Augusto Amador Medeiros

ON THE MODELLING AND CHARACTERIZATION OF ACOUSTIC LINERS UNDER GRAZING FLOW

Dissertação submetida ao Programa de Pós-Graduação em Engenharia Mecânica da Universidade Federal de Santa Catarina para a obtenção do Grau de Mestre em Engenharia Mecânica.
Orientador: Prof. Julio Apolinário Cordioli, Dr. Eng.

Florianópolis
2015

Ficha de identificação da obra elaborada pelo autor, através do Programa de Geração Automática da Biblioteca Universitária da UFSC.

MEDEIROS, AUGUSTO AMADOR
On the modelling and characterization of acoustic liners under grazing flow / AUGUSTO AMADOR MEDEIROS ; orientador, Julio Apolinário Cordioli - Florianópolis, SC, 2015.
126 p.

Dissertação (mestrado) - Universidade Federal de Santa Catarina, Centro Tecnológico. Programa de Pós-Graduação em Engenharia Mecânica.

Inclui referências

1. Engenharia Mecânica. 2. Impedância Acústica. 3. Liners. 4. Ruído Aeronáutico. 5. Aeroacústica. I. Cordioli, Julio Apolinário. II. Universidade Federal de Santa Catarina. Programa de Pós-Graduação em Engenharia Mecânica. III. Título.

Augusto Amador Medeiros

ON THE MODELLING AND CHARACTERIZATION OF ACOUSTIC LINERS UNDER GRAZING FLOW

Esta Dissertação foi julgada adequada para a obtenção do título de "Mestre em Engenharia Mecânica", e aprovada em sua forma final pelo Programa de Pós-Graduação em Engenharia Mecânica.

Florianópolis, 23 de Abril de 2015.

Prof. Armando Albertazzi Gonçalves Jr., Dr.Eng.
Coordenador do Curso

Banca Examinadora:

Prof. Julio Apolinário Cordioli, Dr. Eng. – Orientador
Universidade Federal de Santa Catarina, Brasil

Prof. Andrey Ricardo da Silva, Ph.D.
Universidade Federal de Santa Catarina, Brasil

Prof. Arcanjo Lenzi, Ph.D.
Universidade Federal de Santa Catarina, Brasil

Prof. Hans Bodén, Dr. Tech.
KTH Royal Institute of Technology, Suécia

ACKNOWLEDGEMENTS

There is no better way to start this then with those that have been supporting me and encouraging me my entire life: my parents, Adriana and Gil. Thank you for teaching me the value of education, your greatest legacy.

I would like to thank my supervisor, Prof. Julio Cordioli. Not only for his availability and insightful, patient criticism, but also for his friendship and for the many opportunities he gave me. He strongly advised me to start the Master's degree and for that I am grateful too.

I would also like to thank all my friends at the LVA for the pleasant talks, lunches and ping-pong games. To the Silent Aircraft project team both at the LVA and EMBRAER, thanks for the many technical discussions that have certainly shaped and improved my work. Special thanks to Zargos for proof-reading the first manuscript and patiently giving his input.

This work was supported by funding from EMBRAER S.A. and CAPES, for which I'm thankful.

Finally, I would like to thank someone who has been with me for the better part of the last decade, making my days so much happier. Thank you Camila for comprehending my absences and supporting me through all my decisions.

The Scientific Method: Do whatever it takes not to fool yourself into thinking that something is true that is not, or that something is not true that is.

(Neil deGrasse Tyson)

RESUMO

A determinação da impedância acústica de liners utilizados em motores turbofan de aeronaves comerciais é um ponto de interesse da comunidade científica há várias décadas, especialmente na presença de escoamentos tangenciais, condição similar à de operação. Diferentes técnicas foram desenvolvidas para obtenção da impedância de liners. Atualmente, as mais comuns são as técnicas inversas, que consistem em duas etapas: (i) medição do campo acústico em um duto com escoamento e uma amostra de material, e (ii) simulação do campo acústico e aplicação de um processo de otimização para encontrar a impedância que minimiza a diferença entre resultados experimentais e analíticos. Neste trabalho, foram discutidos três métodos: dois métodos inversos, o Método da Matriz de Transferência e o Método do Acoplamento Modal, e um método direto, o Método Prony. Os três métodos foram implementados e validados através de resultados de simulação numérica em Método de Elementos Finitos. Foram avaliados também o custo computacional e a sensibilidade dos métodos à presença de modos de alta ordem no campo acústico medido. Além disso, amostras de materiais típicos foram caracterizadas em uma bancada de testes em velocidades até Mach 0.25 para comparar os resultados dos diferentes métodos. Modelos preditivos semi-empíricos, que utilizam parâmetros geométricos do material para determinar sua impedância, foram também abordados neste trabalho. Alguns destes modelos foram implementados, e seus resultados para amostras disponíveis comparados aos medidos com os métodos citados. Por fim, uma nova técnica de determinação de impedância foi proposta, incorporando um modelo matemático de impedância ao processo de otimização, de forma a reduzir significativamente o número de incógnitas do sistema, estabilizando assim a solução.

Palavras-chave: Impedância acústica; Liners; Ruído Aeronáutico; Aeroacústica.

UM ESTUDO DA MODELAGEM E CARACTERIZAÇÃO DE LINERS ACÚSTICOS SOB ESCOAMENTO TANGENCIAL

Introdução

O ruído emitido pelas aeronaves nas condições de aterrisagem e decolagem, quando elas se encontram mais próxima ao solo, é bastante incômodo para as comunidades vizinhas. Nestas fases, o ruído é dominado por componentes tonais emitidos nas frequências de passagem das pás do fan do motor. A atual alternativa para tratamento deste ruído tonal, ao qual o ser humano é mais sensível e é por isso penalizado nos testes de certificação das aeronaves, é o tratamento passivo dos dutos do motor utilizando materiais de tratamento acústico chamados *liners*. Estes materiais são tipicamente formados por um núcleo em forma de colméia, entre uma placa perfurada e uma placa-base rígida, formando ressonadores de Helmholtz.

O desempenho dos liners é normalmente avaliado pela sua impedância acústica, que é dependente da velocidade do escoamento tangencial à amostra. Nestas condições, sua determinação não é trivial, e diversos métodos de determinação de impedância nestas condições são descritos na literatura. Neste trabalho, três métodos de determinação de impedância acústica de liners na presença de escoamento foram avaliados: o Método da Matriz de Transferência (TPM, do inglês *Two-Port Matrix Method*) [1], o Método do Acoplamento Modal (MMM, do inglês *Mode-Matching Method*) [2], e o Método Prony (SFM, do inglês *Straight-Forward Method*) [3].

Outra forma de caracterizar os liners é através de modelos preditivos semi-empíricos. Estes modelos fornecem estimativas rápidas da impedância de um material através de seus parâmetros geométricos. Neste trabalho, três destes modelos foram avaliados: o modelo de Kooi e Sarin [4], o de Elnady e Bodén [5], e o de Motsinger e Kraft [6].

Por fim, uma modificação ao MMM foi proposta, incorporando um modelo preditivo ao processo de cálculo da impedância.

Análise Numérica

Nesta parte do trabalho, os três métodos de medição de impedância foram alimentados com dados de entrada provenientes de simulação numérica em Método de Elementos Finitos (FEM). Os resultados obtidos pelos métodos podem ser vistos nas Figuras 3.2–3.10.

Uma análise do efeito de modos de alta ordem no escoamento foi também realizada.

Análise Experimental

Neste capítulo, 4 amostras de liners foram descritas, e seu comportamento avaliado em uma bancada de testes com escoamento. Os métodos de determinação de impedância validados no capítulo anterior foram então utilizados para calcular a impedância destas amostras. Os resultados foram comparados com os obtidos pelos modelos preditivos, nas Figuras 4.9–4.12.

Cálculo de Impedância Parametrizado

Uma modificação ao MMM foi proposta. Ao invés de se encontrar a impedância a cada frequência através de um novo processo de otimização independente, a impedância é modelada como uma função contínua, parametrizada, da frequência. Os parâmetros desta função são então encontrados para minimizar a diferença entre o campo acústico medido e o simulado em todas as frequências medidas de uma só vez. Este método foi validado com simulação numérica e comparado aos resultados experimentais do MMM para uma amostra de liner.

Conclusões

Na validação numérica dos métodos de determinação de impedância, eles se mostraram capazes de encontrar as impedâncias impostas nos modelos numéricos em todas as condições de escoamento. Os erros em geral foram menores para o TPM, que também apresentou o maior custo computacional dentre os métodos. O SFM mostrou-se extremamente rápido, porém possui problemas de convergência em baixa frequência devido à contaminação das medições com fenômenos de transição nos bordos do liner. Na análise dos modos de alta ordem, notou-se que o primeiro modo transversal no duto só piora os resultados dos métodos caso os microfones não estejam localizados na sua linha nodal.

Na frente experimental, os três métodos mostraram resultados bastante semelhantes. Os modelos preditivos, entretanto, ficaram muito aquém do esperado, em geral subestimando a resistência das amostras, especialmente para baixas velocidades de escoamento.

A variação do MMM proposta mostrou-se eficaz, produzindo curvas suaves na frequência e mostrando boa concordância com os resultados dos demais métodos. Foi validada numericamente, apresentando erros semelhantes às demais técnicas, e não foi desestabilizada pelos modos de alta ordem.

ABSTRACT

The problem of determining the acoustic impedance of liners used in turbofan engines of commercial aircraft has been a point of interest for the scientific community for decades, especially in the presence of grazing flows, similar to operational conditions. Different techniques have been developed to determine liner acoustic impedance under grazing flow. The current trends are inverse methods, which consist of two steps: (i) measurement of the acoustic field in a duct with flow and a liner sample, and (ii) modeling of the acoustic field and application of an optimization procedure to find the impedance that minimize the difference between experimental and analytic results. In this work, three techniques were discussed: two indirect methods, the Two-Port Matrix Method and the Mode-Matching Method; and a direct technique, the Straight-Forward Method. The three methods were implemented and validated by means of Finite Element Method numerical simulation results. The computational cost and the sensibility to the presence of higher-order modes were also assessed for each method. Semi-empirical predictive models, which use the geometrical parameters of the materials to determine their impedance, were also discussed in this work. Some of these models were implemented, and their results for available liner samples were compared to those obtained by measurements with the previously cited methods. Lastly, a new technique for impedance determination was proposed, which incorporated a mathematical impedance model to the optimization process as a means to significantly reduce the number of unknowns, therefore stabilizing the solution.

Keywords: Acoustic Impedance; Acoustic Liners; Aircraft Noise; Aeroacoustics

LIST OF FIGURES

LIST OF TABLES

LIST OF ACRONYMS

P-MMM	Parametric Mode-Matching Method
BPF	Blade Passage Frequency
E&B	Elnady and Bodén impedance model
FEM	Finite Element Method
K&S	Kooi and Sarin impedance model
LVA	Vibration and Acoustics Laboratory
M&K	Motsinger and Kraft impedance model
MMM	Mode-Matching Method
PGM	Pressure Gradient Method
POA	Percentage of Open Area
SDOF	Single Degree of Freedom
SFM	Straight-Forward Method
SI	International System of Units (from the French: *Système International d'Unités*)
SPL	Sound Pressure Level
TMM	Two-Microphone Method
TPM	Two-Port Matrix Method
UFSC	Federal University of Santa Catarina

LIST OF SYMBOLS

Latin Symbols

a	Modal amplitude
b	Duct width
c_0	Speed of sound
d	Face-sheet holes diameter
f	Frequency
f_{int}	Correction factor for the interaction between neighboring orifices (E&B)
h	Duct height
i, r	Subscripts for incident or reflected waves
k_0	Wavenumber, ω/c_0
k_x	Mode-number in the x direction
k_y	Mode-number in the y direction
k_z	Mode-number in the z direction (axial)
l	Liner section length
m	Mass reactance component on the EHR model
n	Duct section index (1, 2 or 3)
p	Acoustic Pressure
q	Mode index, ordered by cut-off frequency
t	Perforated plate thickness
u_z	Acoustic Velocity in the z direction (axial)
z	Normalized Impedance
$[T]$	Matrix representing the lined section (TPM)
$[T_{tr}]$	Infinitesimal transition matrix (TPM)
B	"Law of the wall" constant, $B = 5.1$
C_d	Discharge Coefficient
D/Dt	Material derivative
J_n	n-th order Bessel function
K	Viscous Stokes wavenumber
L	Cell Depth, or Honeycomb layer thickness
M	Mean flow Mach number
N	Number of divisions of a period (EHR)
Q	Number of modes considered in the solution
R_e	Reflection coefficient
Re	Reynolds Number

T	Wave period (EHR)
U	Mean flow velocity
U_*	Skin Friction Velocity
W	Acoustic Power
Z_0	Characteristic impedance of the fluid
Z_w	Wall impedance

Greek Symbols

Δt	Time-step (EHR)
α	Absorption Coefficient
β	EHR parameter to account for the varying cavity reactance
χ	Normalized Reactance
δ	End correction
δ_0	No-flow end correction
ϵ_χ	Orifice end-correction for the reactance (E&B)
ϵ_θ	Orifice end-correction for the resistance (E&B)
κ	von Karman constant, $\kappa = 0.4$
ν	Kinematic viscosity of the fluid
ω	Angular frequency
ρ_0	Density
σ	Porosity, same as POA
θ	Normalized Resistance
ξ	Damping in the cavity's fluid (EHR)
Δ_z	Distance between microphones (SFM)
Φ	Mode-shape

Other Symbols

$\dagger$	Morre-Penrose pseudo-inverse
∇^2	Laplace Operator

CONTENTS

1 INTRODUCTION

1.1 Background

The interaction between airports and the surrounding communities is a complex urban phenomenon. New airports are usually built at a distance from the main urban center they serve because of the limitation on the heights of neighboring buildings and, more importantly, the noise emitted by aircraft. Nevertheless, the economic influence of the airport stirs the development of its surroundings, attracting the very urbanization it was built away from.

At that point, the growth of air traffic in the airport is found to be limited mainly by the public acceptance of its noise emissions [7]. To control the emitted noise and thus preserve the health of the closer communities, regulations have been introduced in several airports and nations dictating the noise allowance for aircraft flying to or from them. This has led to the concept of noise certification, in which the aircraft manufacturer has to demonstrate that his product meets certain noise standards in order to enter commercial service. Current demands include noise limits at the three critical operating conditions around the airport (see Figure 1.1): sideline (when the engines are at full power), take-off, and approach. These are critical phases because the aircraft is closer to the affected communities.

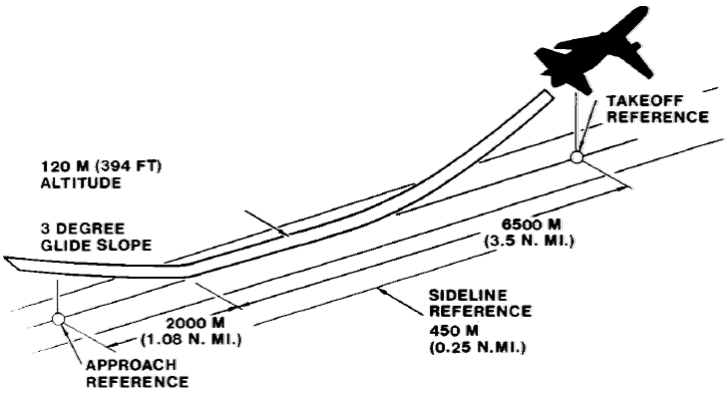

Figure 1.1 – Reference positions for aircraft noise certification [8].

There are several noise sources on an aircraft. Those include the airframe noise, generated by turbulence of air around all devices in the outer flow (fuselage, wings, flaps, landing gear, etc), the propulsion system, among others. During cruise speed, turbulence noise is the most relevant. But for the phases considered in the certification tests, where the aircraft speed is lower, the propulsion system is the dominating source [8]. High-bypass ratio turbofan engines became the norm for civil aviation, mostly because of fuel savings and significant reduction of jet noise. The continued reduction of jet noise, however, brought attention to other engine noise sources, like the main fan and the engine core.

The effective perceived noise level (EPNL) is a parameter employed in certification tests of aircraft. It penalizes discrete tones on the aircraft noise spectra as they are much more annoying to the human perception then a equivalent, broadband noise of the same global level [8]. Since fan noise is characterized by dominating discrete tones associated with blade passage frequencies (BPF), as depicted in Figure 1.2, acoustic treatment of the fan ducts is largely employed to avoid EPNL penalties. This is accomplished by covering the interior nacelle walls with lining materials.

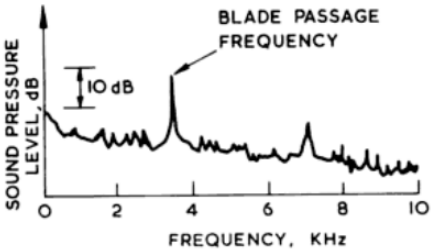

Figure 1.2 – Typical forward arc spectrum of noise from a fan with subsonic tip speeds. Adapted from [9].

Most current liners consist of a honeycomb core positioned between a perforated face-sheet and a rigid back plate, as illustrated in Figure 1.3. This design, which offers the best ratio of weight and noise reduction [10], can be seen as an array of Helmholtz resonators, thus providing good sound attenuation over a narrow frequency band. Their geometric parameters are chosen in order to obtain maximum attenuation on the frequency band of interest, which generally comprises the critical BPF on a specific flight condition.

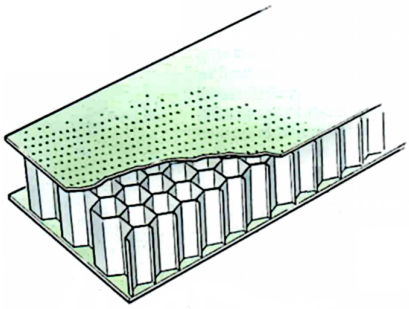

Figure 1.3 – Typical aero-engine liner construction.

In engine noise prediction schemes, liner performance is generally accounted for by means of its acoustic impedance. However, typical aero-engine liner impedance is known to be dependent on the speed of the grazing flow over its surface [11]. Because it is not trivial to measure liner impedance on the presence of grazing flows, several methods were published in the last decades.

A current trend are inverse methods, usually called "impedance eduction methods", which consist of two steps. First, the acoustic field in a duct with a liner sample subject to grazing flow is measured. Then, the acoustic field is simulated using a numerical or analytical method, and an optimization procedure is applied to find the impedance that minimizes the difference between experimental and simulated results.

The main difference between the many published methods is how the acoustic field is simulated in the presence of the liner sample and grazing flow. There are methods based on Finite Element Method simulations [12], two-port systems [1, 13], mode-matching [2], solutions to the convected Helmholtz equation [14], to the linearized Euler equations [15], to the Pridmore-Brown equation [14], among many others. Jing et al. [3] also proposed a new method that does not require an optimization in order to find the impedance, but instead calculates it directly from the test data. To simplify their derivation and application, most of these methods assume that only plane-waves propagate in the hard-wall sections of the test ducts, i.e, the highest frequency under analysis is lower then the cut-on frequency of the first transverse mode of the duct.

In this work, three of the cited methods will be evaluated. These are the Mode-Matching Method (MMM) [2], the Two-Port Matrix Method (TPM) [1], and the Straight-Forward Method (SFM) [3].

The TPM, first proposed by Roeck and Desmet [16], uses an analytic transfer matrix to describe a lined section of a duct with flow. This matrix is a function of the wavenumbers in the lined section, which are found in an optimization procedure and then used to calculate the liner impedance. It showed promising but unstable results, and was later extended by Santana et al. [1] to better handle the effects of the hard-soft wall transitions, solving most of the instabilities seen in Roeck and Desmet preliminary results.

In the MMM, Elnady et al. [2] used the mode-matching technique to couple the acoustic fields in hard-wall and lined sections of a duct, from which the amplitudes of the propagating modes are found for a given impedance guess. The acoustic field is then calculated and compared to the measured one until the error is minimized by finding a matching impedance.

In the SFM, proposed by Jing et al. [3], the acoustic field along the section with the liner sample is measured at equally-spaced positions. The well-known Prony's method is used to approximate the acoustic field as a series of complex exponentials, whose exponents give the axial wavenumbers, and thus the liner impedance. This method differs from the TPM and the MMM because it is not iterative; the wavenumbers, and then the impedance, are calculated directly from the acoustic pressure measurements. This approach has the advantages of not requiring an optimization, thus avoiding its potential drawbacks, such as dependence on initial guesses and difficult convergence in certain situations. This direct approach also has its drawbacks, as will be seen in this work.

A few decades ago, due to technical and technological limitations such as the lack of precise acoustic propagation models, the imprecision of available measurement techniques and instruments, and the weak computational power, little was published about liner impedance measurement methods in the presence of flow [17]. Instead, great attention was given to the construction of predictive models, which normally involved the liner geometric parameters, together with the grazing flow velocity and the excitation frequency. These models were improved over the last decades, showing satisfactory predictions over their validity ranges. In fact, they are still widely used in the industry due to their convenience. They can provide estimates, although with some imprecision, of the impedance of a material while still in design stages. Generally, predictive models are semi-analytic, i.e., with a few terms derived from physical reasoning and modeling, but also including empirical terms, like those found by curve-fitting experimental data.

Out of many published predictive models, the Kooi and Sarin [4] model, from the early 1980s, is still frequently cited. The authors obtained expressions for the resistive and reactive parts of the impedance of liners in the presence of grazing flow, but used the skin friction velocity to characterize the flow speed. The model also takes into account frequency, hole diameter, face-sheet thickness and porosity, cell depth, and fluid properties. Some of these terms were derived empirically, by curve-fitting test data of 5 different liner samples.

Motsinger and Kraft [6] derived a predictive model whose resistance was based on the DC flow resistance of a perforate. Because of that, their resulting expression for the resistance was not frequency-dependent. Nonetheless, this facilitated the modeling of the non-linear response of the perforate to the incident acoustic velocity, by considering the analogous relation between the flow velocity and the acoustic velocity at the holes.

Elnady and Bodén [5] conducted a thorough literature review of existing predictive models, comparing them to test data of 50 different material samples. They identified the many physical phenomena and the most relevant parameters involved in liner impedance, analyzing each effect separately. This resulted in a new model, with the individual terms that best agreed with their experimental data, including some terms from the previous models and some new terms proposed by the authors.

The impedance eduction techniques evaluated in this work result in systems of equations to be solved at each frequency in which the impedance is to be found. Measurement error or bad convergence of the optimization at some frequencies might result in a non-smooth impedance curve, which is not a physical result. In this work, a modification to one of the methods was proposed to incorporate a parametric impedance model to the eduction process. Instead of finding the complex impedance at each frequency, the proposed method finds the parameters of an impedance model, that defines it for all frequencies under analysis. This always results in smooth impedance results if the employed function is smooth, and facilitates interpolation and extrapolation to obtain the impedance at other frequencies.

1.2 Aim and Objectives

The aim of this study is to implement and validate different methods for calculating the acoustic impedance of liners under grazing

flow, through modeling or measurements, and propose an alternative method based on semi-empirical models.

To achieve that, the following objectives were established:

- To review the literature for different predictive models of the impedance of acoustic liners used in aircraft engines.
- To implement at least three grazing flow impedance measurement methods.
- To build Finite Element Method models to validate the implemented methods, in the presence of grazing flows.
- To compare the implemented methods regarding their computational cost, accuracy and required input data.
- To measure the impedance of liner samples in a grazing flow test rig using the validated methods and compare them to the results of the predictive models.
- To propose a new impedance measurement method that includes one of the predictive models in the calculation process, in order to reduce the number of unknowns and stabilize the solution.

1.3 Document structure

The work is organized as follows. In Chapter 2, further details are given on aero-engine acoustic liners. In the same chapter, the predictive models and measurement methods evaluated in the current work are described. In Chapter 3, a numerical analysis of the measurement methods is conducted, including a validation and an analysis of the effect of higher order modes on the obtained results. In Chapter 4, the test rig used in the current work is described, and the impedance of four liner samples is measured with the validated methods and compared to the predictive models. In Chapter 5, a modification to one of the methods is proposed, and the resulting technique is validated and compared to the previous methods using the test data of Chapter 4. Finally, conclusions and suggestions for future work are drawn in Chapter 6.

This work has been done in cooperation with Brazilian aircraft manufacturer EMBRAER S.A., who funded part of it under the Silent Aircraft research project.

2 LITERATURE REVIEW

2.1 Locally Reacting Acoustic Liners

Liners are sound absorbing materials placed on duct walls to attenuate noise that propagates within the duct. They are generally classified as locally or non-locally reacting.

Local reaction means that the direction of the acoustic perturbation inside the material is independent from the direction of the incident plane-wave. Physically, this results from the hypothesis that waves that enter the material are only able to propagate in a direction normal to its surface, never parallel to it. This is generally caused by a solid-backed, regular partitioned structure with solid walls perpendicular to a porous face.

This is the case for typical aero-engine liners, in which the core layer is a metallic honeycomb structure, such as the one depicted in Figure 1.3, covered by a perforated face-sheet and a solid back-plate. The honeycomb walls offer a much higher attenuation in the direction parallel to the liner's surface than normal to it, therefore satisfying the conditions for local reaction.

Typical liners can be seen as an array of Helmholtz Resonators. The air in each hole of the perforated face-sheet can be seen as a mass oscillating with friction on the walls, and the compressibility of the air inside each cavity can be seen as a spring. This amounts to a Single Degree of Freedom (SDOF) system like in a mass-springer-damper oscillator, providing good acoustic attenuation on a narrow frequency band. By varying the geometric parameters of the material, such as hole diameter, cavity depth, and face-sheet thickness, it can be tuned to a specific frequency of interest. In its aero-engine application, this frequency would generally be one of the Blade-Passage Frequencies (BPF) during the aircraft's take-off or approach maneuvers.

As will be seen later, the perforated face-sheet is shown to exhibit non-linear behavior when excited by strong enough acoustic fields. This results in acoustic properties that may vary with the acoustic velocity in its holes [5, 6]. A newer trend in liner design are the so-called linear liners, in which the perforated plate is replaced by, or covered with, a wire-mesh sheet [10]. This type of material does not exhibit non-linear properties when excited by high Sound Pressure Levels (SPL). The focus of this dissertation is nevertheless in typical perforated plate liners, which represent the majority of liners in service in commercial

aircraft.

Non-locally reacting materials, sometimes called bulk reactors, on the other hand, are those in which the incident acoustic waves are able to propagate in any direction. This results in a surface whose acoustic properties may vary with the direction of an incident wave. Typical acoustic treatment materials used in architecture, such as acoustic foams and wools, are of non-locally reacting nature, but may also be approximated as locally reacting for a small enough thickness [18].

Materials that are non-locally reacting exhibit good attenuation over a much wider frequency range then locally-reacting materials. Their main drawback for the aero-engine duct application are the difficulties in withstanding the harsh environment inside the engine. These arrangements retain fluid, which might pose a fire hazard when applied in the core ducts. Water retention might also be a problem in the other parts of the engine. Therefore, locally-reacting, perforated/wire-mesh face-sheet liners are still the norm. There is, however, active research towards the use of bulk liners, which may soon become much more widely used considering their wider frequency range of operation.

The advantage of modeling liners as locally reacting materials is that, as seen from the outside, they can be characterized by a surface impedance (see section 2.2) independent of the angle of incidence. This approximation has been used extensively in analytical and numerical acoustic propagation models, as it greatly simplifies the analysis.

As it was mentioned in Chapter 1, aircraft and engine manufacturers when predicting engine noise use liner impedance as input, mostly in numerical propagation models. Typical liner impedance, however, is dependent on the velocity of a grazing flow through its surface, similar to operational conditions. Therefore, there is a need for accurate liner impedance determination on the presence of grazing flow, which is the reason for this work.

2.2 Acoustic Impedance and Absorption Coefficient

The need for accurate determination of liner impedance was discussed in section 2.1. However, the concept of acoustic impedance has not yet been defined. The acoustic impedance of a material is defined as the ratio between the incident acoustic pressure, p, and the resulting normal particle velocity, u, or:

$$Z(\omega) = \frac{p(\omega)}{u(\omega)}. \tag{2.1}$$

It is commonly found dimensionless, normalized by the characteristic impedance of the medium, given by the product of its density, ρ_0, and speed of sound, c_0, according to:

$$z(\omega) = \frac{Z(\omega)}{\rho_0 c_0} = \theta(\omega) + j\chi(\omega), \tag{2.2}$$

where θ and χ are, respectively, the real and imaginary parts of the impedance, also named resistive and reactive parts, or resistance and reactance. The resistive part is related to the energy dissipation in the surface, while the reactive part, as the name suggests, comes from its inertial and elastic properties.

The impedance of a material is intrinsically related to its capacity to attenuate noise. In fact, in a no-flow, plane-wave, normal incidence environment, there is a simple relation between a material's acoustic impedance and absorption coefficient, α, defined as

$$\alpha = \frac{W_a}{W_i} = \frac{W_i - W_r}{W_i}, \tag{2.3}$$

where W is the acoustic power, and the indexes a, i, and r mean, respectively, absorbed, incident and reflected. Since the acoustic power can be calculated as product of the acoustic intensity, I, by the area of incidence, Equation 2.3 can be simplified to

$$\alpha = \frac{I_i - I_r}{I_i}. \tag{2.4}$$

Again assuming plane-wave incidence, Equation 2.4 can be further simplified as a relation between each plane-wave's amplitudes, p, as

$$\alpha = \frac{|p_i|^2 - |p_r|^2}{|p_i|^2} = 1 - \frac{|p_r|^2}{|p_i|^2}, \tag{2.5}$$

where $|p|$ represents the magnitude of complex number p.

Now, consider an incident harmonic plane-wave on a acoustic material with a surface impedance Z at a position $x = 0$. The pressure and acoustic velocity distributions can be written as:

$$\begin{aligned} p &= \left(p_i e^{-jkx} + p_r e^{jkx}\right) e^{j\omega t}, \text{ and} \\ u &= \frac{1}{\rho_0 c_0} \left(p_i e^{-jkx} - p_r e^{jkx}\right) e^{j\omega t}. \end{aligned} \tag{2.6}$$

At $x = 0$, the impedance boundary condition is given by Equation 2.1:

$$Z = \frac{p(x=0)}{u(x=0)}. \tag{2.7}$$

Substituting the expressions for the pressure and velocity, Equation 2.6, into Equation 2.7, one gets:

$$\frac{Z}{\rho_0 c_0} = z = \frac{p_i + p_r}{p_i - p_r}. \tag{2.8}$$

Solving for the ratio p_r/p_i:

$$\frac{p_r}{p_i} = \frac{z-1}{z+1}. \tag{2.9}$$

Substituting Equation 2.9 into Equation 2.5, the relation between the absorption coefficient and the impedance is found:

$$\alpha = 1 - \left|\frac{z-1}{z+1}\right|^2. \tag{2.10}$$

By analyzing Equation 2.3, it can be seen that, ideally, α may never be higher then the unity, as that would mean that more power is absorbed then it is incident on the material; and never negative, since no energy is generated inside the material. Equation 2.10 respects these conditions, since its second term is always a positive real number smaller then the unity—it is easy to check α tends to zero as $|z|$, or θ (for a fixed χ), tends to infinity.

It is frequently mentioned in the literature that maximum sound attenuation for a given material is seen when its reactance reaches zero. That can be easily checked with the help of Equation 2.10. Additionally, it could be used to check how the absorption coefficient varies with the resistance. In Figure 2.1, the absorption coefficient is plotted for different resistance and reactance pairs.

The results show that, indeed, maximum attenuation is seen for a smaller reactance. For instance, the maximum theoretical unity value for the absorption coefficient is only seen for a null reactance ($Z = 1 + 0j$). Moreover, a higher resistance does not mean a higher attenuation. On the contrary, the resistance of maximum attenuation varies with the reactance.

A possible physical interpretation of these results is that, since the impedance is the ratio of the acoustic pressure to the velocity,

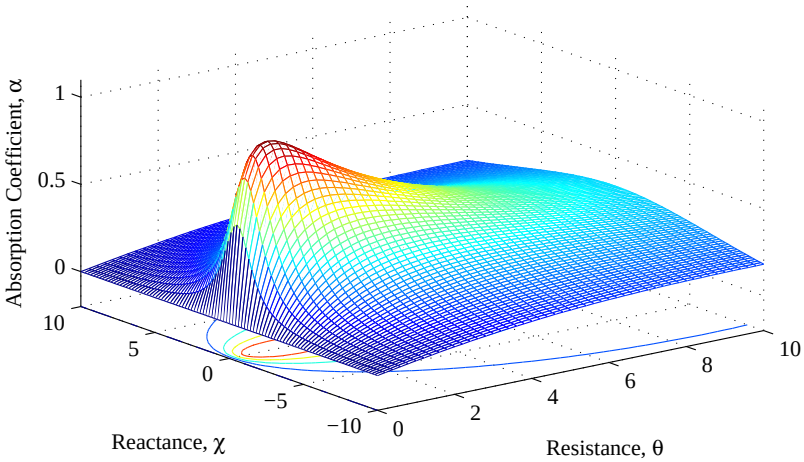

Figure 2.1 – Absorption coefficient, α, as a function of the resistance, θ, and the reactance, χ.

the imaginary part includes the phase information between the two oscillating quantities. In that sense, when the imaginary part is null, pressure and velocity are exactly in phase, which means the acoustic intensity, and therefore the absorbed power, is at a maximum on the material.

The impedance-absorption analogy drawn in this section might be useful, as it is not always obvious what the physical meaning of a given impedance value is. Under more general conditions, the relation between the absorption coefficient and the impedance also changes [19]. However, the impedance is still a more general concept, as it keeps the phase information that is lost when calculating the absorption coefficient.

2.3 Predictive Models for Liner Impedance

As mentioned before in this dissertation, a few decades ago, there were technological and theoretical limitations that hindered development and implementation of impedance measurement techniques. That stimulated research on analytical and semi-empirical predictive models for liner impedance based on the material's geometric parameters. Relevant parameters include perforated plate thickness, t; hole diameter,

d; cell depth, L; and porosity, σ, or percentage of open area (POA), defined as the ratio of the total plate area by the open area.

The advantage of the predictive models consists of giving quick impedance estimates without the need for possibly costly and complex measurements. This can be valuable in early design stages, when a liner sample is not yet available. Moreover, liner geometry might be optimized for a given frequency and flow condition, using these predictive models, based on attenuation requirements.

In this section, four different impedance models will be described. In section 4.4, these models will be used to calculate the impedance of available liner samples, which were also measured in a test rig using the techniques described later in this dissertation.

2.3.1 Kooi & Sarin

The Kooi & Sarin (K&S) model [4], presented in the early 80s, is still frequently cited, and some of the more recent models are actually variations of this model. By measuring the impedance of five liner samples with different geometric parameters (porosity, hole diameter and perforated plate thickness) using the In-Situ technique (see section 2.4.5), the authors showed that the impedance was directly dependent on the skin friction velocity on the liner surface, and not directly on the mean flow Mach number, as usually considered. The skin friction velocity, U_*, defined as the ratio of the shear stress to the fluid density at the wall, can be calculated, for a fully developed turbulent flow, from the "law of the wall" velocity distribution equation [4, 20]:

$$\frac{U}{U_*} = \frac{1}{\kappa}\ln\left(\frac{xU_*}{\nu}\right) + B - \Delta B(\mathrm{Re}_r), \tag{2.11}$$

where U is the flow velocity in a position x inside the boundary layer, ν is the kinematic viscosity of the fluid at the wall, k and B are constants equal to 0.4 and 5.1, respectively, and $\Delta B(\mathrm{Re}_r)$ is a term that accounts for the roughness of the surface as a function of the roughness Reynolds number[1]. Equation 2.11 is transcendental on U^*, and can be solved numerically from the velocity U at a given position x.

From Crandall's theory for the sound propagation through perforated plates [21], it can be shown that the impedance caused by viscous effects, for typical dimensions and frequencies and ignoring the forma-

[1] This term vanishes for a hydraulically smooth wall. Kooi and Sarin measured it for typical liner samples, and found it to be negligible.

tion of the *vena contracta* (see section 2.3.3) inside the holes and the grazing flow, can be written as

$$z_v = \frac{\sqrt{8\nu\omega}}{\sigma c_0}\frac{t}{d} + j\left(\frac{\omega t}{\sigma c_0} - \frac{\sqrt{8\nu\omega}}{\sigma c_0}\frac{t}{d}\right), \tag{2.12}$$

where t is the face-sheet thickness, d is the hole diameter, ω is the angular frequency, in radians per second, ν is kinematic viscosity of the fluid, and c_0 is the speed of sound in the fluid.

Equation 2.12 is used to calculate the no-flow impedance, and is then subtracted from the measured impedance under grazing flow, assuming the difference is simply its variation due to flow. By doing that to all liner samples in different flow speeds, they find the following empirical expression for the real part of the impedance:

$$\theta = \frac{\sqrt{8\nu\omega}}{\sigma c_0}\frac{t}{d} + \frac{5 - \frac{t}{d}}{4\sigma c_0}(9.9U_* - 3.2fd), \tag{2.13}$$

where f is the frequency, in Hertz, and all other variables assume SI units.

For the reactance, the imaginary part of Equation 2.12 is added to the reactance of a cavity of height L, and a new end-correction term, δ, is added to the hole's length (which is the plate thickness, t), resulting in the expression:

$$\chi = \frac{\omega(t+\delta)}{\sigma c_0} - \frac{\sqrt{8\nu\omega}}{\sigma c_0}\left(1 + \frac{t}{d}\right) - \operatorname{cotg}\left(\frac{\omega L}{c_0}\right). \tag{2.14}$$

The end-correction term is related to the effect of an added mass at each side of the orifice, that oscillates with the mass of air inside the orifice. It is assumed that this mass distribution around and inside each orifice is concentrated in a cylinder of air whose length is slightly longer then the plate thickness. The authors considered the Guess [22] model to account for this effect in the absence of grazing flow, given by

$$\delta_0 = 0.85d(1 - 0.7\sqrt{\sigma}), \tag{2.15}$$

where the term enclosed in parenthesis is an additional correction for the interaction between adjacent orifices. This interaction comes from the fact that the mass of air around the orifices also oscillates, therefore overlapping for close enough orifices.

The mean flow also plays a role in the attached mass, since part of it is carried downstream, resulting in a reduction of the end-correction

term. The authors used curve-fitting in their test results to obtain an empirical expression for the end-correction in the presence of flow, given here normalized by the no-flow end-correction from Equation 2.15, written as:

$$\frac{\delta}{\delta_0} = 0.92 - 0.75\frac{U_*}{ft} + 0.11\left(\frac{U_*}{ft}\right)^2. \tag{2.16}$$

2.3.2 Motsinger & Kraft

Motsinger and Kraft (M&K) took a different approach in modeling the impedance of acoustic liners. By measuring the DC flow resistance[2] of perforates, they noted its linear dependence with the incident flow velocity, as illustrated in Figure 2.2, and drew an analogy with the acoustic velocity.

The total resistance at a given incident velocity has two parts. The first, a constant term, is caused by linear effects such as pressure loss due to friction inside the holes. The second, a velocity-dependent term, is caused by turbulence in the entrances and exits of the holes. It is modeled using a viscous model that accounts for the formation of the *vena contracta*, a region where the diameter of the stream is reduced and the streamlines become parallel, thus accelerating the flow. Because of this last contribution, the M&K model has a term for the non-linear dependence of the impedance with the incident acoustic velocity, as will be seen later.

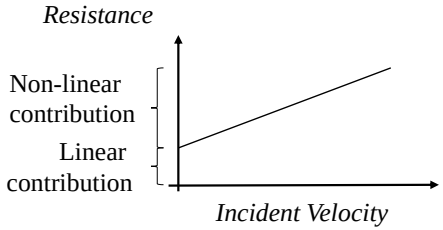

Figure 2.2 – DC Flow resistance contributions due to linear term and non-linear term.

[2]This is an hydraulic analogy where the perforate is seen as an electric resistance in a direct-current circuit (hence the DC name), very common in the Fluid Mechanics literature. The resistance is calculated from the potential difference across the object, represented by the pressure drop, and the current passing through it, represented by the flow velocity incident on the sample.

The *vena contracta* is taken into account by means of the the discharge coefficient, C_d, which gives the relation between the incident velocity on the perforate and the actual velocity inside the hole. The authors claim that 0.76 is a typical value for the C_d of liner perforates. The resulting expression for the resistance is[3]:

$$\theta = \frac{64\nu t}{2\rho_0 c_0 \sigma C_d d^2} + \frac{|u_i|}{2c_0\sigma^2 C_d^2}, \tag{2.17}$$

where $|u_i|$ is the absolute value of the incident acoustic velocity. Since it is not generally known beforehand, it has to be calculated iteratively from the measured incident acoustic pressure and last iteration's calculated impedance value, until convergence is reached.

The reactance term is very similar to the K&S, Equation 2.14, however the viscous term on Crandall's theory was not used. The resulting equation is:

$$\chi = \frac{\omega(t+\delta)}{\sigma c_0} - \operatorname{cotg}\left(\frac{\omega L}{c_0}\right), \tag{2.18}$$

where the end-correction, δ, is modeled as suggested by Rice *et al.* [23]:

$$\frac{\delta}{\delta_0} = \frac{1}{1 + 305M^3}, \tag{2.19}$$

and δ_0 is still given by Equation 2.15.

2.3.3 Elnady & Bodén

The work of Elnady and Bodén [5] (E&B) was mostly a revision of several works on the modelling of liner impedance. For each of the parameters considered relevant for the impedance, different previously published models were compared, and new equations were also proposed. That includes the works of Kooi and Sarin, Rice *et al.*, Guess, and Motsinger and Kraft, cited in the previous sections, among others.

An important difference from most previous works is in how the Crandall's theory is considered. Differently from the low frequency and usual dimensions assumptions made by Kooi and Sarin, that resulted in Equation 2.12, Elnady and Bodén kept the complete expression, given

[3]The author uses the Centimetre-gram-second (CGS) system of units, which should be respected because of the constant in Equation 2.17.

by:

$$z_v = \frac{\left(\frac{j\omega t}{\sigma c C_d}\right)}{F(Kd)}, \tag{2.20}$$

where

$$F(Kd) = 1 - \frac{4J_1(Kd/2)}{KdJ_0(Kd/2)}, \tag{2.21}$$

and J_0 e J_1 are the zeroth and first order Bessel functions, respectively, and K is the viscous Stokes wavenumber inside the hole, defined as

$$K = \sqrt{-\frac{j\omega}{\nu}}. \tag{2.22}$$

Elnady and Bodén [5] state that, historically, the form of Equation 2.20 was not normally used to calculate the impedance of perforated plates because of difficulties in calculating the Bessel functions with complex arguments, and in separating the real and imaginary parts of the result. Today, however, this is no longer a problem. By assuming $|Kd| > 10$, which is normally the case for typical frequency and dimensions, the $J_1/J_0 \rightarrow (-j)$ approximation can be made, and Equation 2.20 reduces to Equation 2.12, normally found in the literature.

Another important term is the end-correction, as seen in the previous models. The authors discussed several models, including the Guess and Rice models. In this model, however, the contributions from the effective hole length, ϵ, and from the interaction between adjacent holes, f, were clearly separated, so that the final correction is their product, $\delta = \epsilon f$. Another distinction is that two end-corrections are used: one for the resistance, ϵ_θ, and one for the reactance, ϵ_χ.

Elnady and Bodén measured the end-correction for 50 distinct samples, and wrote expressions for each term that best fitted their results. For the real part, the end-correction is given by

$$\epsilon_\theta = 0.2d + 200d^2 + 16000d^3, \tag{2.23}$$

and for the imaginary part, by

$$\epsilon_\chi = 0.5d. \tag{2.24}$$

For the interaction between orifices, a few models were tested: Guess' model, given by the term enclosed in parenthesis in Equa-

tion 2.15, Muller's model [24], and Fok's model [5]. They ended up using Muller's model, on the basis that it gave results very similar to Fok's, despite being derived from very different experiments. In Muller's model, this factor is given by

$$f_{int} = 1 - 1.47\sqrt{\sigma} + 0.47\sqrt{\sigma^3}. \tag{2.25}$$

Going forward, Elnady and Bodén discuss the grazing flow effect on the resistive and reactive parts of the impedance.

On the resistive part, after comparing different models, including the K&S, whose dependency with flow velocity was indirect, the authors ended up developing their own model, given by the simple relation $0.5M/\sigma$. It agreed with their test data as well as the K&S model, and is easier to use since it is based on the Mach number, instead of the skin friction velocity used on the K&S, which is more difficult to measure.

On the reactance, the K&S (Equation 2.16) and Rice's (Equation 2.19) models were compared, among others. The flow effect on the reactance is generally accounted for on the end-correction term, δ_0, by means of a multiplying factor smaller then the unity, to represent the reduction in the attached mass as it is carried downstream by the flow. In Elnady and Bodén experiments, both the K&S and Rice's model underestimated the influence of the grazing flow, which appeared to be responsible for a significant reduction on the reactance. Instead of using a new end-correction factor for the flow, they added a new term to the reactance, which, similarly to what was done on the resistive part, is given simply by $-0.3M/\sigma$, and demonstrated to be capable of predicting reactance variations with flow speed.

Similarly to the M&K, a term dependent on the incident acoustic velocity is added to both the resistance and the reactance to account for the non-linear behavior of the perforated face-sheet. The incident velocity, as in the M&K, needs to be calculated iteratively from an incident pressure spectrum and the impedance.

The E&B model also discussed the effect of bias flow[4] on the perforates; this however is not of interest to the present study, thus not

[4]Bias flow is the flow through the perforates, as opposed to the grazing flow, parallel to the surface, considered in this work. It is more common in automobile applications, such as car mufflers.

being discussed here. The final equation for the resistive part is:

$$\theta = \mathrm{Re}\left\{\frac{j\omega}{\sigma c_0 C_d}\left[\frac{t}{F(Kd)} + \frac{\epsilon_\theta}{F(Kd)} f_{int}\right]\right\} + \frac{1}{\sigma}\left[1 - \frac{2J_1(kd)}{kd}\right] + \frac{0.5}{\sigma} M + \left(1 - \sigma^2\right) \frac{|u_i|}{2c_0\sigma^2 C_d^2}, \tag{2.26}$$

where the last term is the non-linear effect, and $k = \omega/c_0$ is the wavenumber. The reactive part is:

$$\chi = \mathrm{Re}\left\{\frac{j\omega}{\sigma c_0 C_d}\left[\frac{t}{F(Kd)} + \frac{\epsilon_\chi}{F(Kd)} f_{int}\right]\right\} - \cot\left(\frac{\omega L}{c_0}\right) - \frac{0.3}{\sigma} M - \left(1 - \sigma^2\right) \frac{|u_i|}{6c_0\sigma^2 C_d^2}. \tag{2.27}$$

It is worth mentioning that the authors measured the discharge coefficient, C_d, for their 50 perforate samples, and found that it varied with t and d. This contradicts the claim by Motsinger and Kraft [6], who suggested that 0.76 would be a typical value. Elnady and Bodén [5] published their C_d results in the form a table as a function of t and d, from which the C_d used in this work were be interpolated.

2.3.4 Extended Helmholtz Resonator

The Extended Helmholtz Resonator [25] (EHR) differs from the previously models because it was not developed as a predictive model. Its parameters, unlike the previous models, are not easily linked to geometrical properties of the materials, which is why it is not being considered a "predictive model". It is covered in this dissertation nevertheless because it offers a simple set of equations for generating impedance curves in the frequency domain that strongly resemble typical liner impedance curves and satisfy a design impedance at a given frequency.

Rienstra [25] developed the EHR for translating impedance values in the frequency domain into an equivalent relation in the time-domain, mostly for use in numerical methods. This problem is not trivial because of the necessity to guarantee that the resulting relation is physical, i.e., obeys the causality, reality and passivity conditions. Violation of these conditions would manifest as non-physical results, like generation of energy at the wall or other non-physical instabilities.

The EHR, as the name suggests, is based on a simple Helmholtz

resonator, whose impedance satisfies the above conditions. More details on this matter and the derivation can be seen on the original paper [25]. The resulting frequency-dependent impedance expression is:

$$Z(\omega) = R + j\omega m - j\beta \cot\left(\frac{1}{2}\omega\nu\Delta t - j\frac{1}{2}\xi\right), \tag{2.28}$$

where ωm is the mass reactance of the air in the perforations, β is a parameter to account for different cavity reactances, Δt is the time-step, and ξ is the damping in the cavity's fluid. In the original paper, advice is given on how to choose the parameters to generate curves that resemble liner impedance, i.e., without abrupt variations in the frequency range of interest and within coherent impedance values.

Additionally, Rienstra derives the equations that give the above parameters to generate an impedance curve satisfying a design impedance at a given frequency $\omega = \omega_0$, $Z_d = Z(\omega_0) = \theta_0 + j\chi_0$. Suppose a wave period $T = 2\pi/\omega_0$ is divided in N parts (typically, $N = 20$), i.e., $T = N\Delta t$. In that case, Δt is defined:

$$\Delta t = \frac{2\pi}{N\omega_0}. \tag{2.29}$$

If m is set to zero for convenience, and the cavity's fluid damping ξ is chosen between the limits

$$0 \leq \xi \leq \operatorname{arsinh}\left(-\frac{\theta_0}{\chi_0}\sin\left(\omega_0\nu\Delta t\right)\right), \tag{2.30}$$

to make sure that the resistance $\theta \geq 0$, then β and R are determined from the design impedance with the following relations:

$$\beta = -\chi_0 \frac{\cosh(\xi) - \cos\left(\omega_0\nu\Delta t\right)}{\sin\left(\omega_0\nu\Delta t\right)}, \tag{2.31}$$

$$R = \theta_0 + \chi_0 \frac{\sinh(\xi)}{\sin\left(\omega_0\nu\Delta t\right)}. \tag{2.32}$$

The only parameter not yet defined is ν, which can be chosen empirically. After conducting a parameter study, Rienstra advises that ξ be chosen as large as possible (for instance, around 90% of the upper limit in Equation 2.30) and ν be set to 1 for $X_0 < 0$ or between $N/2$ and N otherwise.

This model and the above relations were used to create the impedance curves seen on the numerical validation carried-out in this

dissertation, in section 3.1.

For illustrative purposes, we choose $Z_d = 1 - 1j$ at $\omega = (1500)2\pi$ rad/s, i.e., we want the parameters that generate an impedance whose resistance passes through 1, and reactance through -1, at 1500 Hz. By employing equations 2.29 to 2.32, we find parameters seen in Table 2.1. The resulting impedance calculated using Equation 2.28 is shown in Figure 2.3. It can be seen that, as expected, the impedance equals $1 - 1j$ at 1500 Hz.

Table 2.1 – EHR parameters resulting from design impedance $Z_d = 1 - 1j$ at $\omega_0 = (1500)2\pi$ rad/s.

R	m	β	ν	Δt	ξ
0.592	0.000	1.079	5.000	$3.333.10^{-5}$	0.397

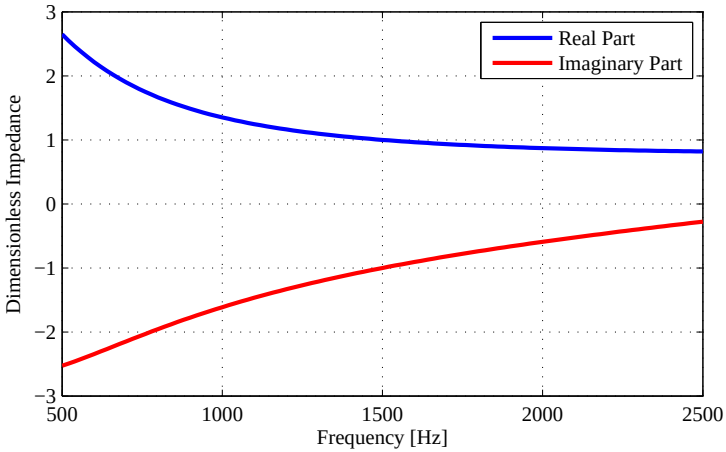

Figure 2.3 – Impedance curve obtained with the EHR from design impedance $Z_d = 1 - 1j$ at $\omega_0 = (1500)2\pi$ rad/s.

2.4 Impedance Measurement Methods

In the introduction of this work, a few methods for measuring the acoustic impedance of liners under grazing flow were cited. In this section, three of them will be described in more detail: the Two-Port Method (TPM), the Mode-Matching Method (MMM) and the

Straight-Forward Method (SFM). Additionally, in section 2.4.5 some other methods, not implemented in this dissertation but historically or technically relevant, will be briefly described.

Since all the cited methods build on the same foundations, i.e., the physics of acoustic propagation in a flow duct with a liner sample, this section will first introduce the basic set of equations shared by them. They are based on a duct geometry as seen in Figure 2.4, whose walls are rigid except for a section of length l where an impedance Z_w is applied to the wall at $x = b$. The duct can be seen as having three different sections: a hard-wall, inlet section (1), then a lined section, which represents the region with the liner in the experimental configuration (2), followed by a hard-wall, outlet section (3). Uniform flow in the positive z-direction is assumed in all sections.

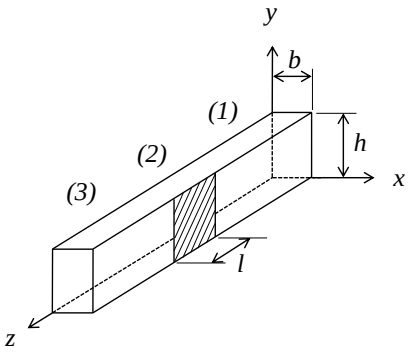

Figure 2.4 – Rectangular duct with height h and width b, whose wall at $x = b$ has an impedance Z_w along a section of length l.

2.4.1 Sound Propagation in a Duct with Uniform Mean Flow

In a duct with uniform mean flow in the axial (z) direction, the convected wave equation [26] for linear acoustics is given by

$$\nabla^2 p - \frac{1}{c_0^2} \frac{D^2 p}{Dt^2} = 0, \tag{2.33}$$

where D/Dt is the material derivative and ∇^2 is the Laplace operator. Each solution to the wave equation represents a mode, that propagates

only above its cut-on frequency f_c, given by

$$f_c = \frac{c_0}{2h}(1 - M^2)^{1/2}, \tag{2.34}$$

where M is Mach number of the uniform mean flow in the duct, and h could be replaced by b for the modes in the other direction. The acoustic field in each of the three sections n, p_n, is calculated by the summation of the Q modes in the duct section, whose mode shapes are given by $\Phi(x, y)$, so that

$$p_n = \sum_{q=1}^{Q} a_{ni}^{(q)} \Phi_{ni}^{(q)} e^{-jk_{zni}^{(q)} z} + \sum_{q=1}^{Q} a_{nr}^{(q)} \Phi_{nr}^{(q)} e^{jk_{znr}^{(q)} z} \tag{2.35}$$

where the indexes i and r represent the incident and reflected waves which propagate respectively in the $z+$ and $z-$ directions, q is the index of the mode, ordered by its cut-off frequency[5], a is the amplitude of each mode, and $k_{zn}^{(q)}$ is the wavenumber in the z direction for the q-th mode, that satisfies the dispersion relation [26]

$$k_x^2 + k_y^2 + k_z^2 = (k_0 \pm M k_z)^2, \tag{2.36}$$

where k_0 is the wavenumber ω/c_0. The wavenumbers in the cross-sectional directions, k_x and k_y, are implicit in the mode shapes $\Phi(x, y)$. The $e^{j\omega t}$ harmonic time dependence is omitted for brevity in Equation 2.35 and all equations derived from it.

An hypothesis made by the methods described in the following sections is that only plane waves propagate in the section with hard walls, i.e., the maximum frequency under analysis should be below the lowest cut-on frequency in the duct, given by equation 2.34. That means that if only plane waves are incident in section 1, higher-order modes generated at the interface with section 2 will decay exponentially with axial distance. The same happens with modes generated at the interface of section 3 to section 2.

Using the hard-wall boundary condition at all walls in section 1 and 3, the wave numbers and the mode shapes can be calculated. The

[5] Another useful way of indexing modes is by using the mode order in each direction, as in (m, n). In that case, m represents the mode order in the x direction and n, in the y direction. For instance, mode (2,1) would be the compound mode of the second transverse mode in the x direction ($m = 2$) with the first transverse mode in the y direction ($n = 1$).

wavenumbers in the x and y directions for the q-th mode are

$$\begin{aligned} k_{xi}^{(q)} = k_{xr}^{(q)} = \pi(q-1)/b, \text{ and} \\ k_{yi}^{(q)} = k_{yr}^{(q)} = \pi(q-1)/h, \end{aligned} \tag{2.37}$$

with the mode shapes having a cosine form for symmetric modes and a sine form for anti-symmetric modes, in each direction [27]. In the lined section, the boundary conditions are symmetric in the y direction, and, similarly to what occurs in the hard-wall sections, the wave numbers can be found from Equation 2.37. Below the first cut-on frequency in the y direction, $k_{y2i}^{(1)} = k_{y2r}^{(1)} = 0$, and from the dispersion relation, Equation 2.36, the wave numbers in the x direction are

$$\begin{aligned} k_{x2i}^{(q)} = \sqrt{(k_0 - Mk_{z2i}^{(q)})^2 - (k_{z2i}^{(q)})^2}, \text{ and} \\ k_{x2r}^{(q)} = \sqrt{(k_0 + Mk_{z2r}^{(q)})^2 - (k_{z2r}^{(q)})^2}. \end{aligned} \tag{2.38}$$

By taking the expression for the acoustic field in the duct, equation 2.35, and applying the Myers boundary condition [28] for the impedance at $x = b$, the following equation is derived:

$$Z_w = jZ_0 \frac{k_0}{k_{x2i}^{(q)}} \left(1 - M\frac{k_{z2i}^{(q)}}{k_0}\right)^2 \cot(k_{x2i}^{(q)} b), \tag{2.39}$$

where Z_0 is the characteristic impedance of the fluid, given by the product of its density and speed of sound. The same equation could be written in terms of the reflected wave numbers (index r) by changing the sign of the Mach number M inside the parenthesis [1].

Equation 2.39 is important because it relates the impedance on the wall to the wavenumbers in the duct, allowing one to calculate the wall impedance once the wavenumbers of the acoustic field are known. Conversely, it also allows one to calculate the wavenumbers in the duct for a given impedance value.

2.4.2 Two-Port Matrix Method

In the Two-Port Matrix Method, it is assumed that there is a dominant mode propagating throughout the whole duct, although its exact mode shape might change depending on the region in which it is propagating. In this case, Equation 2.35 could be rephrased for the

lined section, section 2, as

$$p_2 = a_{2i}\Phi_{2i}e^{-jk_{z2i}z} + a_{2r}\Phi_{2r}e^{jk_{z2r}z}. \tag{2.40}$$

Applying the Linearized Momentum Equation [26] to Equation 2.40, the acoustic velocity distribution can be derived:

$$u_{z2} = \left(\frac{1}{Z_i}\Phi_{2i}e^{-jk_{z2i}z} - \frac{1}{Z_r}\Phi_{2r}e^{-jk_{z2r}z}\right), \tag{2.41}$$

where Z_i e Z_r are defined as

$$Z_i = Z_0\left(\frac{k_0 - Mk_{z2i}}{k_{z2i}}\right), \text{ and } Z_r = Z_0\left(\frac{k_0 + Mk_{z2r}}{k_{z2r}}\right). \tag{2.42}$$

Using equations 2.40 and 2.41, expressions for the relations between pressure and velocity before (index $2in$) and after (index $2out$) the test section can be written, resulting in a transfer matrix, $[T]$, in a similar fashion to what is done in ref. [26], of the form:

$$\begin{Bmatrix} p_{2out} \\ u_{2out} \end{Bmatrix} = \begin{bmatrix} \frac{Z_i e^{-jk_{z2i}l} + Z^- e^{jk_{z2r}l}}{Z_i + Z_r} & \frac{Z_i Z_r\left(e^{-jk_{z2i}l} - e^{ik_{z2r}l}\right)}{Z_i + Z_r} \\ \frac{e^{-jk_{z2i}l} - e^{jk_{z2r}l}}{Z_i + Z_r} & \frac{Z^- e^{-jk_{z2i}l} + Z_i e^{jk_{z2r}l}}{Z_i + Z_r} \end{bmatrix} \begin{Bmatrix} p_{2in} \\ u_{2in} \end{Bmatrix}. \tag{2.43}$$

Equation 2.43 can be considered the main equation of the TPM. It presents a system of two equations and two unknowns (k_{z2i} and k_{z2r}) that when solved provides the wavenumbers in the axial direction inside the lined section. Applying these wavenumbers to Equation 2.38, the wavenumbers in the x direction can be calculated, and then used to calculate the unknown impedance, Z_w, using Equation 2.39.

The TPM implies that pressure and velocity before and after the lined section are known beforehand, which can be achieved using the multiple-microphone wave decomposition technique presented in Appendix A. This assumes that pressure and velocity at the beggining of section 2 equal pressure and velocity at the exit of section 1, and the same is assumed at the interface of sections 2 and 3, i.e., there is no discontinuity of pressure or velocity through the interfaces. This assumption will be discussed in the following section.

2.4.2.1 Hard-Soft Wall Transition

As outlined above, the TPM assumes that only one mode propagates throughout the duct. This can be approximately true in most of the duct length, if the frequency considered is below the first cut-on frequency. However, although the higher order modes generated by scattering in the hard-soft-wall transitions decay with distance, they are still present in their vicinities, and the transfer matrix approach does not take this into account.

Additionally, there is data suggesting that the physical phenomena in these transitions in the presence of flow are reasonably complex. There is evidence of the possible generation of a hydrodynamic wave similar to a Kelvin-Helmholtz instability [29–31], although that discussion is outside the scope of this study.

Santana et al. [1] suggests that the effects of the hard-soft wall transition be incorporated to the present method through the addition of a new transfer matrix, $[T_{tr}]$. This matrix represents an infinitesimal transition duct element before and after the lined section, as shown in Figure 2.5.

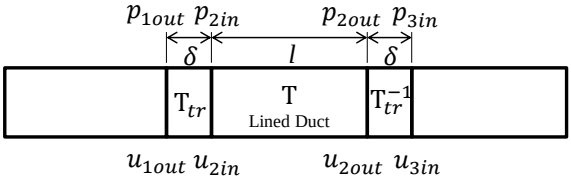

Figure 2.5 – Schematics of the two-port matrix representation of the infinitesimal transition element.

The $[T_{tr}]$ matrix relates the pressures and velocities before and after the transition region. The effects on each side of the lined section are considered symmetric, so that the transfer matrix at the exit is the inverse matrix of $[T_{tr}]$. Pressure and velocity at the beginning of section 3 are then related to those at the end of the first duct section by:

$$\begin{Bmatrix} p_{3in} \\ u_{3in} \end{Bmatrix} = [T_{tr}][T][T_{tr}]^{-1} \begin{Bmatrix} p_{1out} \\ u_{1out} \end{Bmatrix}. \tag{2.44}$$

At first, no assumption is made about the form of the transition matrix, $[T_{tr}]$, adding four new unknowns (the elements of $[T_{tr}]$) to the analysis, in addition to the two wavenumbers in the z direction from

Equation 2.43, resulting in a total of 6 unknowns. Since Equation 2.44 is a system of 2 equations, two additional independent measurements have to be made, which can be achieved by means of the two-source or two-load techniques [32]. They consist in making a new measurement with a different duct outlet impedance (two-load technique) or with a different source position[6] (two-source technique). By doing that, the system represented by Equation 2.44 can be assembled two more times. The final system consists of 6 equations and 6 variables, which can be solved with a non-linear system solver, for instance, via an optimization procedure. In the current work, the MATLAB *fsolve* [33] minimizer with the Levenberg-Marquardt [34] was used, with mostly default tolerances.

2.4.3 Mode-Matching Method

The main difference between the MMM and the TPM, presented previously, is that the MMM takes into account as many modes as necessary in each section. It still assumes that the only mode propagating towards both sides of the lined section is a plane wave mode, such that the acoustic fields in sections 1 to 3 can be written as:

$$p_1 = a_{1i}^{(1)}\Phi_{1i}^{(1)}e^{-jk_{z1i}^{(1)}z} + \sum_{q=1}^{Q} a_{1r}^{(q)}\Phi_{1r}^{(q)}e^{jk_{z1r}^{(q)}z}, \tag{2.45}$$

$$p_2 = \sum_{q=1}^{Q} a_{2i}^{(q)}\Phi_{2i}^{(q)}e^{-jk_{z2i}^{(q)}z} + \sum_{q=1}^{Q} a_{2r}^{(q)}\Phi_{2r}^{(q)}e^{jk_{z2r}^{(q)}(z-l)}, \tag{2.46}$$

$$p_3 = \sum_{q=1}^{Q} a_{3i}^{(q)}\Phi_{3i}^{(q)}e^{-jk_{z3i}^{(q)}(z-l)} + a_{3r}^{(1)}\Phi_{3r}^{(1)}e^{jk_{z3r}^{(1)}(z-l)}. \tag{2.47}$$

In Equation 2.45 the summation only occurs for the reflected modes, since the only incident mode is the plane-wave mode ($q = 1$). Analogously, in Equation 2.47 the summation only occurs for the incident modes, since the only reflected mode (which propagates in $z-$, i.e., towards section 2) is the plane-wave mode.

Mode-Matching is the name of the technique used to determine how acoustic energy is transferred from one duct section to the other

[6] For instance, if in the first measurement the source was upstream of the liner sample, in the second it would be downstream.

through the propagating modes at the discontinuities. First, it is assumed continuity of pressure and axial velocity at the interface of section 1 with the lined section ($z = 0$), and then at the interface of the lined section with section 3 ($z = l$), so that:

$$p_1(x, y, 0) = p_2(x, y, 0), \tag{2.48}$$

$$p_2(x, y, l) = p_3(x, y, l), \tag{2.49}$$

$$u_{z1}(x, y, 0) = u_{z2}(x, y, 0), \tag{2.50}$$

and

$$u_{z2}(x, y, l) = u_{z3}(x, y, l). \tag{2.51}$$

The authors then apply the boundary conditions (equations 2.48 to 2.51), and using the orthogonality between modes it is possible to end up with a system of $4Q$ equations and $4Q$ unknowns, the model amplitudes $a_{1r}^{(q)}$, $a_{2i}^{(q)}$, $a_{2r}^{(q)}$ and $a_{3i}^{(q)}$, for q from the first mode to the Q-th mode.

The required inputs to the system of equations are the incident plane-wave amplitude in section 1, $a_{1i}^{(1)}$, and the exit reflection coefficient $R_e^{(q)} = a_{3r}^{(q)}/a_{3i}^{(q)}$, which is zero for all $q > 1$ since the only reflected mode is the plane-wave mode, as per Equation 2.47. Both inputs can be easily computed using the procedure outlined in Appendix A. It is also required to know the wave numbers for each mode, in each direction, in each duct section. In the hard sections, they are easily computed from equations 2.37 and A.2. In the lined section, they have to be computed from an expected impedance value by solving together equations 2.38 and 2.39.

From solving the aforementioned system of equations for an expected impedance value, the modal amplitudes are found, and the acoustic field can be computed at any position in the duct with equations 2.45 to 2.47. It makes sense then to use the microphones positions already used to compute $a_{1i}^{(1)}$ and $R_e^{(q)}$ to compare the calculated acoustic field to the measured one. From that, a cost function is built, and by minimizing it the unknown impedance can be found. In the current work, the MATLAB *fsolve* [33] minimizer with the Levenberg-Marquardt [34] algorithm was used, with mostly default options, similar to the TPM.

A detailed derivation of the full system of equations can be seen in the original papers [2, 27].

2.4.4 Straight-Forward Method

As seen in the previous sections, the TPM and the MMM rely on pressure measurements on the hard-wall sections of the duct. The MMM uses them to calculate incident pressure and reflection coefficient, and the TPM, to calculate pressure and velocity at the liner's leading and trailing edges. The Straight-Forward Method (SFM) instead uses pressure measurements along the lined section.

If N equally-spaced microphones are positioned in the wall opposite to the liner sample, the pressure at the n-th microphone could be rewritten, from Equation 2.35, as a sum of exponentials:

$$p(z_n) = \sum_{q=1}^{k} A^{(q)} e^{\mu^{(q)} z_j} \tag{2.52}$$

where $\mu^{(q)} = -jk_z^{(q)}$ for downstream (q odd) and $\mu^{(q)} = jk_z^{(q)}$ for upstream (q even) traveling waves, $k = 2Q$, Q still being the number of modes considered in the solution, and $A^{(q)}$ is the product of the wave amplitude by its mode-shape at the measured duct height.

This is where Prony's method [35, 36] is used. If $z_n = n - 1 = 0, 1, 2, ..., N-1$, the exponentials in Equation 2.52 can be written as $e^{\mu^{(q)} n} = \left(e^{\mu^{(q)}}\right)^n = \left(\alpha^{(q)}\right)^n$. Prony observed that each of these exponentials satisfies some fixed, k-th order linear difference equation

$$\begin{aligned} y(n+k) + C_{k-1} y(n+k-1) + \\ C_{k-2} y(n+k-2) + \cdots + C_0 y(n) = 0, \end{aligned} \tag{2.53}$$

whose characteristic equation is

$$\alpha^k + C_{k-1}\alpha^{k-1} + C_{k-2}\alpha^{k-2} + \cdots + C_0 = 0, \tag{2.54}$$

with roots $\alpha^{(q)}$. Since any individual term satisfy the linear, homogeneous equation, linear combinations of them also satisfy it. In particular, the original function, Equation 2.52, satisfies it:

$$\begin{aligned} p(n+k) + C_{k-1} p(n+k-1) + \\ C_{k-2} p(n+k-2) + \cdots + C_0 p(n) = 0, \\ n = 1, 2, ..., N-k. \end{aligned} \tag{2.55}$$

Since $p(z_n)$ is known by measurements in n points, Equation 2.55 can be

used to construct a system of k equations from which the coefficients $C_i (i = 0, 1, ..., k-1)$ are found. Knowing the C_i, we can substitute them into the characteristic equation, Equation 2.54, to find the roots $\alpha^{(q)}$, which in turn give the expoents $\mu^{(q)}$ and thus the wavenumbers $k_z^{(q)}$. Since both the C_i and the $\alpha^{(q)}$ have to be determined, it is necessary to make measurements on at least $2k$ points, i.e., $n \geq 2k$ for a determined (equal case) or overdetermined (greater-then case) system. From here and on, the same procedure outlined in the TPM explanation is followed: calculate k_x and then the impedance from Equation 2.38 and Equation 2.39.

A parameter worth paying attention is the spacing, Δ_z, between consecutive microphones. Since most experimental setups use relatively short liner samples (in the test rig used in the current work, described in section 4.1, it is 200 mm long) and a number of microphones have to be positioned in such a limited length, the range of possible spacings is restricted. But it plays an important role in Prony's method. Since it is basically sampling a continuous signal (pressure along the duct) in discrete positions to later describe it using a series of complex exponential functions, it is not much different then what a Discrete Fourier Transformation (DFT) does, and the distance between the microphones (the rate of sampling in a DFT) will determine the highest frequency which one can distinguish in the signal. Under the Nyquist frequency criterion [37], to avoid aliasing the distance should be chosen in order to have at least 2 points per wavelength of the highest frequency of interest, i.e., the distance Δ_z should be chosen to satisfy:

$$\Delta_z < \frac{c_0}{2 f_{max}}. \tag{2.56}$$

The hard-soft wall transition effects mentioned in section 2.4.2.1 might also be important in Prony's method [3]. Again because of the limited length of the liner samples and because microphones have to be positioned along it, the first and last microphones on the array might be too close to the transitions, which might in turn contaminate the measurements. Good practice when designing the microphone array is to leave at least a few wavelengths of distance from the transitions to the closer microphones to avoid that problem. This will be discussed later in the numerical validation of the SFM in section 3.1.

2.4.5 Other Methods

There are several other impedance measurement techniques in addition to the ones described here. A brief description of some other methods is given below.

For the case without flow, a widely-known method is the standing wave tube method, in which a material sample is located at one end of a tube and the standing wave parameters are measured using a continuous trace of pressure along the tube. These parameters are then related to the specimen properties. This time-consuming method, which became an ISO standard [38], evolved into the Two-Microphone Method (TMM), that uses two fixed microphone positions to separate the incident and reflected waves, from which the impedance is calculated. The TMM has also became an ISO standard [39].

A variation of the TMM, described in Appendix A, allows mean flow and multiple microphone positions to be considered. It was used in this dissertation to compute input data required by the TPM and the MMM.

In terms of the impedance determination methods that consider a grazing flow, the In-Situ technique [40], introduced by Dean in the 70's, is to this day widely used. It is based on the fact that, for a cavity under certain conditions, there is a relationship between the acoustic particle velocity and the acoustic pressure inside the cavity. By further assuming that the acoustic velocities are the same on either side of the face-sheet, acoustic pressures outside the sample and inside the cavity sample are measured, and their frequency response function is used to calculate the material's impedance.

The In-Situ technique has several advantages regarding versatility of liner samples it can measure and laboratory apparatus. It also does not require any knowledge or prediction of the acoustic propagation in the duct, which is mostly based on simplifying assumptions that might introduce uncertainties. Nevertheless, it is destructive, as the liner sample has to be drilled to accommodate the microphones. Additional problems include near-field effects that influence microphone readings flush to the liner surface [5] and also that the impedance is measured only at a single point, thus running the risk of not being representative of the entire sample [17].

The drawbacks of the In-Situ method and the obvious problems with adding mean-flow to the closed tubes used on the TMM motivated the development of indirect techniques, like the TPM and MMM described before.

Researches at the American space agency, NASA, have developed several indirect techniques. One of them, the Pressure Gradient Method (PGM) [12], uses a 2D FEM to model the acoustic propagation along the lined section of a duct for a given impedance value. The impedance guess is varied in an optimization until the calculated pressure gradients in the axial direction at the beginning and ending of the liner sample match the measured ones. This is a very robust method because of the FEM approach. It has since been extended to handle higher order modes cut-on in the hard-wall sections [41]. This configuration, however, requires dozens of microphones in order to decompose the acoustic field, which is rather cumbersome and not available at all laboratories.

3 NUMERICAL ANALYSIS

This chapter describes the computational procedures of the present work, which includes building numerical models of a test rig geometry in order to validate the implemented methods and test some assumptions. These analyses were of utmost importance to the present work, since they highlighted the characteristics of the impedance measurement techniques on a controlled environment, i.e., with simulation-generated input data, which is generally free of noise and reliable, and model characteristics (geometry, flow speed, imposed impedance, etc) known down to machine precision.

There are several computational methods for solving acoustic problems. One of the oldest and still most used methods is the Finite Element Method (FEM) [42], which is capable of solving a multitude of problems and has been the subject of decades of research and optimizations. Out of several commercial acoustic simulation software based on FEM, on this work the FFT ACTRAN [43] package was used.

FFT ACTRAN is a simulation package aimed at the aerospace industry. Because of that, it has most of the tools needed for simulating liner samples in a flow duct: the capability to include uniform and non-uniform mean flow in the simulation, and the Myers boundary condition for the impedance wall in the presence of flow. Additionally, it has several boundary conditions (BC), of which the Modal Duct stands out in the present analysis.

The Modal Duct (or Modal Basis) BC is used to model semi-infinite ducts in which the sound field can propagate in both directions along its axis. This BC is attached to one or both ends (inlet/outlet faces) of a duct model to make it infinite in that direction. It allows defining the amplitude of individual modes coming from infinity (as an excitation), or defining that certain modes generated in the duct are free to propagate to infinity, thus not being reflected at the boundary. If all modes within the frequency range of the simulation are set free to propagate into the BC with no reflections, a truly anechoic termination is created, since the modes form a basis to describe the acoustic field in the duct. This BC was extensively used here in all validation models, being specially useful in the analysis described in section 3.2, where its capabilities will be explored to control the modal content of the excitation.

This chapter will be structured as follows. The first section, 3.1, deals with the numerical validation of the impedance measure-

ment methods carried-out using ACTRAN. The next one, section 3.2, describes a second validation where modifications were made to the numerical models for checking whether the implemented methods are able to handle higher-order modes present in the duct.

3.1 Numerical Validation

The logic of the validation described in this section is very straightforward, as explained below:

1. First, a rectangular duct model is built. Its characteristics, including BC, flow cases, microphone positions, geometry, and mesh properties are detailed in section 3.1.1.

2. In a segment of a given length, one of the duct walls has a known, frequency-dependent impedance applied to it, simulating the liner sample.

3. Several data-recovery points are positioned before, along, and after the test section to mimic microphone positions in a real test rig. The pressure data exported at the microphone positions are read by the impedance calculation algorithms, which try to find the impedance imposed in the model. These results are shown in section 3.1.2 for the different simulated flow conditions, along with the correct (reference) values imposed in the models.

4. For a method to be considered validated, it must be able to find, within satisfactory tolerances, the impedance curves applied in the models, i.e., its results should converge to the imposed impedance.

3.1.1 Model description

With the previously described validation procedure in mind, a FEM model was built. Its geometry is similar to the test rig used at section 4.1, whose main parameters are:

- Rectangular duct cross-section of 0.04 by 0.10 m;

- Test section for liner samples of 0.20 m in length, covering the entire duct height (0.10 m);

- 4 microphones before and 4 after the test section, each group symmetrically positioned in the wall opposite to the liner sample, and an additional 10 microphones on the opposite wall along the liner section with a $\Delta_z = 0.02$ m spacing. The microphone coordinates are given in Table 3.1

Table 3.1 – Microphone positions on FEM model. Microphones 5 to 14 are used in the SFM. The rest are used in both the TPM and the MMM. The origin of the system of coordinates is located on one of the vertexes of the inlet face.

	Microphone	x [m]	y [m]	z [m]
Before Liner	1	0.05	0	0.10
	2	0.05	0	0.27
	3	0.05	0	0.36
	4	0.05	0	0.41
Along liner	5	0.05	0	0.70
	6	0.05	0	0.72
	7	0.05	0	0.74
	8	0.05	0	0.76
	9	0.05	0	0.78
	10	0.05	0	0.80
	11	0.05	0	0.82
	12	0.05	0	0.84
	13	0.05	0	0.86
	14	0.05	0	0.88
After liner	15	0.05	0	1.17
	16	0.05	0	1.22
	17	0.05	0	1.31
	18	0.05	0	1.48

The mesh, seen in Figure 3.1, was built with 20 elements per wavelength of the highest frequency of interest (2500 Hz), taking into account the highest simulated flow speed (102.9 m/s, or Mach 0.3). The mesh is composed of TETRA elements with linear interpolation functions. In ACTRAN, the Modal Duct BC was applied to the inlet face. It was set to impose all modes cut-on on the frequency range of the simulation: the plane-wave mode (0,0) and the first transverse mode on the x-direction (1,0), which cuts-on at 1700 Hz without flow as per Equation 2.34. Additionally, the Modal Duct was used to make the inlet face anechoic by setting all incident modes as free.

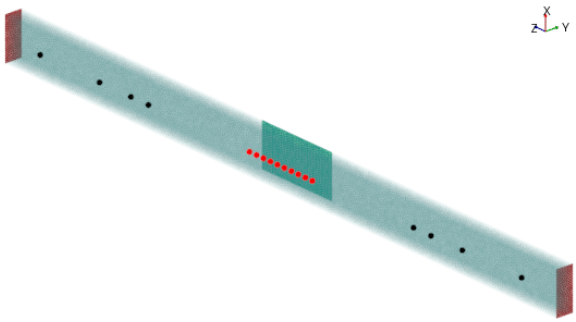

Figure 3.1 – FEM model for the validation. The darker elements on the wall represent the liner region. On both ends, the inlet and outlet faces. The darker points are microphones 1–4 and 15–18, used by the TPM and MMM, and the lighter points are microphones 5–14, used by the SFM.

The impedance curves in the frequency domain were generated using the Extended Helmholtz Resonator Model (see section 2.3.4) with parameters chosen in order to generate typical liner impedance values. These were applied to the liner region using the Myers boundary condition, simulating the presence of the liner sample. Although it is known that the impedance of a real liner sample would change with the grazing flow speed, for consistence in this analysis all models had the same impedance applied independently of the simulated flow speed. Regarding flow, three conditions were tested: no-flow, Mach 0.2 (68.6 m/s) and Mach 0.3 (102.9 m/s). The results obtained by the three implemented methods can be seen in the following section.

3.1.2 Results

In this section, the results of the numerical validation will be presented. It is divided into three parts, according to the simulated flow speed. On each of them, the results obtained by the SFM, TPM and MMM will be shown together with the relative error between imposed (reference) and calculated impedance values. Furthermore, every figure will have a blue vertical line at the cut-on frequency of the first transverse mode.

3.1.2.1 No-Flow Condition

For the results presented in this section, the FEM model seen in Figure 3.1 was solved without mean flow. The pressure results were then used to calculate the impedance using the TPM, MMM, and SFM, whose results can be seen, respectively, on Figure 3.2, Figure 3.3, and Figure 3.4.

On the no-flow validation, all three methods were able to find impedance values within a 5% range around the reference values. The TPM and MMM have very similar error curves, starting from near-zero, increasing as it gets closer to the duct cut-off frequency, and then reducing as frequency increases. This might be due to the first transverse mode becoming more important around its cut-on frequency, but then the plane-wave dominates the acoustic field again for higher frequencies.

The SFM, however, shows a different behavior, with the largest errors being on the lower frequencies, reducing as frequency increases. This characteristic of the SFM error will be discussed in the next results where there is flow, and the low frequency errors become more prominent.

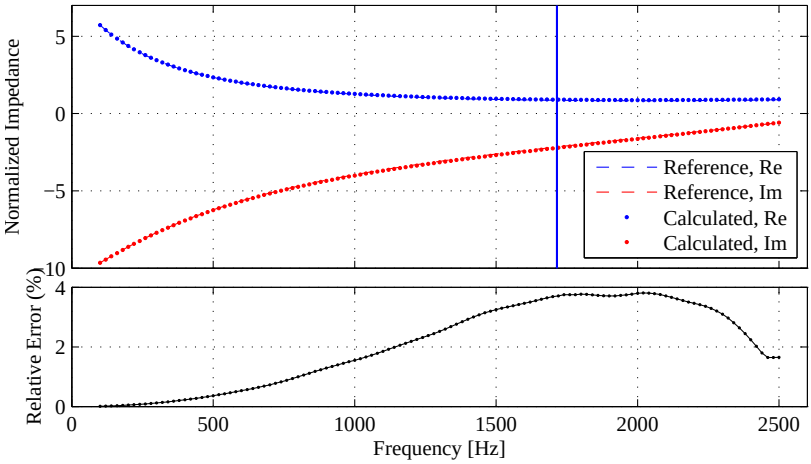

Figure 3.2 – Normalized impedance and relative error obtained with the Two-Port Method for the no-flow condition.

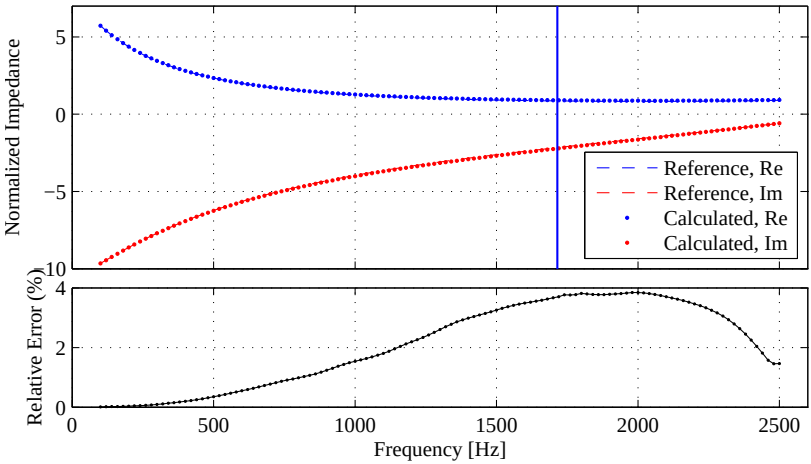

Figure 3.3 – Normalized impedance and relative error obtained with the Mode-Matching Method for the no-flow condition.

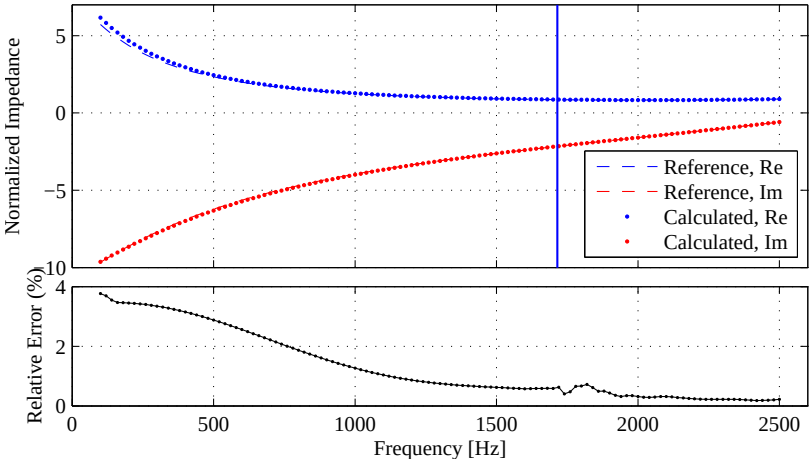

Figure 3.4 – Normalized impedance and relative error obtained with the Straight-Forward Method for the no-flow condition.

3.1.2.2 Mach 0.2 condition

For the following results, a Mach 0.2 (68.6 m/s) mean flow was considered in the FEM simulation. The results for each method can be

seen in Figure 3.5 (TPM), Figure 3.6 (MMM), and Figure 3.7 (SFM).

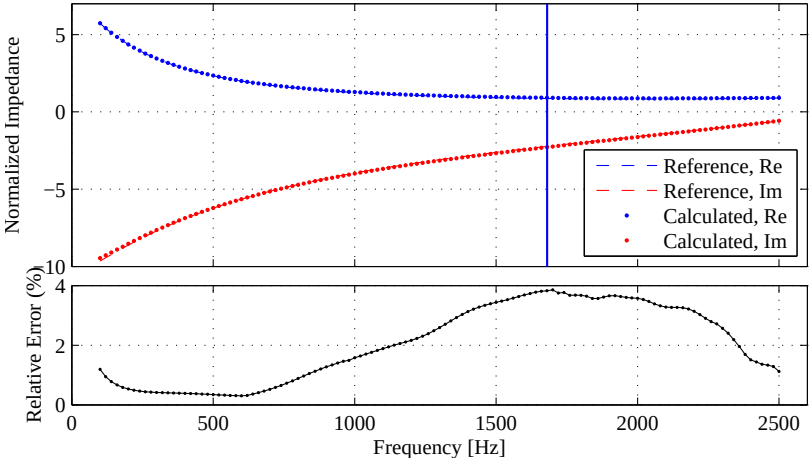

Figure 3.5 – Normalized impedance and relative error obtained with the Two-Port Method for the Mach 0.2 validation result.

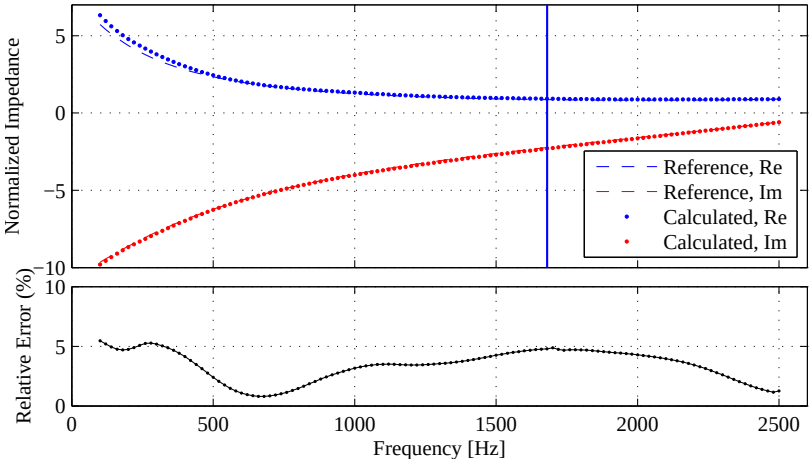

Figure 3.6 – Normalized impedance and relative error obtained with the Mode-Matching Method for the Mach 0.2 validation result.

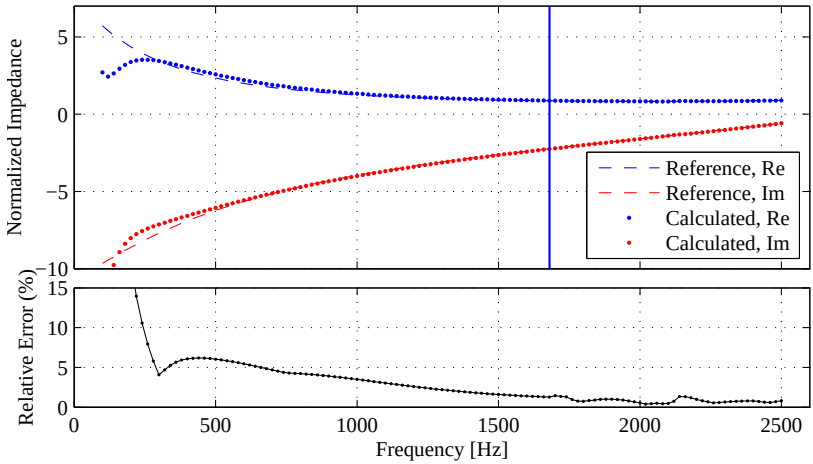

Figure 3.7 – Normalized impedance and relative error obtained with the Straight-Forward Method for the Mach 0.2 validation result.

The TPM and MMM results, seen in Figure 3.5 and Figure 3.6, were similar to the no-flow results. Both methods showed a slight increase in lower-frequency errors, but the remaining frequencies were mostly unaltered by the presence of flow. The SFM error increased significantly below 300 Hz, but was also mostly unaltered at higher frequencies.

This increase in lower-frequency errors, subtle in the TPM and MMM but relevant in the SFM, can be explained by the effects associated with the hard-soft wall transitions cited in section 2.4.2.1, that are captured by the microphones closer to the liner's leading and trailing edges. This is supported by a few evidences:

- It is less pronounced in the no-flow results (see Figures 3.2 to 3.4);
- It affects only the lower-frequency range, where wavelengths are larger and thus relevant for larger distances;
- It is more pronounced on SFM results, whose microphones are much closer to the liner's leading edge and trailing edge then TPM and MMM microphones;

- In the SFM case, it is alleviated by removing from the calculations the microphones closer to the liner's edges.

By placing microphones further away from the transitions, one might minimize this effect and improve the SFM results. That should be kept in mind when designing a test rig for the SFM. A larger number of microphones increases the over-determination for solving Equation 2.52, improving the results. But if they are too close to the transitions their measurements might be contaminated. A compromise solution, whenever possible, would be to increase the liner sample length, so that one might have a sufficient number of microphones, while keeping enough distance from the transitions.

Accordingly, the SFM results seen in this work were all calculated using 8 microphones, instead of the 10 available. This was seen to significantly improve lower-frequency results for the SFM, and did not have any significant impact at other frequencies.

3.1.2.3 Mach 0.3 condition

In this last test case, a Mach 0.3 (102.9 m/s) mean flow was considered in the simulation. Results are seen in Figures 3.8 to 3.10.

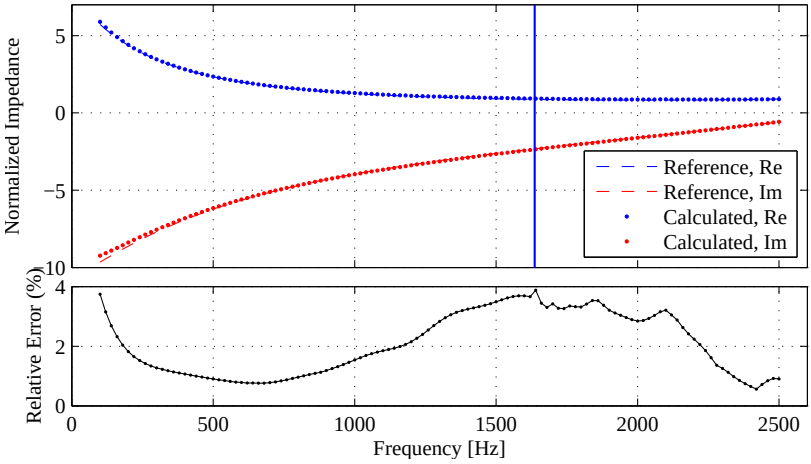

Figure 3.8 – Normalized impedance and relative error obtained with the Two-Port Method for the Mach 0.3 validation result.

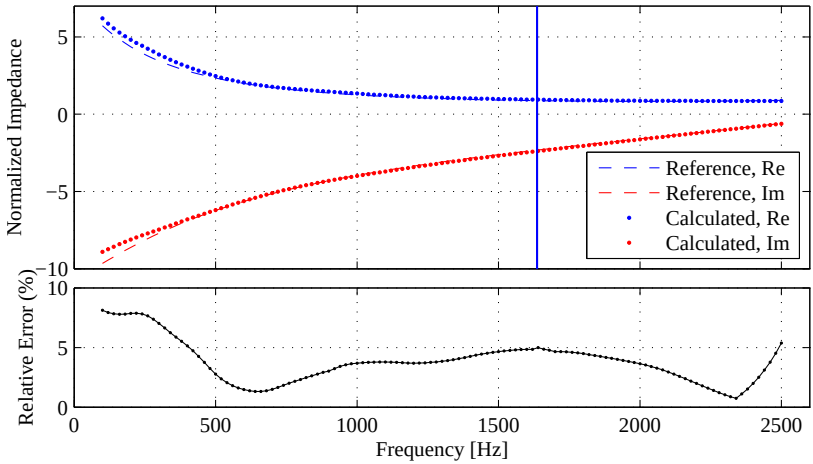

Figure 3.9 – Normalized impedance and relative error obtained with the Mode-Matching Method for the Mach 0.3 validation result.

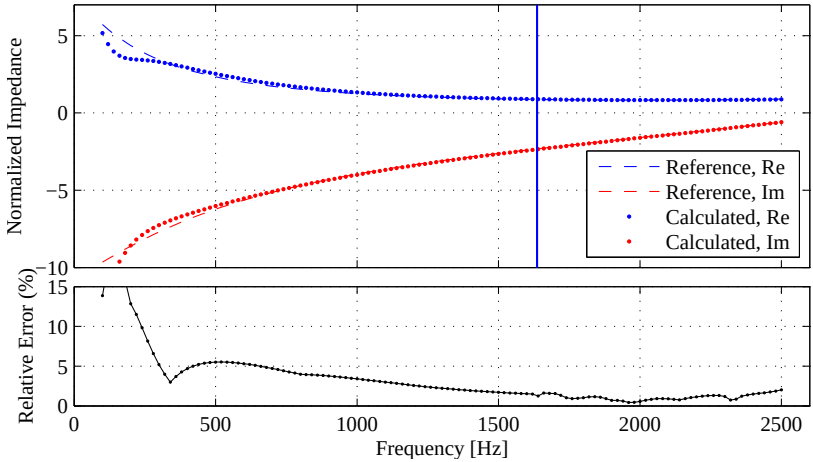

Figure 3.10 – Normalized impedance and relative error obtained with the Straight-Forward Method for the Mach 0.3 validation result.

At Mach 0.3, the results do not differ much from the Mach 0.2 ones. Again, worse convergence is seen for all methods on lower frequencies, the worst case being the SFM. The errors for all methods at those frequencies are also generally higher then on Mach 0.2. This corroborates the hypothesis raised in the last section, that in lower frequencies, where wavelengths are larger, hard-soft wall transition effects are contaminating the measurements.

The methods are now considered validated. They successfully found the imposed impedance at three different flow conditions, on a broad frequency range, within satisfactory tolerances.

Generally speaking, the TPM and the MMM are able to reach smaller errors at the lower frequency range, i.e., below 1000 Hz, in the presence of mean flow, comparing to the SFM. However, their errors increase with frequency, reaching between 4% and 5% at the duct cut-off frequency. The SFM, on the other hand, has problems with lower frequencies, but reaches errors below 1% at higher frequencies.

3.1.3 Computational Cost

It is interesting to compare processing times for each method. Table 3.2 shows the time that each method took to find the results seen in this validation. These times were obtained from averaging ten runs of each method in a quad-core Core i7 desktop machine clocked at 3.2 GHz with 16 GB of DDR3 RAM.

Table 3.2 – Average solve times, in seconds, for each test case.

	TPM	MMM	SFM
No-Flow	210	38	0.3
Mach 0.2	128	102	0.3
Mach 0.3	125	158	0.3

As expected, processing times for the SFM are much lower then for the two other methods. As per the current implementation, the SFM basically involves the inversion of two small matrices (usually less then 50 elements) and a few conditional statements at each frequency, which is very lightweight processing for current standards.

The MMM and the TPM, on the other hand, solve an optimization problem to find the impedance at each frequency, which requires running their objective functions multiple times until one of the convergence criteria is met. That is even after the TPM and the MMM were

implemented in a distributed fashion for solving each frequency in parallel, which results in an approximate 4-times reduction of processing times in the quad-core test machine[1].

3.2 The effect of higher-order modes

In the last section the models were excited with all modes cut-on in the frequency range of the simulations. These included the plane-wave mode and the (1,0) mode, which cuts-on at 1700 Hz and has a nodal line on half of the duct's height. It could be seen that the presence of the (1,0) mode did not significantly affect the results. However, the microphones were positioned exactly on the nodal line of that mode, so theoretically it could not have been measured.

A question remains if the same results would have been seen in case the microphones were in a height other then the nodal line height. Additionally, it remains to be answered whether exciting the model with a plane wave instead of all cut-on modes makes the solution any more stable, be the microphones on the nodal line or on a different height.

This section tries to answer the previous questions by solving the FEM validation model up to 3500 Hz in order to include the first and also the second transverse mode, which cuts-on at 3400 Hz and has nodal lines on thirds of the duct height.

In the first two results, the microphones are kept on the middle of the duct's height. First, in section 3.2.1, only the plane-wave mode will be imposed on the inlet face of the model. Then, in 3.2.2, all modes in the frequency range are excited. This is equivalent to the models solved in the previous validation.

In the next two sections, the position of the microphones is changed in order to remove them from the nodal lines. They are then placed on an arbitrary position, $x = 0.015$ m, chosen not to match, or be too close to, the nodal lines of the first ($x = 0.050$ m) and second transverse modes ($x = 0.033$ m and $x = 0.066$ m). Both excitations will again be tested: in section 3.2.3, plane-waves will excite the inlet, and in section 3.2.4, all modes will be used as excitation. Mach 0.3 uniform mean flow was considered in all models.

[1] The actual speedup does not reach a 4-times improvement because of the overhead created by the communication between each parallel-running process [44].

3.2.1 Plane-wave excitation and original microphone positions

In this section, the microphones are kept on their original positions, i.e., $x = h/2$. The Modal Duct BC is set to impose a plane-wave on the inlet. The results obtained by the three methods can be seen in Figure 3.11.

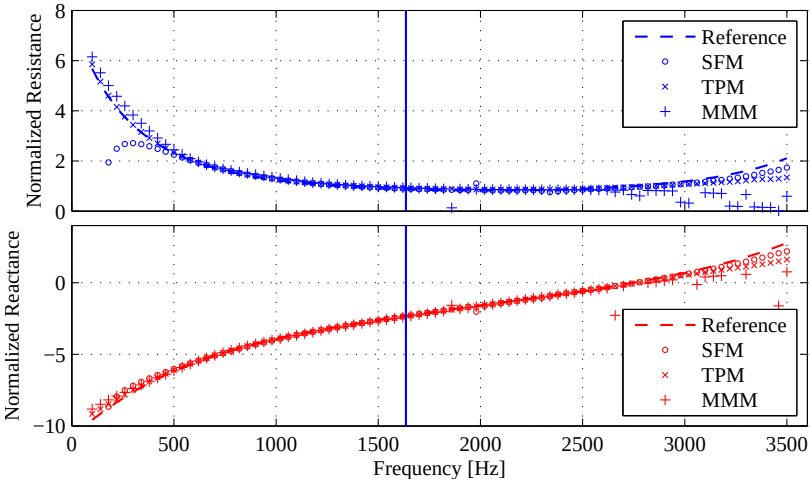

Figure 3.11 – Reference and educed impedance for Mach 0.3, plane-wave excitation, and microphones on $x = h/2$.

It is observed that the three methods were able to find the imposed impedance for most frequencies. At around 3000 Hz all results start diverging from the imposed impedance. On the lower frequency range, the SFM diverges from the imposed impedance. An hypothesis for justifying this has already been presented in section 3.1.2. Additionally, the MMM showed unstable results for the upper frequency range. This however is not believed to be caused by the higher-order modes, but by difficulties in the optimization algorithm.

3.2.2 All modes and original microphone positions

With the microphones still on $x = h/2$, now the Modal Duct BC is set to impose all modes cut-on on the frequency range. The results for all three methods are presented in Figure 3.12. These are

the same presented in Figures 3.8 to 3.10, however here for an extended frequency range.

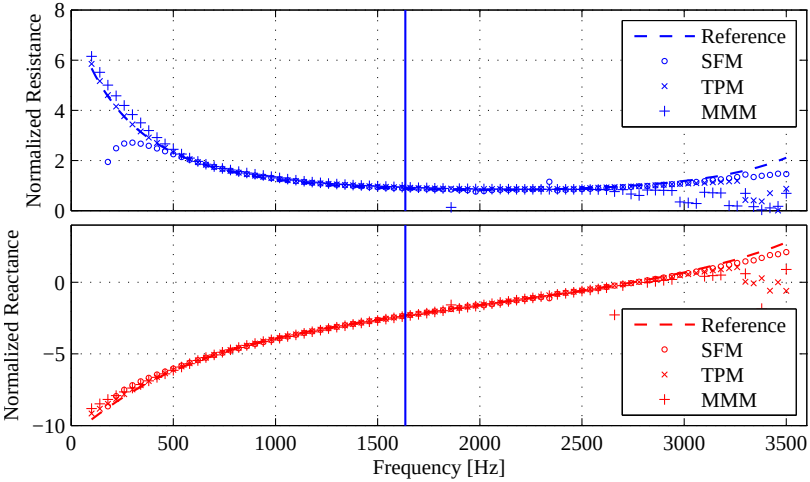

Figure 3.12 – Reference and educed impedance for Mach 0.3, all-modes excitation, and microphones on $x = h/2$.

In Figure 3.12, the same behavior as those in Figure 3.11 is seen, i.e., good results at lower frequencies, but instabilities at higher frequencies for the MMM; good results at higher frequencies and divergence in lower frequencies for the SFM for reasons already mentioned. In this case the TPM also presented some instability at higher frequencies, close to the second transverse mode cut-on frequency. By comparing Figures 3.11 and 3.12 it can be concluded that exciting with plane-waves or all cut-on modes does not make a great difference for any of the methods, at least while the microphones are kept at the nodal line.

3.2.3 Plane-wave excitation and modified microphone positions

For this section and the next one, the microphones are removed from $x = h/2$, where there is a nodal line of the first transverse mode, and positioned at an arbitrary position $x = 0.015$ m. The results for this configuration can be seen in Figure 3.13.

It can be seen that if plane-wave excitation is used, removing the microphones from the nodal line of the transverse mode does not affects the results. In fact, the results found in this case are very similar

to the two previous results.

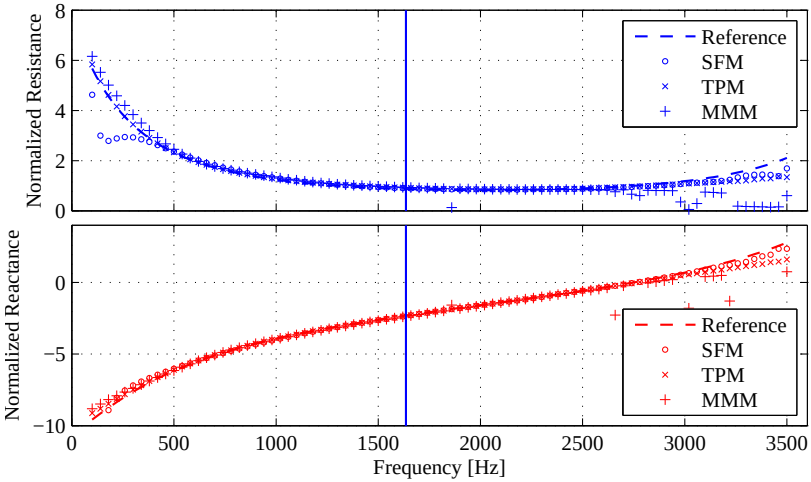

Figure 3.13 – Reference and educed impedance for Mach 0.3, plane-wave excitation, and microphones on $x = 0.015$ m.

3.2.4 All modes and modified microphone positions

In this section, the microphones are again positioned at $x = 0.015$ m on the duct wall. The results are shown in Figure 3.14.

As soon as the first transverse mode cuts-on at around 1700 Hz (actually 1636 Hz because of the convection effect), all methods start to diverge from the imposed impedance, which indicates that the methods' plane-wave hypothesis loose validity. This transition is quite abrupt, with all methods converging to correct results up to exactly the cut-on frequency indicated by the vertical blue line in Figure 3.14. Closer to the second cut-on mode, around 3272 Hz, the situation is even worse, with scattered results and none of the methods converging.

3.2.5 Discussion

In this section, the plane-wave propagation hypothesis of the TPM, MMM and SFM was put to test. It was desired to check whether they were able to find the correct results when higher order modes were

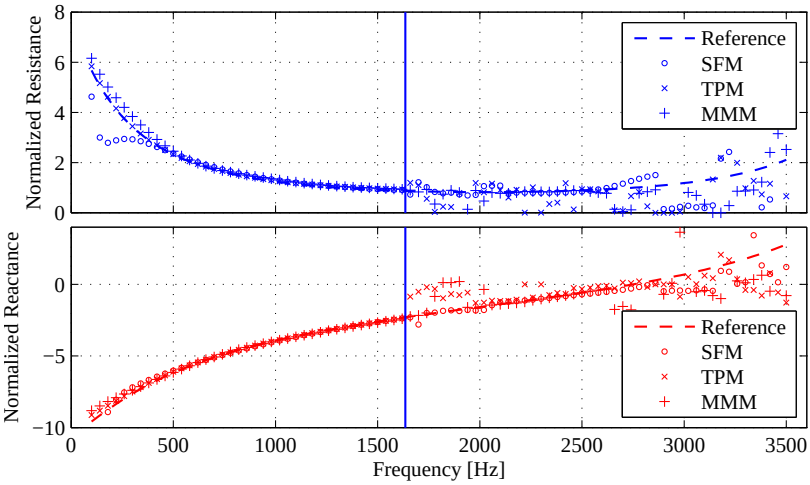

Figure 3.14 – Reference and educed impedance for Mach 0.3, all-modes excitation, and microphones on $x = 0.015$ m.

present in the acoustic field. For that, the analysis frequency range was chosen in order to have two higher-order modes cut-on.

It was found that if one is able to select the microphone positions to be at the nodal line of the undesired cut-on mode, the effect of that mode on the impedance eduction method is reduced. If that is not the case, convergence will depend on whether the excitation is a plane-wave or if the undesired mode is also excited.

If the model is excited with a plane-wave, despite the scattering on the hard-soft wall transitions that excites higher order modes, the position of the microphones will not play any role. If, however, all modes are excited at the inlet, then they will propagate and destabilize the solution.

4 EXPERIMENTAL ANALYSIS

The methods for measuring the acoustic impedance of liners under grazing flow described in section 2.4 and validated in Chapter 3 have very specific requirements regarding test apparatus in order to be used.

Most geometrical specifications of the test duct have already been detailed in section 2.4, i.e., a rectangular duct, with a liner sample on one wall, and hard-wall sections before and after the lined section. For the TPM and MMM, microphones are positioned in the hard-wall sections, flush to the duct walls. For the SFM, the microphones are instead positioned on the opposite wall along the liner sample.

In order to evaluate the effects of grazing flow on the liner samples, a flow generation system is required, along with the ability to measure and control the flow speed. Additionally, one needs to generate an acoustic field in the duct. This can be accomplished by a controlled acoustic source, like one or more speakers connected to a signal generation and amplification system.

Based on this set of requirements, a liner test rig was built at the Vibration and Acoustics Laboratory of the Federal University of Santa Catarina. Its specifications relevant to the current work will be described in section 4.1, but more details can be found in ref. [45].

In the test rig, four liner samples similar to those found in aircraft engines, comprised of perforated face-sheet, honeycomb core and solid back-plate, were measured under different flow speeds. The acquired test data were post-processed and used as input to the MATLAB routines that implemented the impedance eduction techniques.

For one of these liner samples, test data were available for calculating its impedance using the TPM, the MMM and SFM. These results will be presented in section 4.3. For the remaining, however, only the microphones on the hard-wall sections were available. Therefore, their impedance was calculated using only the MMM and the TPM. Because these results are qualitatively similar to those shown in section 4.3, they are instead presented at Appendix B.

In the ending section of this chapter, section 4.4, the measured impedance of the four different liner samples will be compared to predicted values using the models described in section 2.3, i.e., the K&S, E&B and M&K predictive models.

4.1 Liner Test Rig

The test rig built at the Federal University of Santa Catarina is made of several modular, interchangeable sections, as illustrated in Figure 4.1.

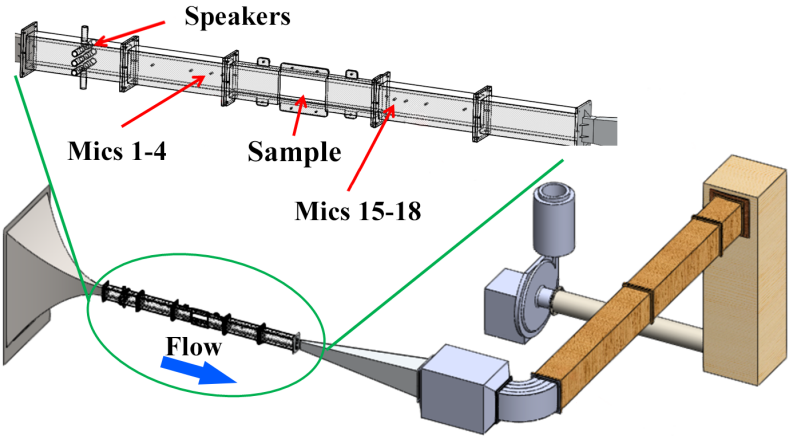

Figure 4.1 – Overview of the test rig, highlighting the test section parts. The liner section shown is the one without the SFM microphones. Adapted from [45].

The test section consists of 5 ducts, whose position can be switched to accommodate different test configurations. For instance, the source section, where the speakers are connected, can be positioned upstream (closer to the nozzle) or downstream (closer to the fan) of the liner sample in order to use the two-source technique for TPM measurements. There are 8 compression drivers for the test rig, which are able to generate sound pressure levels exceeding 140 dB at the test section.

The sections before and after the sample section are the two microphone sections where the TPM and MMM microphones are mounted. Microphone coordinates are the same as in the numerical model of Chapter 3, given in Table 3.1. Eight 1/4" microphones are available to be used in the corresponding sections, depending on the method.

The liner section consists of a straight duct with an opening where the liner sample is positioned. There are two versions of it: one with a plain opposite wall, used for the TPM and MMM measurements, and one with 10 microphone mountings in the opposite wall, used for

the SFM measurements. When measuring for the SFM, the same eight 1/4" microphones are used, and the two remaining mountings (the first and last) are shut.

Just like in the numerical model, the liner sample is 0.20 m long, covering the entire duct height. The cross-section of the test section is 0.04 m by 0.10 m, which results in a no-flow cut-on frequency of 1700 Hz for the first transverse mode, as per Equation 2.34.

The test rig is assembled inside a reverberant chamber. A nozzle is installed at the door that connects this chamber to a second chamber. Air is suctioned from the other chamber and into the nozzle, in which it is accelerated up to a desired flow speed within the test section. After the test section, a diffuser slows down the flow to reduce energy losses. It then passes through an acoustic muffler, a few ducts, and another muffler which is connected to the suctioning fan. The two mufflers aim to reduce the noise generated at the fan, preventing it from contaminating the measurements at the test section.

Excitation signal generation, microphone signal acquisition, and controlling of the flow speed, are executed by a custom software implemented in LABVIEW [46]. A detailed description and validation of this system is made by Masson *et al.* [47]. All results shown in this dissertation were made using discrete, sinusoidal excitation, from 500 to 3000 Hz, in steps of 20 Hz. Liners were measured from no-flow (Mach 0) to Mach 0.25, in increments of Mach 0.05.

The flow speed value used in the impedance eduction algorithms is not the nominal value set in the control system. It is later calculated from the acoustic measurements at the microphones using a custom routine described in Appendix C.

4.2 Liner Samples

Four liner samples were available to be measured at the test rig. All of them use the same 19 mm-tall aluminum honeycomb core and 0.8 mm-thick aluminum plates. The main geometrical parameters of each sample are summarized in Table 4.1. Figure 4.2 shows a picture of sample 2 for illustrative purposes.

Table 4.1 – Main geometric parameters of the four tested liner samples.

Liner Sample	d [mm]	t [mm]	L [mm]	σ [%]
Liner 1	1.8	0.8	19	7.42
Liner 2	2.0	0.8	19	9.16
Liner 3	1.8	0.8	19	12.80
Liner 4	2.0	0.8	19	6.28

Figure 4.2 – Liner sample 2.

4.3 Test Results

As mentioned in the beginning of this chapter, SFM results are only available for Liner 4. Since the discussion made in this section is valid for all liner samples, only Liner 4 results will be presented here. The remaining results can be found in Appendix B.

All liners were measured in no flow-condition and at Mach numbers 0.05, 0.10, 0.15, 0.20, and 0.25. Results for Liner 4 can be seen in Figures 4.3-4.8.

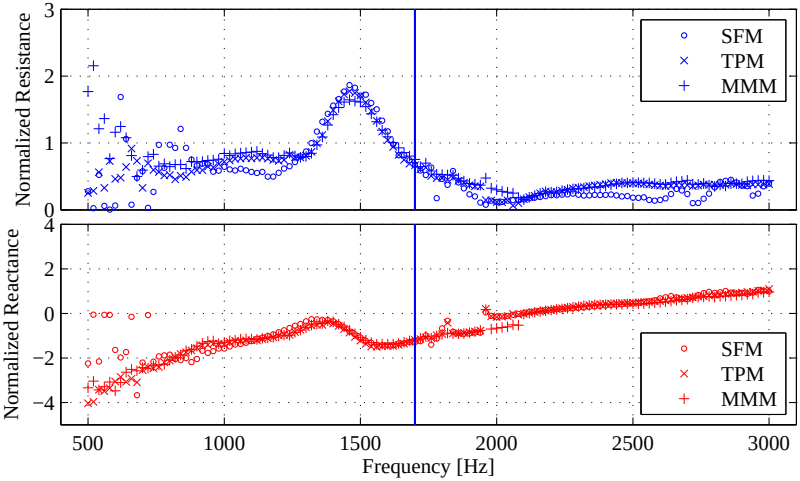

Figure 4.3 – Liner 4 impedance results in no-flow condition.

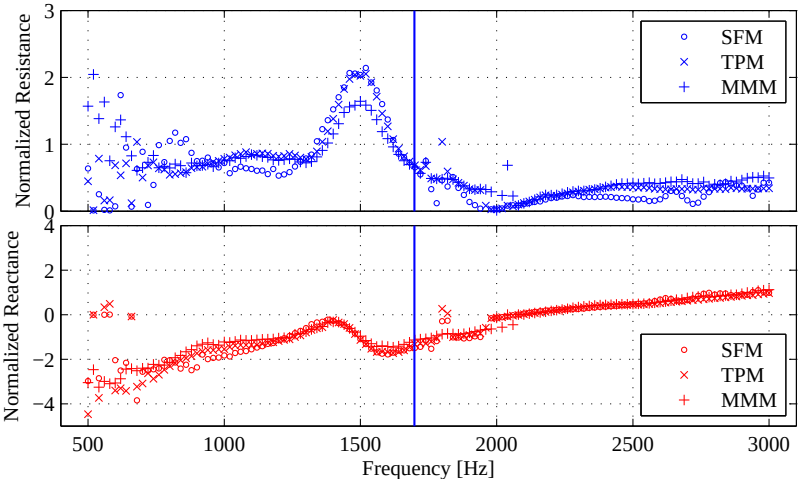

Figure 4.4 – Liner 4 impedance results in Mach 0.05 condition.

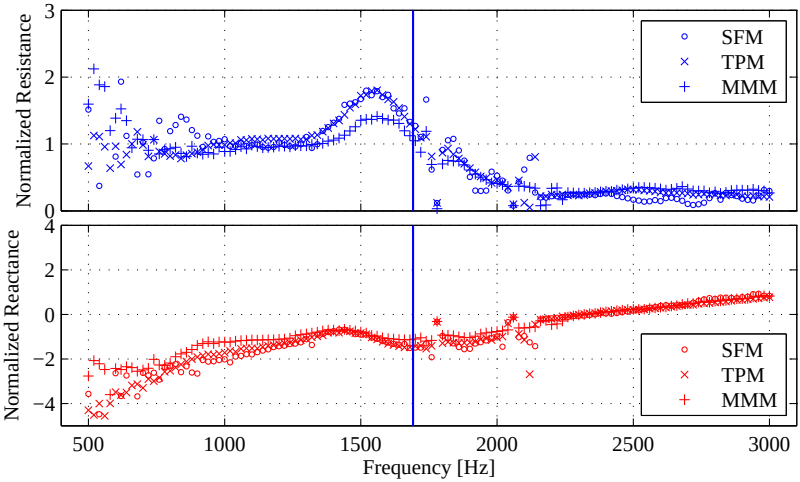

Figure 4.5 – Liner 4 impedance results in Mach 0.10 condition.

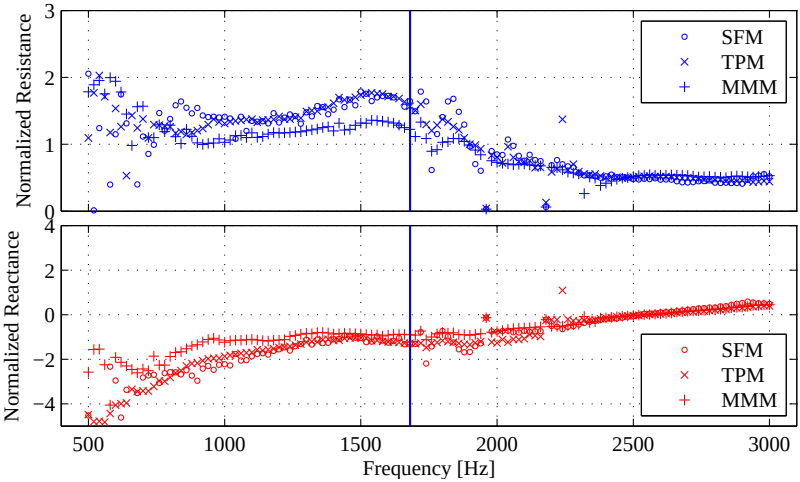

Figure 4.6 – Liner 4 impedance results in Mach 0.15 condition.

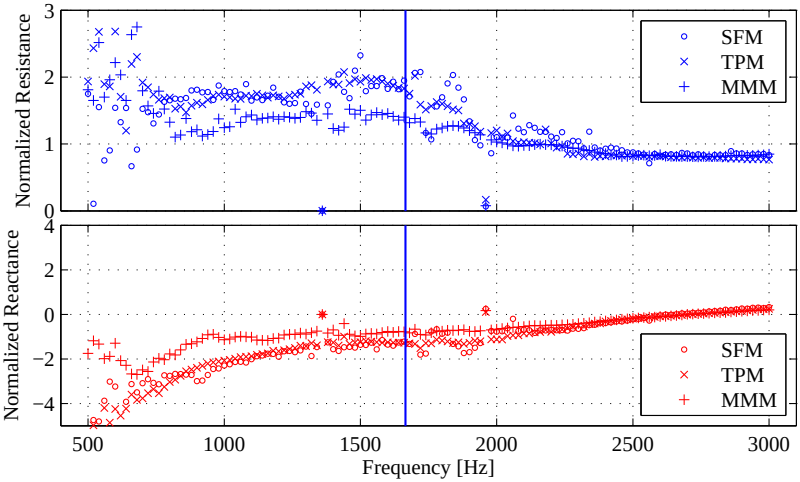

Figure 4.7 – Liner 4 impedance results in Mach 0.20 condition.

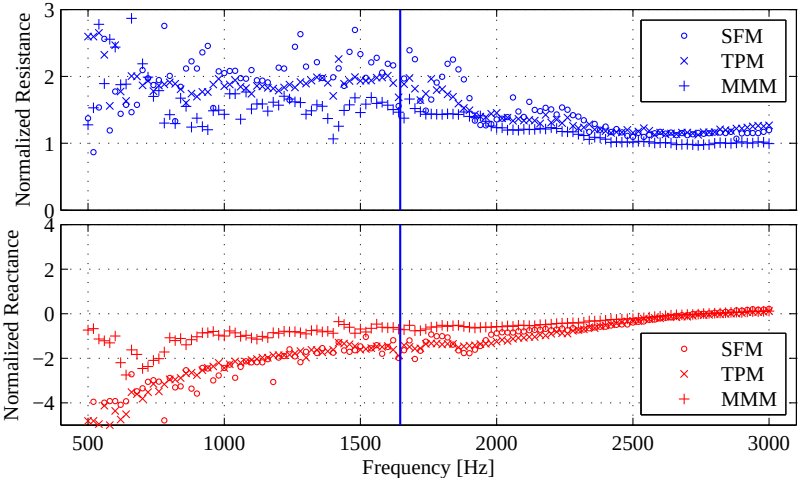

Figure 4.8 – Liner 4 impedance results in Mach 0.25 condition.

No-flow results, seen in Figure 4.3, show a very good agreement between the SFM, TPM and MMM, especially for frequencies above 1000 Hz, and even above the duct cut-off frequency. TPM and MMM resistance results are closer at the higher frequencies, while the SFM oscillates, which does not happen for the reactance. At the lower frequency range, 500 Hz - 1000 Hz, there is some dispersion, without a clear trend for any of the methods.

For higher flow speeds, the results start diverging from each other. It gets worse with flow speed, as can be seen in Figure 4.8, where there is a clear distance between the methods. Generally speaking, SFM results look closer to the TPM then to the MMM. This is easily seen in the higher flow speed result. On the reactance, TPM and SFM results are hardly distinguishable, while the MMM results are easily identified up to 2500 Hz, from where they start converging to the other methods.

Worth noticing is the validation of the assumption that the liner behavior changes with flow, which is visible in these results. The impedance changes significantly even with a 0.05 increase (around 17 m/s) in the mean flow Mach number. The reactance is reduced by the flow, while the resistance is greatly increased. This behavior corroborates what was seen in the predictive models: the flow increases viscous losses at the perforations, which dominate liner resistance, but takes away some of the oscillating mass at the perforations, thus reducing the inertial effects.

Another interesting effect is the shift in the resonant frequency with flow. Going back to the mass-springer system analogy, a mass reduction would increase its resonant frequency, which is marked, for Helmholtz resonators, by the change in the signal of the reactance. In the no-flow result the reactance curve reaches zero at approximately around 2100 Hz; for Mach 0.10, this value goes to 2300 Hz; at Mach 0.25, it is over 2700 Hz. A 600 Hz increase in the resonant frequency is significant, and should be foreseen when designing a liner sample for a specific flight condition in order to achieve maximum performance.

4.4 Comparison of Predictive Models with Test Results

In the last section, the three impedance measurement methods were compared and found to give similar results in most cases. Since the TPM and the SFM appeared to agree better then they agreed with the MMM, and the TPM results are smoother then the SFM, in this

section the TPM results will be used as a reference to compare the liner predictive models described in section 2.3.

Figures 4.9 to 4.12 show the TPM result at every flow speed for liners 1-4, together with the K&S, E&B and M&K results. Since the test rig does not currently allows control of the incident SPL on the liner sample, the actual measured SPL spectra was used to calculate the incident velocity for non-linear terms on the E&B and M&K models.

When looking at the test results, care must be exercised, as one should look at its overall behavior, not the actual value at each frequency, since there are outliers at several frequencies that are most likely caused by error in test data or instabilities in the impedance calculation procedure.

One particular feature of the experimental results for all liner samples is a "bump" in the resistance at lower flow-speeds at around 1400-1600 Hz (depends on the liner sample), accompanied by an wave-shaped form in the reactance whose center is exactly at the peak of the resistance bump. As the flow speed increases, these peaks vanish.

One possibility is that they are not actually vanishing, but simply being hidden as the resistance grows with the flow speed. Since none of the models predict these bumps, they are not believed to be caused by the main, expected physical mechanisms involved in liner attenuation, but by some secondary dissipation mechanism, for instance, a structural mode of the liner sample excited by the acoustic field. When flow speed is increased, the structural mode does not change, but viscous losses grow and dominate the resistance, therefore masking the bumps. More research is advised in order to better understand the cause of these bumps.

In the following sections, the results obtained by each model will be discussed. Generally speaking, all methods gave satisfactory reactance predictions for all liners and flow speeds. Resistance results, however, were underestimated at low frequencies and low flow speeds, but agreed well for higher frequencies.

4.4.1 Kooi & Sarin liner impedance model

The K&S model, seen in green on Figures 4.9 to 4.12, gives good reactance predictions in all test cases, being always between the M&K and E&B results. Its reactance curves also seem to follow the change in the samples' reactance with flow speed. Its resistance results, however, severely underestimate the measured values at lower frequencies.

As flow speed increases, the K&S resistance grows together with the measured resistance, thus keeping the gap between them.

This was the only model between the three tested that correctly predicted the negative slope of the resistance at higher flow speeds, i.e., a resistance that reduces with frequency.

In a per-liner analysis, the K&S gave better predictions for Liners 1 and 4, which are the two lowest-porosity liner, at respectively 7.28% and 6.42%. Maybe not coincidentally, the average porosity of the five liner samples used in the Kooi and Sarin study was 6.71%. This might indicate that there is some sort of valid porosity range for the K&S.

4.4.2 Motsinger & Kraft liner impedance model

The M&K model, depicted in magenta in the results, gave the lowest resistance predictions for the tested liners and flow conditions, at lower frequencies. At higher frequencies the resistance agreed well with the measurements, and as flow speed increased, it closely accompanied the measured resistance.

Low frequency resistances, however, were the only one between the three models that did not grow with the flow speed, what did happen in measured results and is expected because of increase in viscous losses at the orifices.

This weakly dependence on the flow speed happens because the only term in Equation 2.17 that actually varies with flow speed is the incident acoustic velocity. Because it is calculated iteratively based on the impedance, and the reactance does vary with flow speed (through the end-correction term), the incident velocity changes for different flow speeds, thus leading to a slight increase in higher-frequency resistance.

The reactance predictions for the M&K were the highest (or lowest, in absolute terms) between the three models. For the low frequency range (before the "bump"), this meant that its results were very close to the measurements, especially at higher flow speeds. After the bump, however, the measured reactance was a little lower, and further away from its predictions.

4.4.3 Elnady & Bodén liner impedance model

The E&B model was based on a comprehensive analysis of multiple previous models and fifty liner samples, including some with spec-

ifications very close to the ones used in the current analysis. Despite that, its resistance results also did not agree well with the test data.

With the increasing flow speed, the E&B resistance increased much faster then the test results. Therefore, despite underestimating no-flow resistance, at higher flow speeds it actually reached the measured low frequency resistance. And with no negative slope at higher flow speeds, it severely overestimated the high frequency resistance for all liners but sample 3, which showed high resistance in the test results despite its high porosity.

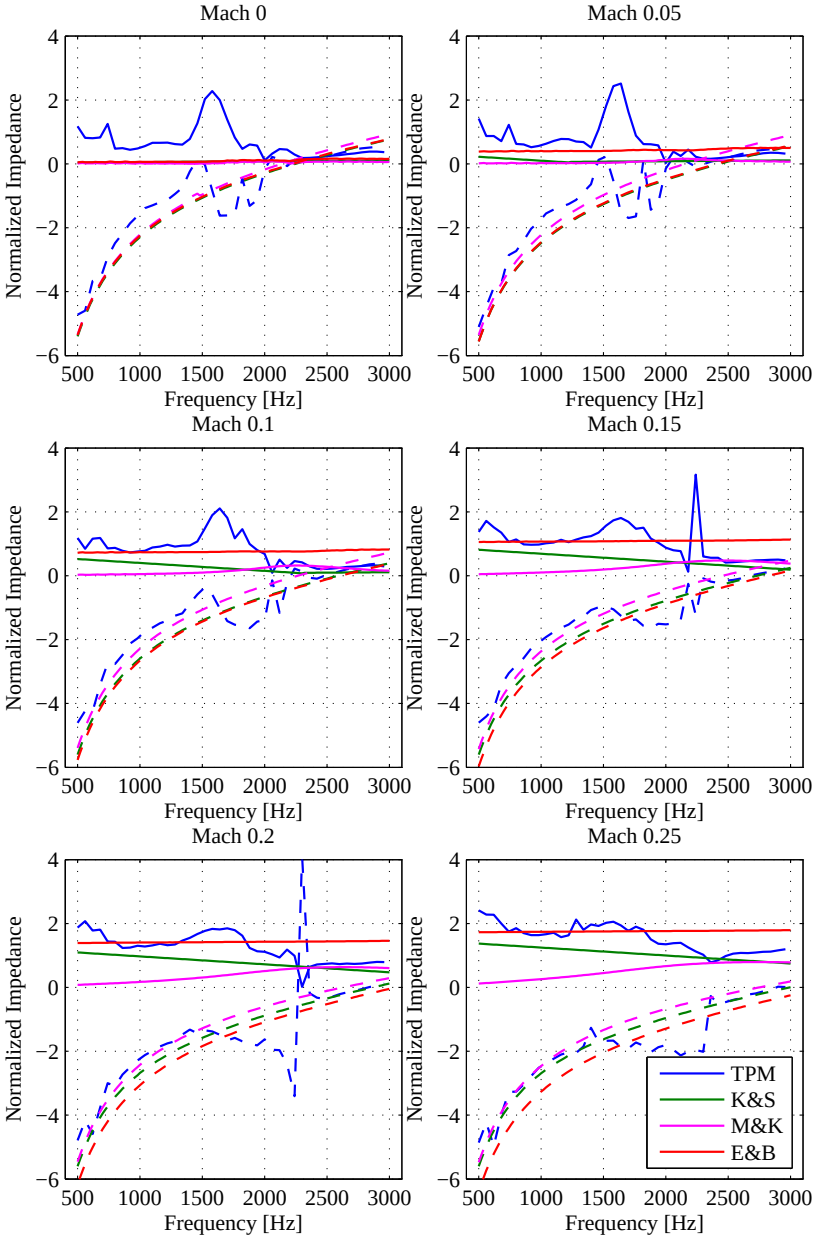

Figure 4.9 – Liner 1 - Comparison of Predictive Models and Measurements at different speeds. Solid lines are resistance values and dashed lines are reactances values.

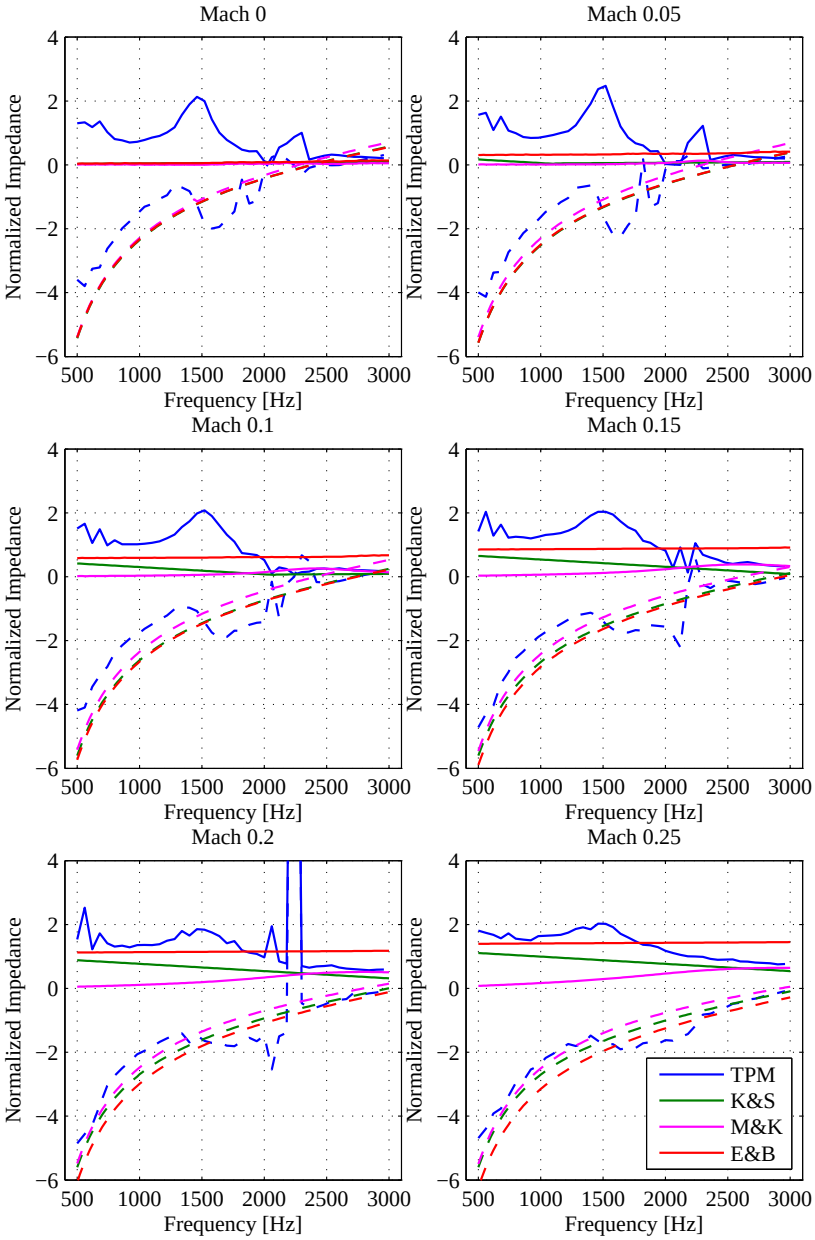

Figure 4.10 – Liner 2 - Comparison of Predictive Models and Measurements at different speeds. Solid lines are resistance values and dashed lines are reactances values.

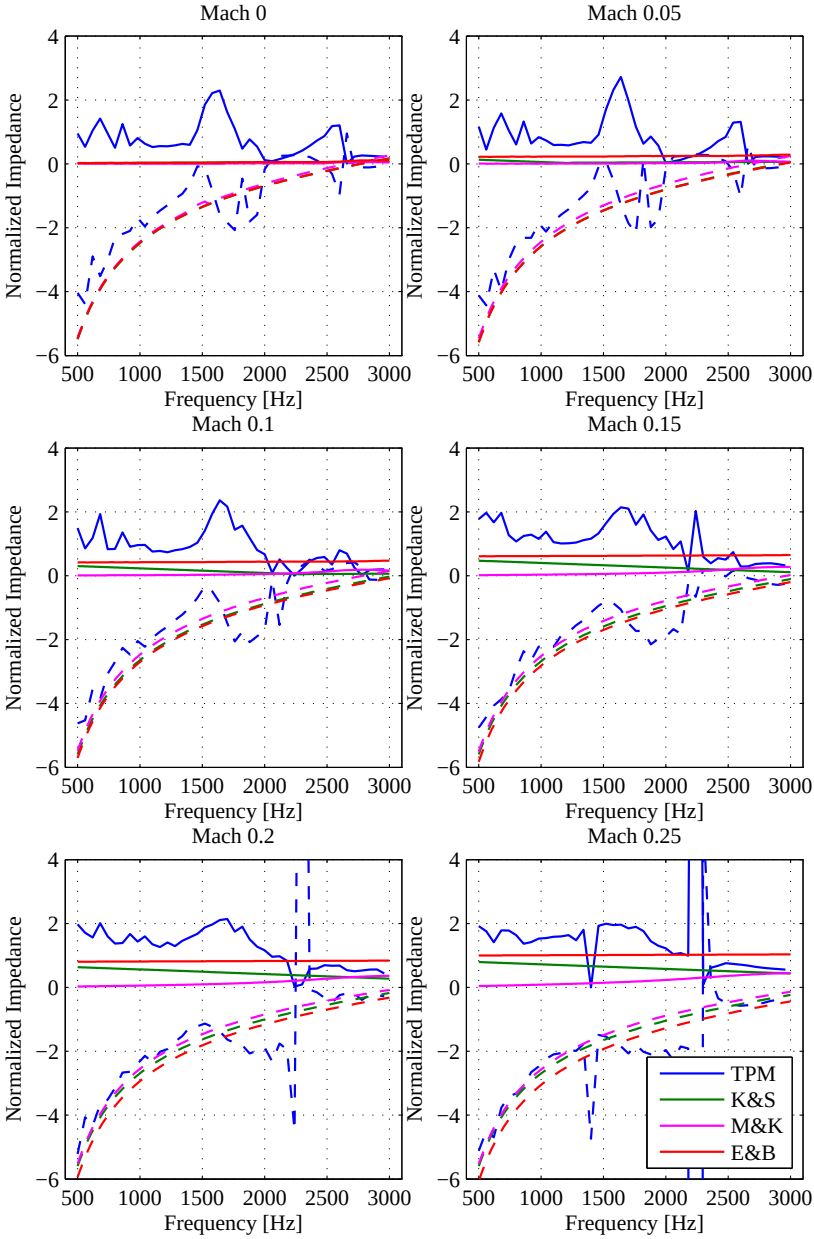

Figure 4.11 – Liner 3 - Comparison of Predictive Models and Measurements at different speeds. Solid lines are resistance values and dashed lines are reactances values.

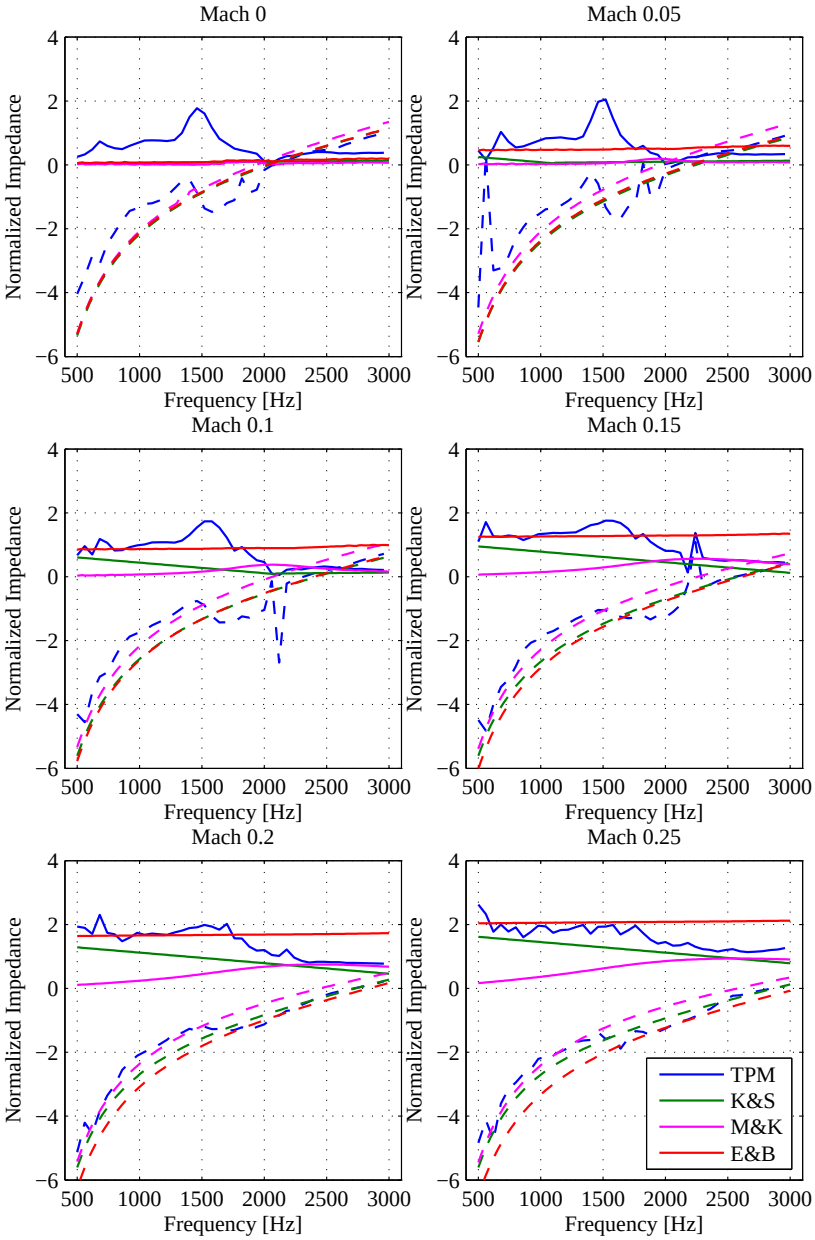

Figure 4.12 – Liner 4 - Comparison of Predictive Models and Measurements at different speeds. Solid lines are resistance values and dashed lines are reactances values.

5 PARAMETRIC IMPEDANCE EDUCTION

The inverse impedance calculation methods seen on this dissertation, the TPM and the MMM, relied on an optimization procedure in order to find the impedance that best reproduced the acoustic field in a duct with a liner sample. Since the impedance is a function of frequency, the acoustic field is measured at different frequencies so that the impedance behavior is fully characterized.

In their current form, the TPM and the MMM loop through the frequencies, finding the best-fitting impedance at each of them. No relation is forced between the impedance at adjacent frequencies, thus the optimization at a given frequency runs completely independent from the other frequencies' results.

By doing a visual analysis of the results, however, one can easily identify some points as not being correct, since the impedance should generally be a smooth function of frequency, with no abrupt spikes or discontinuities. This is seen also on the numerical validation results when higher order modes were cut-on, and some frequencies did not converge to the imposed value.

In this chapter, a new method will be proposed that incorporates physical characteristics of the liner materials in order to obtain smooth curves in frequency. In section 5.1, one of the reasons for the observed discontinuities will be discussed, and in the following section the new method will be described. In section 5.3, a numerical validation similar to the one made in Chapter 3 will be conducted with the proposed method, and finally in section 5.4 the test data from Chapter 4 will be used to assess the advantages and drawbacks of the new method.

5.1 Local Minima and Basins of Attraction

A commom problem for optimization-based methods is that their objective functions[1] might have multiple, local minima, which satisfy the optimization's stop criteria, but are not the correct, physical result. Since the optimization algorithms used are usually gradient-based, with a single initial point, they tend to converge to the closest minimum, which might be one of the non-physical minima.

[1] Objective function is the function to be minimized by the optimization procedure. For the impedance eduction methods, it is usually given by the difference (error) between the measured and the calculated acoustic field.

This problem is best explained using the concept of *basins of attraction* [33]. For illustration purposes, take the hypothetical function, $f(x)$, shown in Figure 5.1. In the visible range of x, the function has two local minima, one in the grey region at $x = x_1$, and one in the green region, at $x = x_2$.

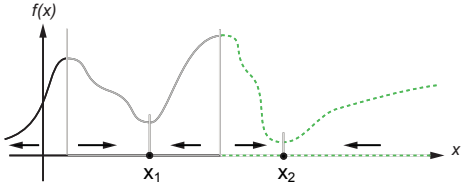

Figure 5.1 – Illustration of the basins of attraction concept. Different basins of attraction are represetend in different line styles. Adapted from [48].

Now suppose $f(x)$ represents a function of some physical quantity x whose minimum is to be found, and problem heuristics indicate that negative values are not possible for this quantity to assume. The correct minimum to be found, then, is the global one, x_2.

When using a gradient-based optimizer, the function gradient is used to find the direction of the steepest descent, i.e., the direction in which x should go for $f(x)$ to decrease the quickest. If a starting point for the algorithm is chosen anywhere in the grey region, the direction of steepest descent always point to the local minima in its center, x_1, to which the algorithm will converge. On the other hand, if the starting point is chosen anywhere in the green region, the direction of steepest descent always points to x_2.

The grey and green regions form what is called a *basin of attraction* to their minima. One way around this problem is to seed multiple starting points and run the local optimizer at each one of them, keeping the result of the lowest objective function value. This of course does not guarantee convergence to a global minimum (if it really exists[2]), but increases the chances of finding one in case the starting points are well distributed across the domain. This is well-known and used by optmizers that focus on finding global minima of functions.

[2]Some functions do not have a unique global minimum, but several of them, for instance, $\cos(x)$, which has multiple global minima at $x = \pm\pi$, $\pm 3\pi$, $\pm 5\pi$, etc. Other functions only have a global minimum on limited intervals, like x^3. For an unbounded domain, x^3 grows to $\pm\,\mathrm{inf}$.

5.2 Parametric Impedance Eduction

When using data obtained from measurements, the problem of convergence to local minima is aggravated, because experimental error can mask minima or create other minima to which the optimization might converge. This creates problems as seen in the test results of the TPM and MMM on Chapter 4, where the impedance at single frequencies do not converge to the expected results, despite many other correctly converging frequencies.

In this section, a modification to the Mode-Matching Method is proposed. In the original version, described in section 2.4.3, the objective function, at each frequency and for a given impedance guess, is given by the sum of the squared percentage error between between measured and calculated acoustic pressure at the n-th microphone position, as in:

$$e(f, Z) = \sum_{n=1}^{k} \left(\frac{p_{n,meas}(f) - p_{n,calc}(f, Z)}{p_{n,meas(f)}} \right)^2. \tag{5.1}$$

If the impedance at n_f frequencies are to be found, that represents a total of $2n_f$ independent variables, since the impedance is a complex variable.

The optimization problem could be rewritten to take into account a frequency-dependent impedance function $Z(\mathbf{x}, f)$, that gives the impedance for all frequencies for a given set of parameters $\mathbf{x}$. The acoustic field, then, is calculated using the impedance for each frequency, and the objective function, Equation 5.1, becomes a function of $\mathbf{x}$, and is summed over all frequencies to give the global error, according to:

$$e(\mathbf{x}) = \sum_{f=f_0}^{f_{n_f}} \left(\sum_{n=1}^{k} \left(\frac{p_{n,meas}(f) - p_{n,calc}(f, Z(\mathbf{x}, f))}{p_{n,meas(f)}} \right)^2 \right). \tag{5.2}$$

The parameters in vector $\mathbf{x}$ are the new optimization variables, which are varied to minimize $e(\mathbf{x})$. By finding $\mathbf{x}$, the impedance is defined for all tested frequencies, solving a single, but larger, optimization problem. This new method will be hereafter called the Parametric Mode-Matching Method (P-MMM).

It can be seen in the higher order validation results of section 3.2 that most frequencies do converge to the correct solution, in the original form of the MMM. If one considers that the order of magnitude

of the incorrect and correct minima in frequencies that do not converge is similar, then by using a physically possible, smooth in frequency $Z(\mathbf{x}, f)$ function, it is expected that the already converging frequencies will dictate the convergence of $Z(\mathbf{x}, f)$ to the correct results.

The model for $Z(\mathbf{x}, f)$ used in the present work was the Extended Helmholtz Resonator model, given by Equation 2.28. In this case, the vector $\mathbf{x}$, which define the impedance for a given frequency and is to be found by the optimization, is given by 8 parameters:

$$\mathbf{x} = (\theta_0, \chi_0, f_0, m, \xi, \nu, C_{im}, \Delta_f), \tag{5.3}$$

where θ_0 and χ_0 define the design impedance at frequency f_0 ($f_0 = \omega_0/2\pi$), Δ_f is a frequency-shift and C_{im} is a constant added to the imaginary part, both included in the model as new degrees of freedom for the optimization. The remaining parameters of Equation 2.28 are calculated from equations 2.30 to 2.32[3].

Bounds are applied to the variables in order to limit the solution domain and reduce the occurrence of unfeasible impedance values. For instance, negative or too high resistances, oscillating curves, and other problems can be avoided. Some of these bounds were defined empirically, through trial and error, while care was taken not to overly limit the possible curves to be generated by Equation 2.28. The defined upper and lower bounds for all parameters are given in Table 5.1.

Table 5.1 – Upper and Lower bounds for the optimization variables in the P-MMM.

	θ_0	χ_0	f_0	m	ξ	ν	C_{im}	Δ_f
Upper bound	10	1	1500	20	4	1.10^3	15	5000
Lower bound	0	-15	0	0	-1	-1.10^{-3}	-15	0

The MMM was chosen as a base for this modification instead of the TPM because in this last, besides the impedance, there is also the $[T_{tr}]$ transition matrix to be found at each frequency, which has no parametric, straight-forward, analytical model. It would have to be found for each frequency nonetheless, defeating the purpose of a parametric impedance eduction.

[3] One of the assumptions on the derivation of equations 2.30 to 2.32 is that $m = 0$. Since m is now being found by the optimization and new terms were added, there is no guarantee that the resulting impedance will satisfy the design impedance $Z(\omega_0) = \theta_0 + j\chi_0$.

5.3 Numerical Validation

The numerical validation of the TPM, MMM, and SFM, described in Chapter 3, was also conducted for the P-MMM. The same FEM models and the corresponding data were used, since no new requirements were introduced by the P-MMM as compared to the MMM. Again, three cases will be tested: no-flow, Mach 0.2, and Mach 0.3.

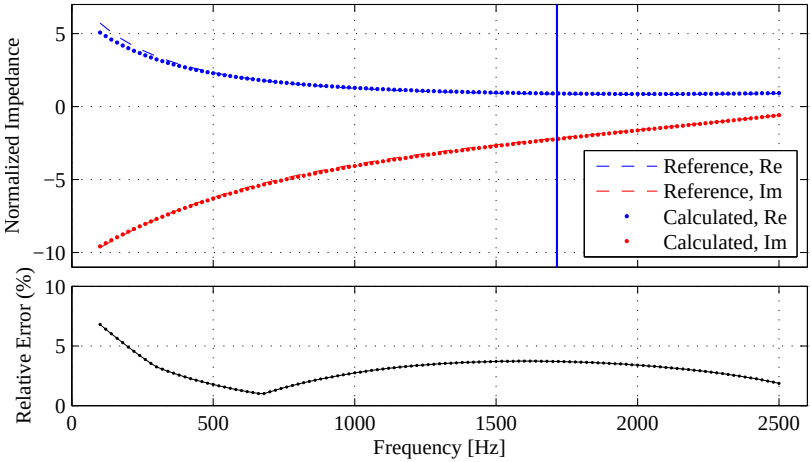

Figure 5.2 – Normalized impedance and relative error obtained with the P-MMM for the no-flow validation result.

The result for the no-flow case, seen in Figure 5.2, shows that the P-MMM was able to find the imposed impedance with an average error around 4%, a very similar value to the one found on the original MMM results. On the flow test cases, the behavior is not different. A smooth result, with low relative errors, around 4% - 5%, comparable to the other original form of the MMM and the other validated methods.

The greater number of variables in a single optimization problem increases the computational cost because of the much larger solution space to be searched and the more costly gradients estimation. Additionally, the Multi Start [48] global optimization algorithm is being used. It works by seeding several starting points for the optimization and running each of them in parallel with a gradient-based local optimizer. This increases solve times but also the chances of a finding a good result. All that contributed to a total solve of time of around 750

seconds for each case seen here, which is considerably more then those of the original MMM or TPM, seen in Table 3.2.

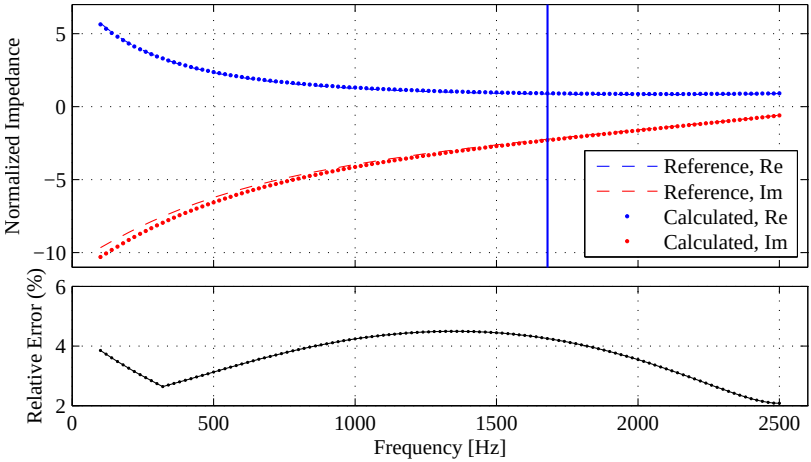

Figure 5.3 – Normalized impedance and relative error obtained with the P-MMM for the Mach 0.2 validation result.

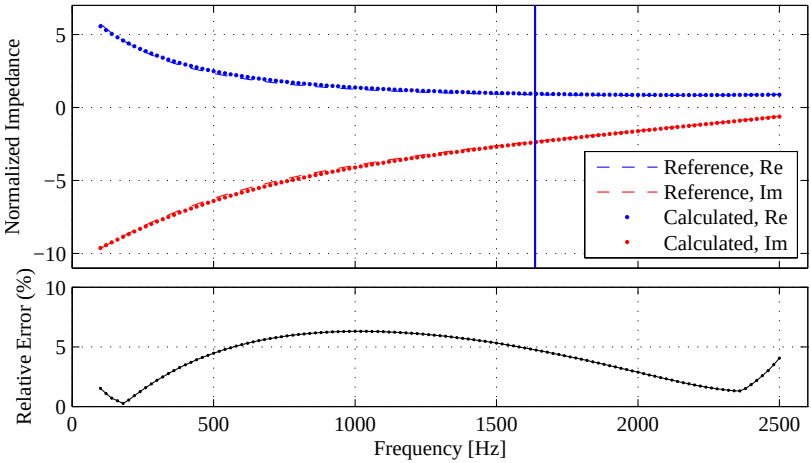

Figure 5.4 – Normalized impedance and relative error obtained with the P-MMM for the Mach 0.3 validation result.

5.3.1 Higher Order Modes

The numerical validation results, despite being encouraging for the new method, were expected, since none of the methods had problems in the numerical validation of Chapter 3. Even though they do not relied on a smooth function of frequency, each frequency converged to the correct results, which naturally resulted in a smooth curve.

In section 3.2, however, all three methods showed unstable results for frequencies higher then the the duct cut-off frequency when higher order modes were used to excite the model, and microphones were not centered in the duct height. It is interesting, then, to check if the introduced modification makes the method any more robust to handle this situation. The worst-case scenario is used for this test, i.e., the same model used for Figure 3.14, where microphones are at $x = 0.015$ m (outside the nodal position of the first transverse mode) and all modes are used to excite the model. The result can be seen in Figure 5.5, compared to the original MMM result and to the imposed impedance value, to which they should converge.

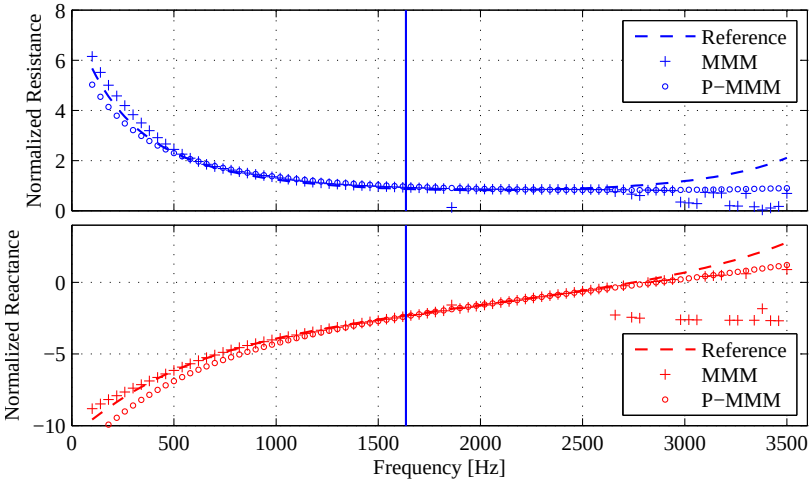

Figure 5.5 – Comparison of P-MMM and MMM results in the presence of higher order modes and with microphones at $x = 0.015$ m. MMM result is the same of Figure 3.14.

It can be seen that, at several frequencies where the MMM solution was unstable, the P-MMM kept a smooth behavior, even though

both results are diverging from the reference at higher frequencies.

This result confirms the hypothesis of section 5.2, that correct and incorrect minima probably have the same order of magnitude and thus correctly converging frequencies would dictate the convergence of the entire curve. The few points that posed problems for the MMM because of multiple, similar minima, were led to the correct result because they fit the curve dictated by the other points.

To better understand the difference between the P-MMM and the reference values, it is interesting to look at the value of the objective function, Equation 5.1, at each frequency. Figure 5.6 shows Equation 5.1 calculated for the correct impedance, i.e., the reference curve imposed on the FEM model, and for P-MMM educed impedance.

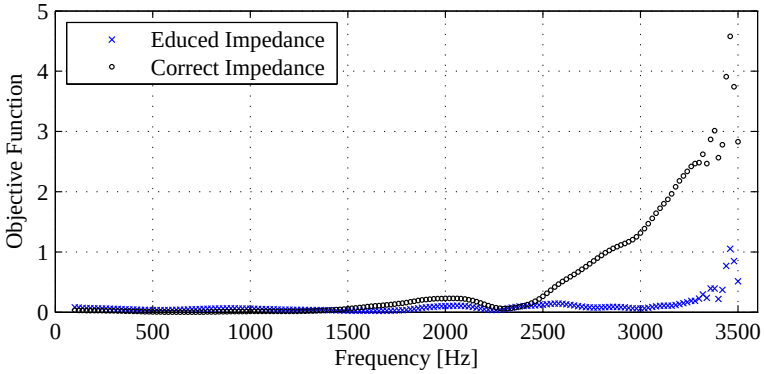

Figure 5.6 – Objective function value at each frequency for the correct (imposed) and the educed (found by the P-MMM) impedance.

Figure 5.6 shows that the optimization converged to an impedance other than the correct one because the educed impedance actually results in objective function values lower then the correct impedance, especially for frequencies above 2500 Hz. For illustrative purposes, if the summation over frequency of Equation 5.2 is performed for each case, it gives 90.45 for the correct curve, and 16.14 for the educed one.

To put it another way, the acoustic field calculated with the Mode-Matching scheme using the educed impedance is closer to the FEM-simulated field then the one calculated with the impedance imposed in said FEM model. The same situation was seen in the TPM and MMM results on the higher-order modes analysis of section 3.2,

even for the other excitation/microphone position cases.

This might have two possible causes: differences between the Mode-Matching and the ACTRAN code, including assumptions and simplifications, for instance, the presence of the higher-order modes in the hard-wall sections, generated by scattering or excited by the BC, which might be more relevant at higher frequencies; and the deterioration of the discretization of the FEM mesh as frequency increases, which for 3500 Hz and Mach 0.3 has only 13 elements per wavelength.

5.4 Experimental Data

The last test for the modified MMM is to run it using experimental data obtained at the test rig. This input data is the same used in Chapter 4, on the comparison between the SFM, TPM, and MMM. They were measured with liner sample 4, without flow and from Mach 0.05 to Mach 0.25. The results are presented in Figures 5.7 to 5.12, together with the MMM results, for comparison.

Overall, good agreement is seen between the P-MMM and the MMM results. Some advantages of the P-MMM implementation are clearly seen, like the smoother, more stable results over frequencies, and the avoidance of the small jump in the reactance, generally accompanied by a dip in the resistance, that happens at the lower flow speeds around 2100 Hz.

From Mach 0 to Mach 0.15, a similar shape dominates the results. This is the "bump" shape, commented in Chapter 4. Here, however, it keeps the lower frequency resistance much lower then on the MMM results (and also the TPM and SFM of Chapter 4). This is believed to be caused by a sort of "least-squares", compromise solution to the problem by the optimization, improving medium and higher frequencies while slightly deteriorating lower frequencies. Better initial guesses, different boundaries, or even a different impedance model might help improve the possible shapes for the solution.

For Mach 0.20 and 0.25, the shape of the impedance changes, and the bump shape is no longer seen. In the first case, Mach 0.20, a "wave" shape, that somewhat fits the MMM results, is noted in the resistance. This improves the lower-frequency results, which are now closer to the MMM and, consequently, to the TPM and SFM.

At Mach 0.25, the traditional liner impedance shape, common in the literature, is seen: a decreasing resistance and an increasing reactance - similar to the K&S predictions of the previous chapter.

Both the resistance and reactance were reasonably larger, in absolute terms, then the MMM's result. In fact, this makes the P-MMM results closer to SFM and TPM Liner 4 results, since the MMM results were also lower then the other two methods', as can be seen on Figure 4.8.

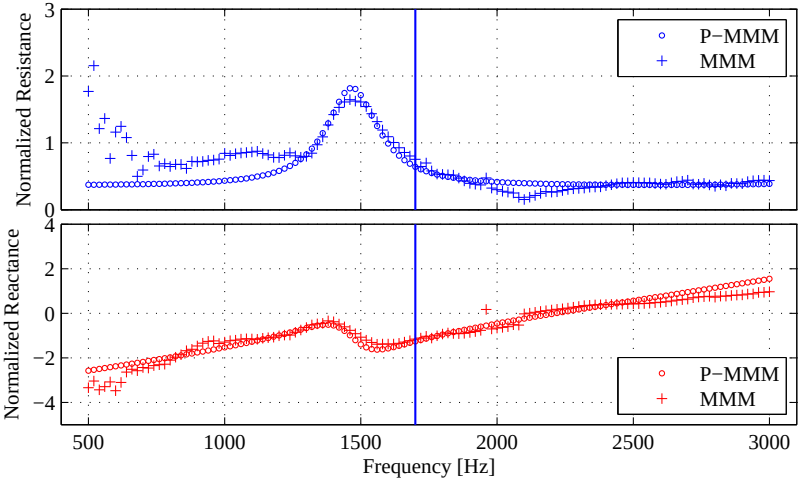

Figure 5.7 – Liner 4 P-MMM test result in no-flow condition.

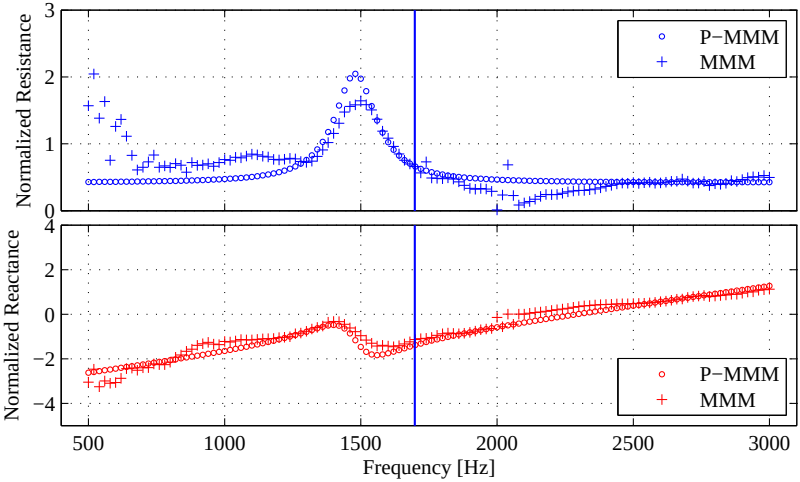

Figure 5.8 – Liner 4 P-MMM test result in Mach 0.05 condition.

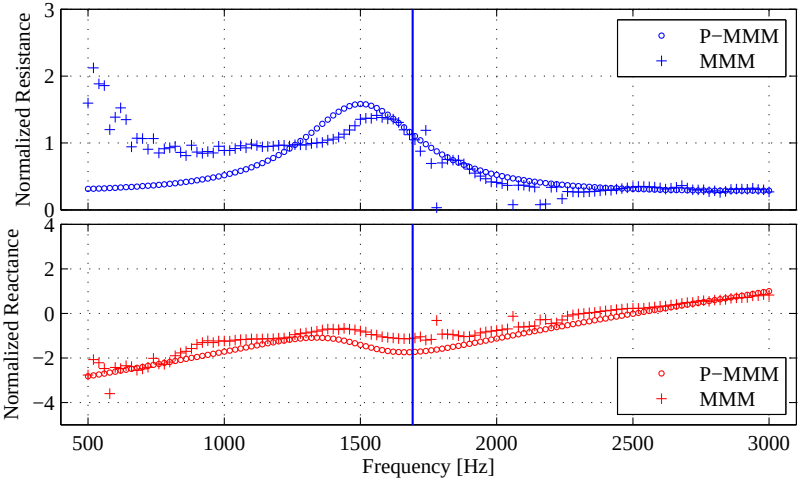

Figure 5.9 – Liner 4 P-MMM test result in Mach 0.10 condition.

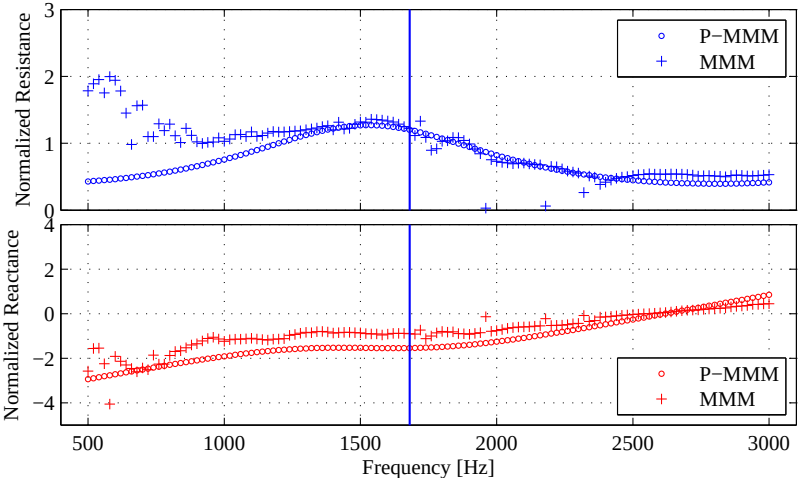

Figure 5.10 – Liner 4 P-MMM test result in Mach 0.15 condition.

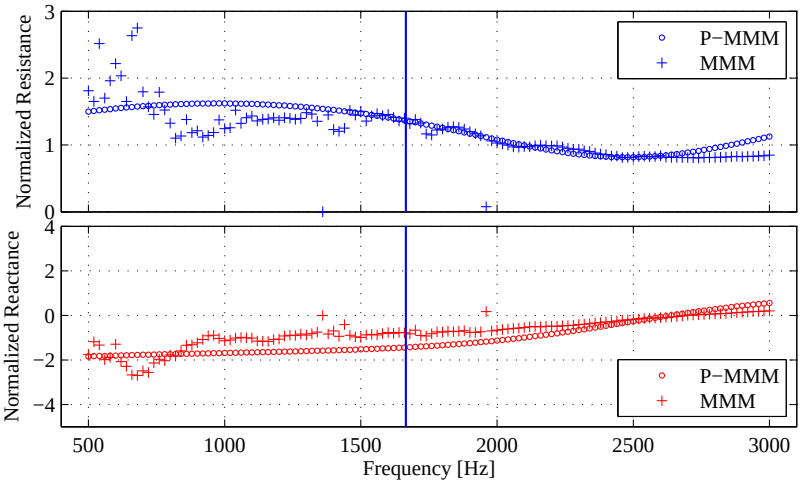

Figure 5.11 – Liner 4 P-MMM test result in Mach 0.20 condition.

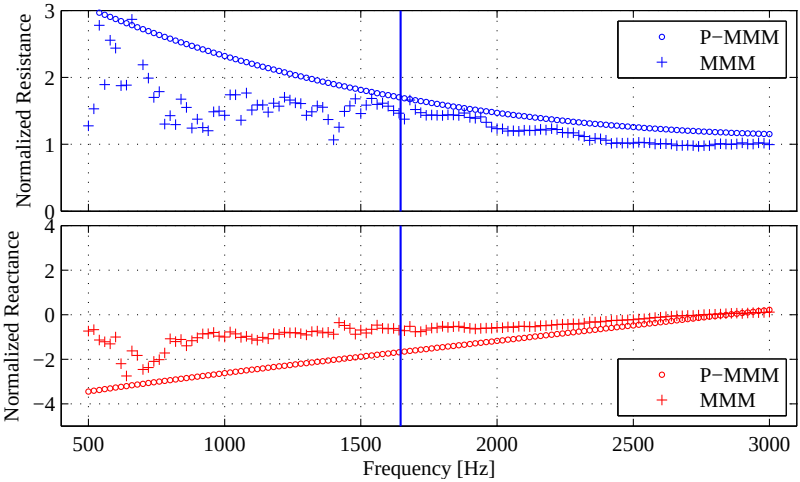

Figure 5.12 – Liner 4 P-MMM test result in Mach 0.25 condition.

6 CONCLUSIONS AND FUTURE WORK

6.1 Conclusions

In this work, three published techniques for measuring the acoustic impedance of liners under grazing flow were evaluated. These were the Two-Port Method (TPM), the Mode-Matching Method (MMM) and the Straight-Forward Method (SFM).

In Chapter 3, the three methods were tested using input data from Finite Element Method simulations. They successfully found the imposed impedance in all conditions within good tolerances.

The TPM results were only marginally better then the MMM for all flow speeds and frequencies, with the former also being more computationally expensive, taking three times longer then the MMM to solve one test case. Besides computational cost, the MMM was also advantageous regarding input data, since one source position is sufficient, while the TPM requires the use of the two-source technique. When comparing the two indirect methods to the SFM, the last showed very promising results, which took less then a hundredth of the time of the other methods to be calculated. However, its errors were much larger in the lower frequencies, where it is believed the method is prone to contamination of the microphone measurements by the transition effects in the presence of flow. This transition problems also show on the MMM results, albeit in a smaller scale. For the TPM this effect is almost negligible, probably because it is handled by a transition element.

In the numerical validation results, it was noticed that the methods were able to find the imposed impedance even at frequencies where the first transverse mode of the duct was cut-on, which was unexpected. However, the microphones in the models were centered on the duct walls, coinciding with the nodal line of the first transverse mode. That raised the hypothesis that the methods worked above the cut-off frequency because this first mode was not actually being measured. To confirm that, new models were built testing different excitations and offsetting the microphones. For one combination, where microphones were offset and all modes excited the model, the methods returned unstable results.

This result shows that the design of a test rig for measuring liner impedance with one of these methods must be carefully considered, since different modes are likely to be excited. To avoid at least the

first transverse mode in case it is cut-on, the microphones might be positioned at its nodal line. If however higher-order modes are cut-on and the microphones are in a position other then the recommended one, good results might be harder to achieve.

When using experimental data from a grazing flow test rig, the methods showed good agreement. An unexpected bump was seen around 1500 Hz at lower flow speeds, which is believed to be caused by a secondary dissipation mechanism such as a structural mode of the sample. However, more research is needed to better understand it.

The test results for 4 different liner samples were compared to the predictive models described in section 2.3. Overall, the K&S model had the best agreement with the test data, usually underestimating the resistance, and the M&K came next, usually overestimating the reactance at higher frequencies. All three models however severely underestimated the resistance in the absence of flow, which is something to be investigated. It might be that the liner samples have another dissipation mechanism not predicted by these models, which should be looked into. For Mach 0.25, the K&S could probably be used for design and optimization of liners, but with reservations. Resistance errors around 20–40% and reactance errors around 10–20% for most frequencies should be expected.

In Chapter 5, an original contribution of this work, a modification to the MMM, was described. Instead of using an optimization to find the impedance at each frequency, a parametric impedance model in the frequency domain was used, and its parameters became the optimization variables. The resulting technique successfully passed the numerical validation and the more difficult higher-order mode analysis that the other methods struggled with. Its experimental results also agreed well with the other methods, except for lower frequencies resistance at low flow speeds. This however might be due to difficulties in finding the set of parameters of the proposed model that minimizes the objective function.

6.2 Suggestions for future work

Regarding the impedance eduction methods, further work is recommended to improve their computational implementation. The MMM and the TPM might benefit from a more robust optimization algorithm, such as the global minimizer used in the P-MMM, even if that results in longer solve times.

For the SFM, more insight is needed on the physical phenomena on the transition regions, in order to specify more precise requirements regarding the distance from the microphones to the transitions to avoid contamination.

Some of the differences between the imposed and the educed impedance on the numerical validation of Chapter 3 might be due to the FEM mesh used in the simulations. Quadratic interpolation functions could be used to check if the errors are reduced. A mesh convergence study could also be carried-out, calculating the impedance at each mesh refinement step and checking the convergence of the results.

The evaluated predictive models severely underestimated no-flow and low Mach number resistance. Additional research could be carried-out to better understand the no-flow resistance mechanisms on the perforated plate. From that, new terms could be proposed that reduce the gap between experimental and prediction results. Additionally, the bump seen in the experimental results needs further investigation. The hypothesis of a structural mode could be checked by exciting, for instance with an impact hammer, a liner sample mounted on the test rig and measuring its frequency response functions with accelerometers.

For the parametric impedance eduction method proposed, different equations besides the Extended Helmholtz Resonator could be implemented. This might improve convergence if the new equation contains less parameters or provides more freedom for the optimization algorithm to change its shape.

Still for the P-MMM, a term similar to the flow-dependance terms of the predictive models could be added, and its coefficient set as an optimization variable. For a given set of parameters, the acoustic field could be compared to the measurements at different frequencies and flow speeds. By minimizing the difference between them, the set of parameters that give the impedance at all frequencies and flow speeds would be found in a single optimization problem.

The non-linearity of the liner samples is an important phenomenon that was overlooked in the current analysis, mostly because the test rig used in the measurements does not allow for the control of the incident SPL. It is suggested that future works in this line of research implement that capability in the test rig control system. The liner samples could then be measured at different incident SPL so that the relevant terms on the predictive models be checked. These terms could be also incorporated to the P-MMM technique to further integrate the eduction process, characterizing a liner sample at different frequencies, flow speeds, and incident SPL.

REFERENCES

[1] SANTANA, L. D. et al. Two-port indirect acoustic impedance eduction in presence of grazing flows. In: **17th AIAA/CEAS Aeroacoustics Conference 2011**. [S.l.: s.n.], 2011. (AIAA 2011-2868).

[2] ELNADY, T. et al. Validation of an inverse analytical technique to educe liner impedance with grazing flow. In: **Proceedings of the 12th AIAA/CEAS Aeroacoustics Conference**. [S.l.: s.n.], 2006. v. 5, p. 3093–3107.

[3] JING, X.; PENG, S.; SUN, X. A straightforward method for wall impedance eduction in a flow duct. **The Journal of the Acoustical Society of America**, v. 124, p. 227, 2008.

[4] KOOI, J. W.; SARIN, S. An experimental study of the acoustic impedance of helmholtz resonator arrays under a turbulent boundary layer. In: **AIAA-1981-1998**. [S.l.: s.n.], 1981.

[5] ELNADY, T.; BODÉN, H. On the modelling of the acoustic impedance of perforates with flow. **PhD Thesis**, III, 2004.

[6] MOTSINGER, R.; KRAFT, R. Design and performance of duct acoustic treatment. In: **Aeroacoustics of Flight Vehicles: Theory and Practice. Volume 2: Noise Control**. [S.l.: s.n.], 1991. v. 2, p. 165–206.

[7] COMMISSION OF THE EUROPEAN COMMUNITIES. Technical Report, **White Paper - European transport policy for 2010: time to decide**. Brussels, 2001. Disponível em: <`http://ec.europa.eu/transport/themes/strategies/doc/2001_white_paper/lb_com_2001_0370_en.pdf`>.

[8] SMITH, M. J. **Aircraft noise**. [S.l.]: Cambridge University Press, 2004.

[9] OATES, G. C. **Aerothermodynamics of aircraft engine components**. [S.l.]: AIAA, 1985. (AIAA Education Series).

[10] RICHTER, C. **Liner impedance modeling in the time domain with flow**. [S.l.]: Univerlagtuberlin, 2010.

[11] BIELAK, G. W.; PREMO, J. W.; HERSH, A. S. **Advanced turbofan duct liner concepts**. [S.l.]: National Aeronautics and Space Administration, Langley Research Center, 1999.

[12] JONES, M. G.; WATSON, W.; NARK, D. Impedance eduction in ducts with higher-order modes and flow. In: **Proceedings of the 15th AIAA/CEAS Aeroacoustics Conference**. [S.l.: s.n.], 2009.

[13] AURÉGAN, Y.; LEROUX, M.; PAGNEUX, V. Measurement of liner impedance with flow by an inverse method. In: **Proceedings of the 10th AIAA/CEAS Aeroacoustics Conference**. [S.l.: s.n.], 2004. v. 1, p. 464–470.

[14] JONES, M. G.; WATSON, W.; NARK, D. Effects of flow profile on educed acoustic liner impedance. In: **AIAA Conference**. [S.l.: s.n.], 2010. p. 2010–3763.

[15] JONES, M. G.; WATSON, W. R.; PARROTT, T. L. Benchmark data for evaluation of aeroacoustic propagation codes with grazing flow. **AIAA paper**, v. 2853, p. 2005, 2005.

[16] ROECK, W. D.; DESMET, W. Indirect acoustic impedance determination in flow ducts using a two-port formulation. In: **AIAA Conference**. [S.l.: s.n.], 2009. v. 3302, p. 2009.

[17] PARROTT, T. L.; WATSON, W. R.; JONES, M. G. **Experimental validation of a two-dimensional shear-flow model for determining acoustic impedance**. [S.l.], 1987.

[18] ALLARD, J.; ATALLA, N. **Propagation of sound in porous media: modelling sound absorbing materials 2e**. [S.l.]: John Wiley & Sons, 2009.

[19] INGARD, U. Influence of fluid motion past a plane boundary on sound reflection, absorption, and transmission. **The Journal of the Acoustical Society of America**, Acoustical Society of America, v. 31, n. 7, p. 1035–1036, 1959.

[20] WHITE, F. M. **Fluid mechanics**. 6. ed. [S.l.]: McGraw-Hill, 2007.

[21] CRANDALL, I. B. **Theory of vibrating systems and sound**. [S.l.]: D. Van Nostrand Company Princeton, 1926.

[22] GUESS, A. Calculation of perforated plate liner parameters from specified acoustic resistance and reactance. **Journal of sound and vibration**, Elsevier, v. 40, n. 1, p. 119–137, 1975.

[23] RICE, E. J. A model for the acoustic impedance of a perforated plate liner with multiple frequency excitation. In: **Acoustical Society of America, Fall Meeting**. [S.l.: s.n.], 1971.

[24] HECKL, M.; MULLER, H. **Taschenbuch der Technischen Akustik**. [S.l.]: Springer-Verlag, 1975.

[25] RIENSTRA, S. W. Impedance models in time domain, including the extended helmholtz resonator model. In: **12th AIAA/CEAS Aeroacoustics Conference**. Cambridge, USA: [s.n.], 2006. (AIAA 2006-2686).

[26] MUNJAL, M. L. **Acoustics of ducts and mufflers with application to exhaust and ventilation system design**. [S.l.]: Wiley New York (NY) et al., 1987.

[27] ELNADY, T.; BODÉN, H.; ELHADIDI, B. Validation of an inverse semi-analytical technique to educe liner impedance. **AIAA journal**, v. 47, n. 12, p. 2836–2844, 2009.

[28] MYERS, M. On the acoustic boundary condition in the presence of flow. **Journal of Sound and Vibration**, Elsevier, v. 71, n. 3, p. 429–434, 1980.

[29] AURÉGAN, Y.; LEROUX, M.; PAGNEUX, V. Abnormal behavior of an acoustical liner with flow. In: **Forum Acusticum**. [S.l.: s.n.], 2005.

[30] AURÉGAN, Y.; LEROUX, M. Experimental evidence of an instability over an impedance wall in a duct with flow. **Journal of Sound and Vibration**, Elsevier, v. 317, n. 3, p. 432–439, 2008.

[31] RIENSTRA, S. W. Acoustic scattering at a hard–soft lining transition in a flow duct. **Journal of Engineering Mathematics**, Springer, v. 59, n. 4, p. 451–475, 2007.

[32] ÅBOM, M. Measurement of the scattering-matrix of acoustical two-ports. **Mechanical Systems and Signal Processing**, Elsevier, v. 5, n. 2, p. 89–104, 1991.

[33] MATLAB Optimization Toolbox User's Guide. The MathWorks, Inc., Natick, Massachusetts, USA: [s.n.], 2013.

[34] LEVENBERG, K. A method for the solution of certain problems in least squares. **Quarterly of applied mathematics**, v. 2, p. 164–168, 1944.

[35] HILDEBRAND, F. B. **Introduction to numerical analysis**. [S.l.]: Courier Corporation, 1987.

[36] HAMMING, R. **Numerical methods for scientists and engineers**. [S.l.]: Courier Corporation, 2012.

[37] SHIN, K.; HAMMOND, J. **Fundamentals of signal processing for sound and vibration engineers**. [S.l.]: John Wiley & Sons, 2008.

[38] INTERNATIONAL ORGANIZATION FOR STANDARDIZATION. **Acoustics: Determination of sound absorption coefficient and impedance in impedance tubes. Part 1: Method Using Standing Wave Ratio**.

[39] INTERNATIONAL ORGANIZATION FOR STANDARDIZATION. **Acoustics: Determination of sound absorption coefficient and impedance in impedance tubes. Part 2: Transfer Function Method**.

[40] DEAN, P. D. An in-situ method of wall acoustic impedance measurement in flow ducts. **Journal of Sound and Vibration**, Elsevier, v. 34, n. 1, p. 97–130, 1974.

[41] WATSON, W. R.; GERHOLD, M. J. E. C. Implementation and validation of an impedance eduction technique. In: **Proceedings of the 17th AIAA/CEAS Aeroacoustics Conference**. [S.l.: s.n.], 2011. v. 2867.

[42] PETYT, M. **Introduction to finite element vibration analysis**. [S.l.]: Cambridge university press, 1990.

[43] ACTRAN 13. Free Fields Technology, Belgium: [s.n.], 2013.

[44] MATLAB Parallel Computing Toolbox User's Guide. The MathWorks, Inc., Natick, Massachusetts, USA: [s.n.], 2015.

[45] SERRANO, P. G. **Desenvolvimento de uma bancada de determinação da impedância acústica na presença de escoamento tangencial**. Dissertação (Mestrado) — Federal University of Santa Catarina, 2014.

[46] LABVIEW 2014. National Instruments Corporation, Austin, USA.: [s.n.], 2013.

[47] MASSON, Z. N. et al. Desenvolvimento de sistema de controle, aquisição e processamento de sinais para bancada de medição da impedância acústica de liners com escoamento. In: **Anais do VIII Congresso Nacional de Engenharia Mecânica**. [S.l.: s.n.], 2014.

[48] MATLAB Global Optimization Toolbox User's Guide. The MathWorks, Inc., Natick, Massachusetts, USA: [s.n.], 2013.

[49] FUJIMORI, T.; SATO, S.; MIURA, H. An automated measurement system of complex sound pressure reflection coefficients. In: INSTITUTE OF NOISE CONTROL ENGINEERING. **INTER-NOISE and NOISE-CON Congress and Conference Proceedings**. [S.l.], 1984. v. 1984, n. 1, p. 1009–1014.

[50] HOLMBERG, A.; ÅBOM, M.; BODÉN, H. Accurate experimental two-port analysis of flow generated sound. **Journal of Sound and Vibration**, Elsevier, v. 330, n. 26, p. 6336–6354, 2011.

[51] DOKUMACI, E. A note on transmission of sound in a wide pipe with mean flow and viscothermal attenuation. **Journal of Sound and Vibration**, Elsevier, v. 208, n. 4, p. 653–655, 1997.

[52] MEDEIROS, A. A. et al. Implementação e validação de método inverso para obtenção de impedância acústica de liners. In: **Anais do VIII Congresso Nacional de Engenharia Mecânica**. [S.l.: s.n.], 2014.

[53] PENROSE, R. A generalized inverse for matrices. In: CAMBRIDGE UNIVERSITY PRESS. **Proc. Cambridge Philos. Soc**. [S.l.], 1955. v. 51, n. 3, p. 406–413.

[54] CHEUNG, W.-S. et al. Acoustic flowmeter for the measurement of the mean flow velocity in pipes. **The Journal of the Acoustical Society of America**, Acoustical Society of America, v. 110, n. 5, p. 2308–2314, 2001.

APPENDIX A – Overdetermined Wave Decomposition

The usual method for finding the amplitudes of two opposite-traveling waves at a given position in a duct is the well-known Two-Microphone Method [39]. It is a standardized procedure consisting in measuring the acoustic field in two positions (hence the name) in a duct and extracting cross-spectrum functions between them to calculate the waves' amplitudes. In its original form, however, it has a few drawbacks, summarized as follows:

1. It does not include the convection effect by the flow,

2. It is sensitive to coherent measurement errors between the microphones due to the simply determined nature of the system of equations to be solved, and

3. It is not trivially expanded to support more then two microphones.

This appendix describes a multiple-microphone wave decomposition method that can be seen as a generalization of the Two-Microphone Method. It takes into account as many microphones as the user wants, to build a overdetermined system of N equations (N being the number of microphones) and 2 variables (the amplitudes of the opposite-traveling waves) that can be easily expanded to include the effect of low and to support more or less microphones. The minimum number of microphones is obviously two, in which case it matches the TMM results. The inclusion of more microphones has the advantage of helping suppress random errors like aerodynamic fluctuations in the test data [49, 50]. It is derived as follows.

Assuming that all higher order modes have decayed, only plane waves propagate in a hard-wall duct. Therefore the acoustic field, given by equation 2.35, can then be rewritten to include only propagating waves in the form

$$p(z) = p_i(z) + p_r(z) = a_i^{(1)} e^{-jk_{zi}^{(1)} z} + a_r^{(1)} e^{jk_{zr}^{(1)} z}. \tag{A.1}$$

In this case, the wave numbers in directions x and y are zero, and the dispersion relation, equation 2.36, can be solved for $k_z^{(1)}$, so that

$$k_z^{(1)} = \frac{k_0}{1 \pm M}, \tag{A.2}$$

where the plus sign is used for the incident wave ($k_{zi}^{(1)}$) and the minus, for the reflected wave ($k_{zr}^{(1)}$). When using data from experiments, Equation A.2 is modified to include the effects of visco-thermal damping using the model by Dokumaci [51].

The velocity in the z-direction in a given position z can be calculated [52] from:

$$u_z(z) = \left(\frac{a_i^{(1)}}{Z_0} e^{-jk_{zi}^{(1)} z} - \frac{a_r^{(1)}}{Z_0} e^{jk_{zr}^{(1)} z} \right), \tag{A.3}$$

or, by comparison with Equation A.1:

$$u_z(z) = \frac{1}{Z_0} p_i(z) - \frac{1}{Z_0} p_r(z). \tag{A.4}$$

From Equation A.1, it is possible to write the pressure at a position $z = z_1$ as a function of the pressure at another position $z = z_2$ as

$$\begin{aligned} p(z_1) =& p_i(z_1) + p_r(z_1) \\ =& p_i(z_2) e^{-jk_{zi}^{(1)}(z_1 - z_2)} + p_r(z_2) e^{jk_{zr}^{(1)}(z_1 - z_2)}. \end{aligned} \tag{A.5}$$

ç If the acoustic pressures in two positions z_1 and z_2 are known, one could use Equation A.5 to form a system of 2 equations and 2 unknowns, the pressure amplitudes at, for instance, z_1, $p_i(z_1)$ and $p_r(z_1)$. This system could also be extended to an overdetermined system of N measurements in different positions, resulting in:

$$\begin{Bmatrix} p_i(z_1) \\ p_r(z_1) \end{Bmatrix} = \begin{bmatrix} e^{-jk_{zi}^{(1)}(z_2 - z_1)} & e^{jk_{zr}^{(1)}(z_2 - z_1)} \\ e^{-jk_{zi}^{(1)}(z_3 - z_1)} & e^{jk_{zr}^{(1)}(z_3 - z_1)} \\ \vdots & \vdots \\ e^{-jk_{zi}^{(1)}(z_N - z_1)} & e^{jk_{zr}^{(1)}(z_N - z_1)} \end{bmatrix}^{\dagger} \begin{Bmatrix} p(z_2) \\ p(z_3) \\ \vdots \\ p(z_N) \end{Bmatrix}, \tag{A.6}$$

and the † represents the Moore-Penrose pseudo-inverse [53]. With Equation A.6, it is possible to calculate the incident and reflected waves at any axial position within a hard duct, given that the pressure is known on at least two positions from, for instance, microphone measurements. It is also worth mentioning that from p_i and p_r it is possible to calculate reflection coefficients.

APPENDIX B – Impedance Results of Liners 1, 2, and 3

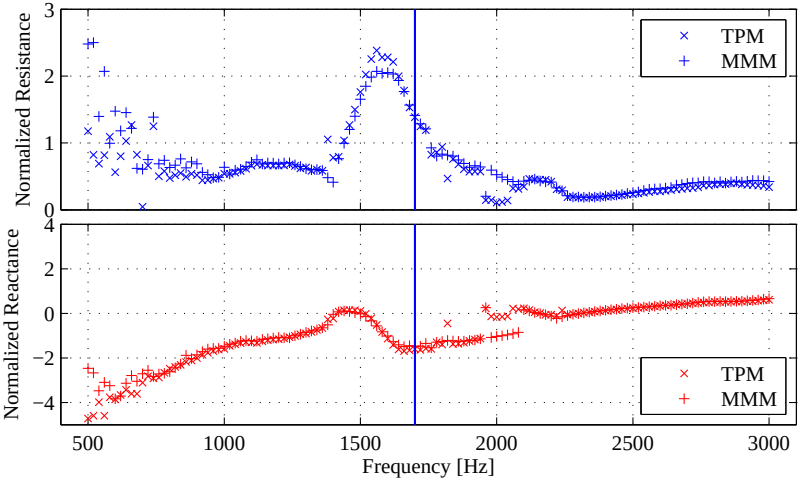

Figure B.1 – Liner 1 impedance results in no-flow condition.

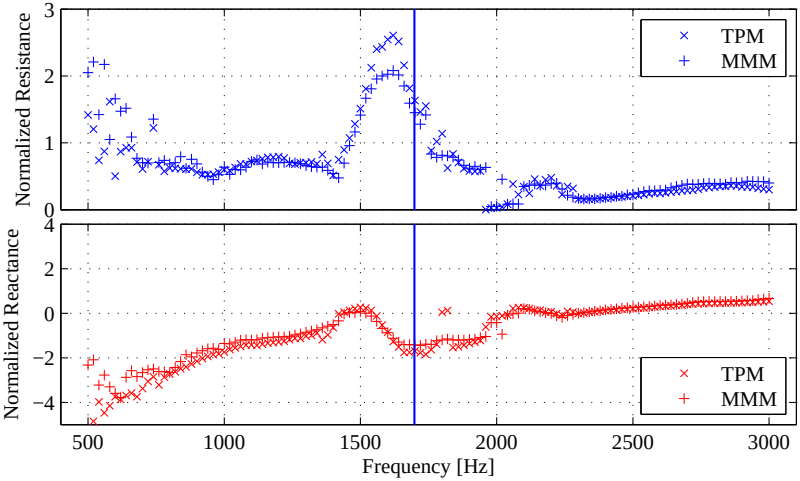

Figure B.2 – Liner 1 impedance results in Mach 0.05 condition.

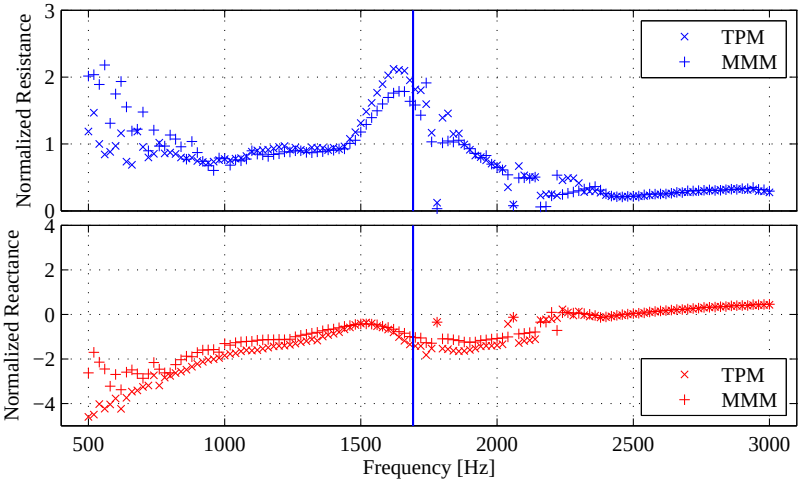

Figure B.3 – Liner 1 impedance results in Mach 0.10 condition.

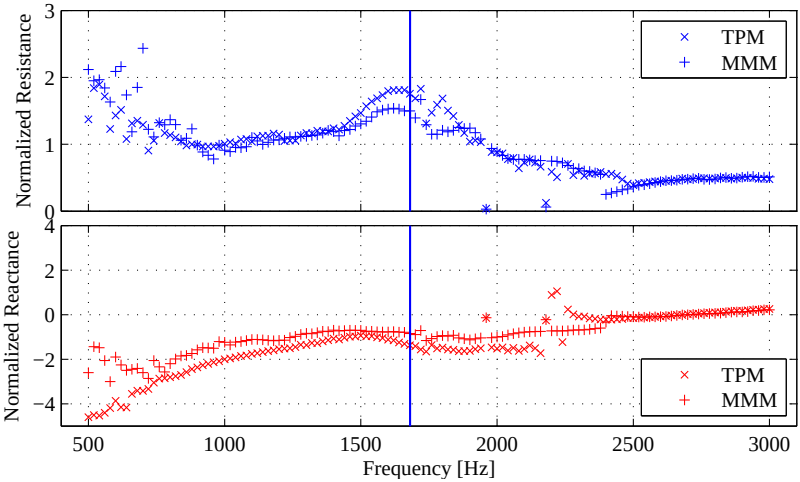

Figure B.4 – Liner 1 impedance results in Mach 0.15 condition.

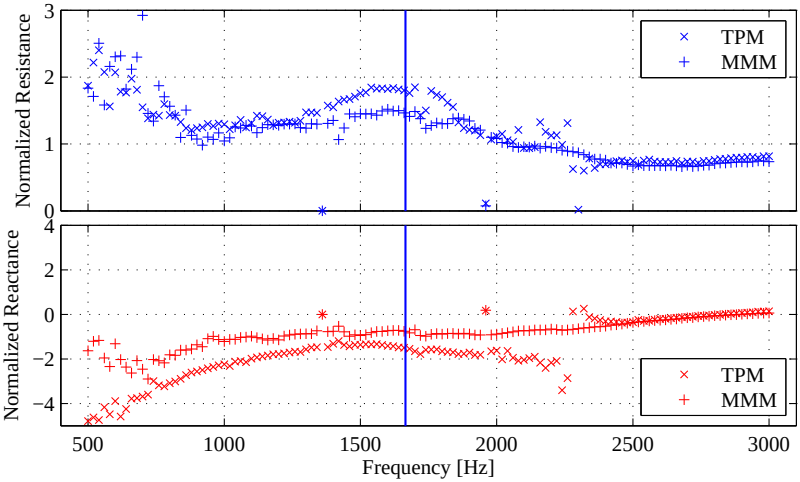

Figure B.5 – Liner 1 impedance results in Mach 0.20 condition.

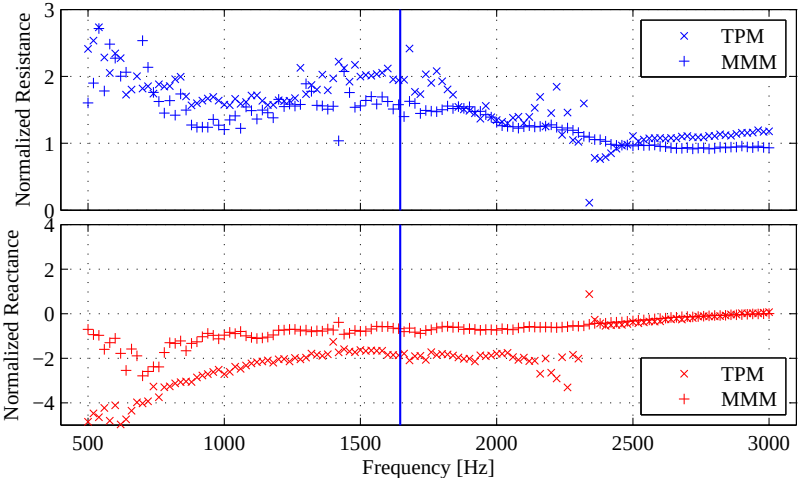

Figure B.6 – Liner 1 impedance results in Mach 0.25 condition.

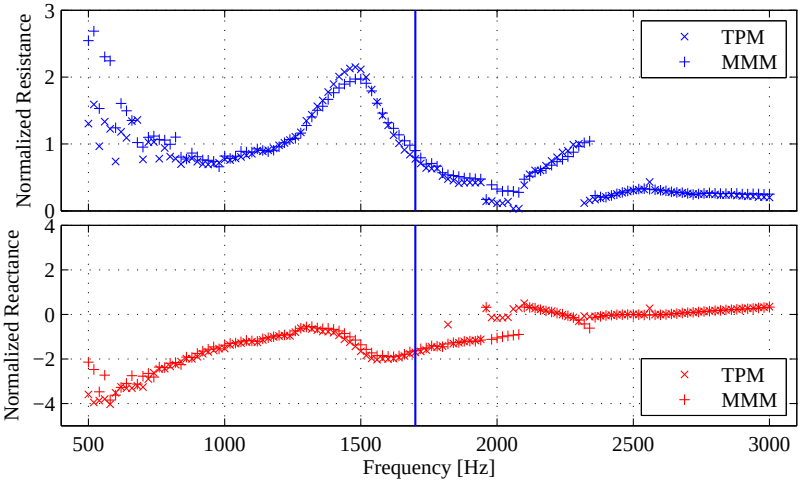

Figure B.7 – Liner 2 impedance results in no-flow condition.

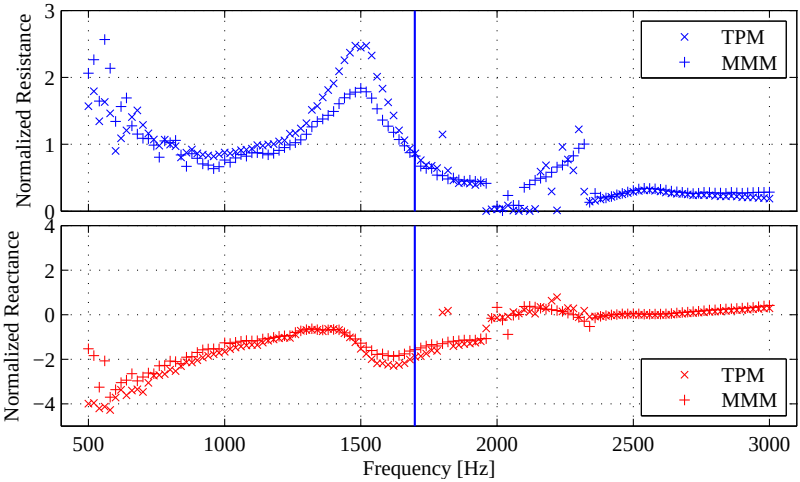

Figure B.8 – Liner 2 impedance results in Mach 0.05 condition.

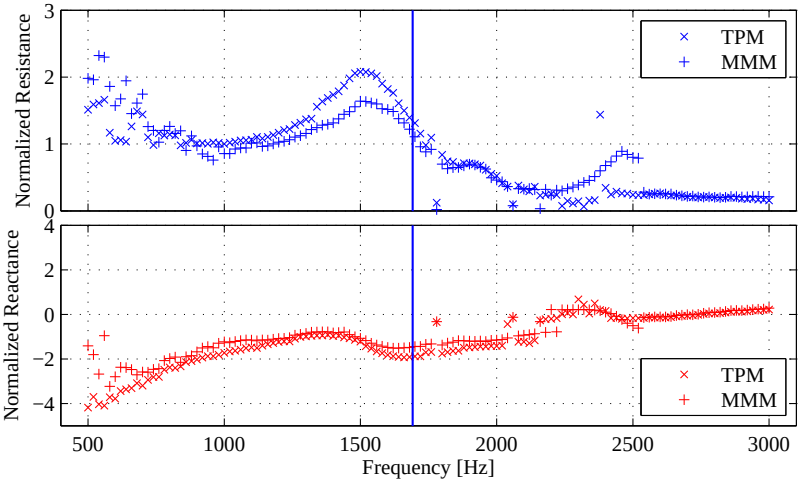

Figure B.9 – Liner 2 impedance results in Mach 0.10 condition.

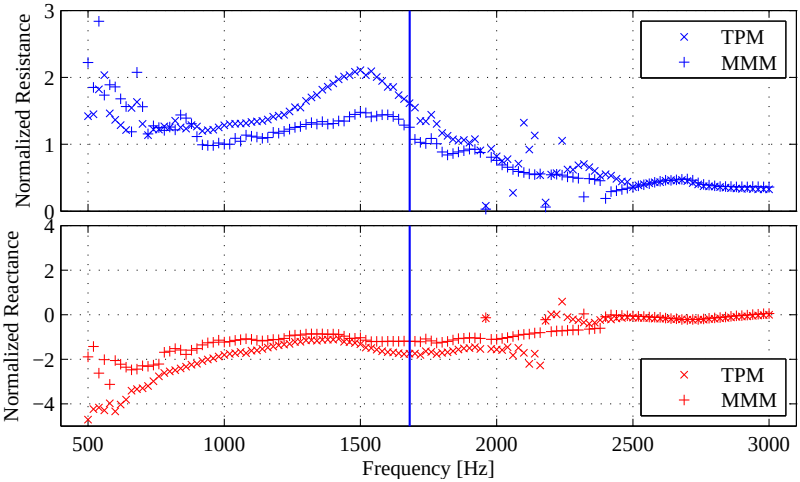

Figure B.10 – Liner 2 impedance results in Mach 0.15 condition.

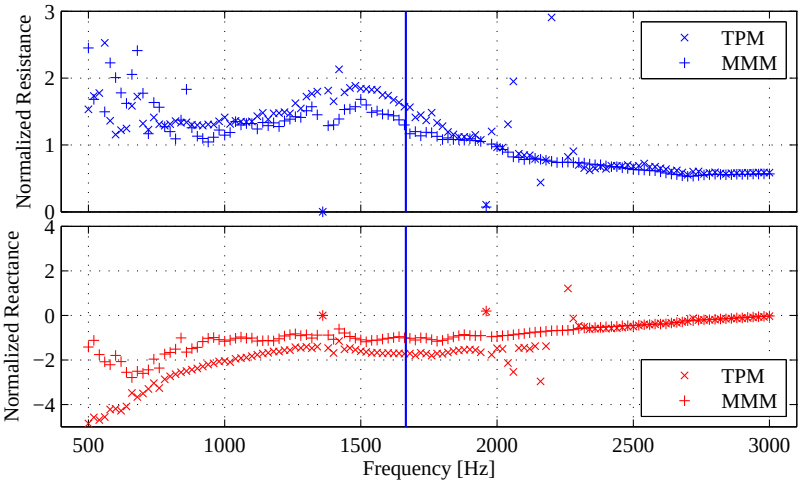

Figure B.11 – Liner 2 impedance results in Mach 0.20 condition.

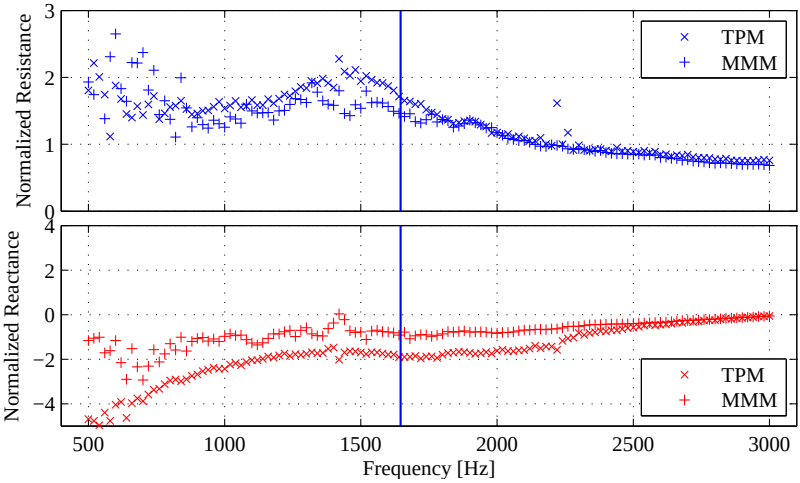

Figure B.12 – Liner 2 impedance results in Mach 0.25 condition.

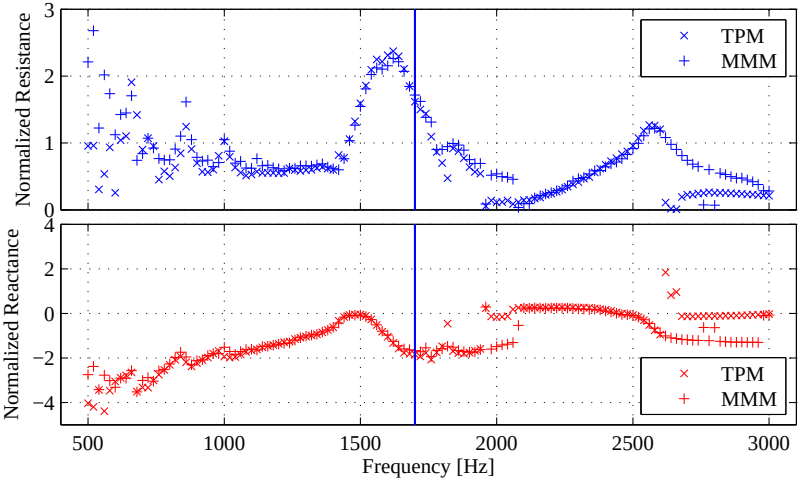

Figure B.13 – Liner 3 impedance results in no-flow condition.

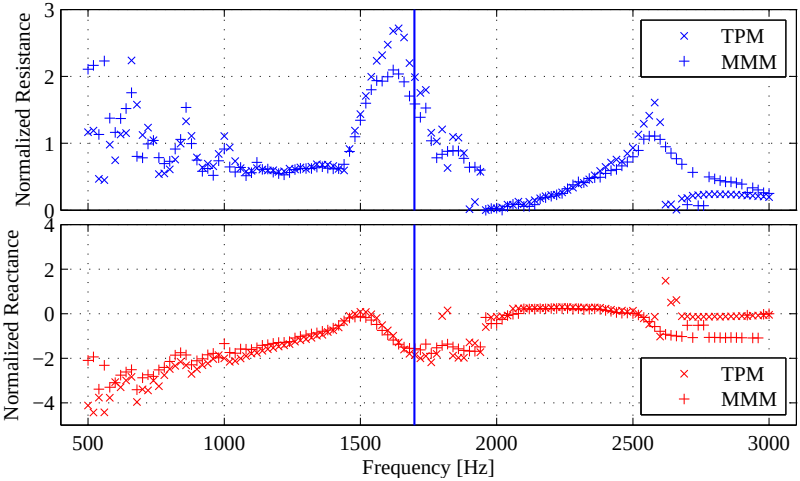

Figure B.14 – Liner 3 impedance results in Mach 0.05 condition.

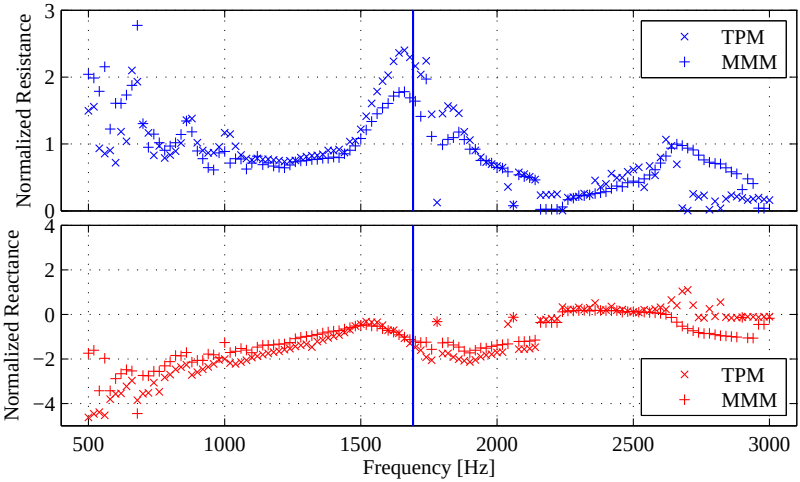

Figure B.15 – Liner 3 impedance results in Mach 0.10 condition.

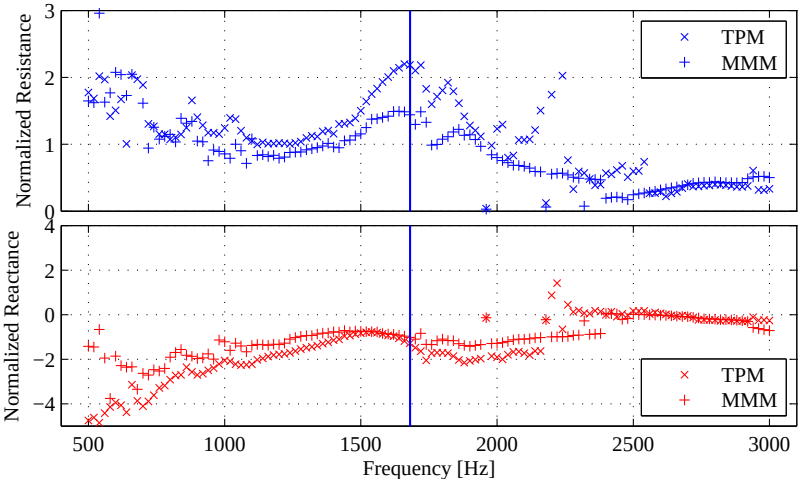

Figure B.16 – Liner 3 impedance results in Mach 0.15 condition.

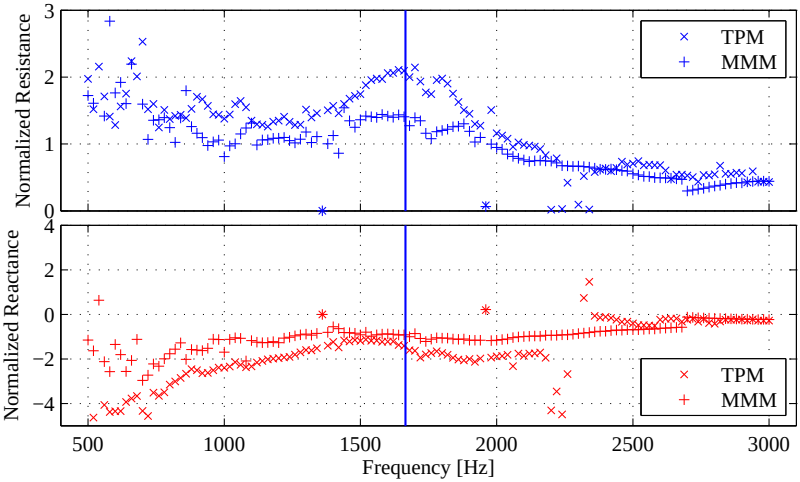

Figure B.17 – Liner 3 impedance results in Mach 0.20 condition.

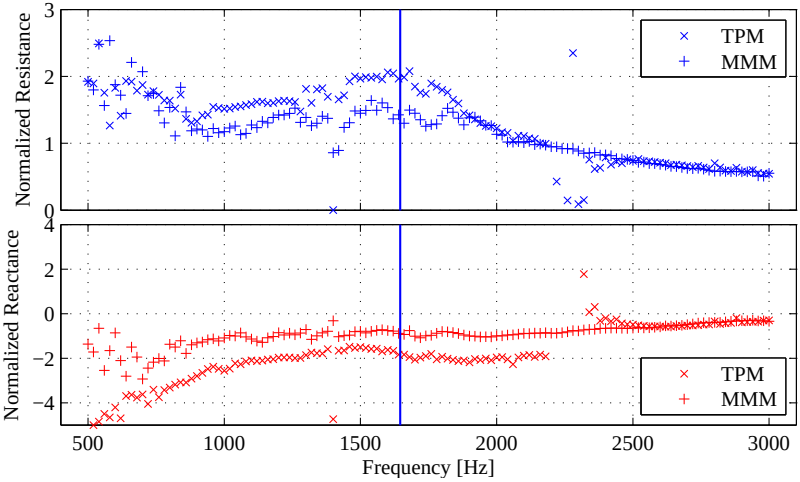

Figure B.18 – Liner 3 impedance results in Mach 0.25 condition.

APPENDIX C – Acoustic Flowmeter

In this appendix, a technique for determining the mean flow velocity in a plane-wave duct from acoustic measurements, used for all experimental results shown in this dissertation, will be described.

The idea of using acoustic measurements to determine the flow velocity is not new; Cheung et al. [54] proposed a technique that used the phase change between different positions in a duct to extract the flow velocity. They however used equally spaced microphones to measure the incident and the reflected wave, which allowed them to use a direct, least-squares solution to the problem. Holmberg et al. [50] also proposed a simple technique based on the wavenumber variation due to flow, very similar to the technique described here, but also assumed the same incident and reflected waves at the different microphones. In the current work, nevertheless, microphones were positioned in the sections before and after the test section, in which plane-waves of different amplitudes are propagating. To take advantage of the over-determination provided by the current system, a different approach was taken, as will be described next.

Figure C.1 – Schematic representation of the test duct with microphones before and after the liner sample.

If a system as depicted in Figure C.1, with k microphones before and k after the test section, is considered, the acoustic field at the n-th microphone before the test section can be calculated from:

$$p_n = \left(a_{1i}e^{-jk_{zi}z_n} + a_{1r}e^{jk_{zr}z_n}\right)e^{j\omega t}, \tag{C.1}$$

and after the test section, from:

$$p_n = \left(a_{2i}e^{-jk_{zi}z_n} + a_{2r}e^{jk_{zr}z_n}\right)e^{j\omega t}, \tag{C.2}$$

where $z_n = z_1, z_2, ..., z_{2k}$ are the positions of the microphones along the duct. As seen in Appendix A, the wavenumber k_z is given by

Equation A.2, i.e.,:

$$k_z^{(1)} = \frac{k_0}{1 \pm M}. \qquad \text{(A.2 revisited)}$$

Now, for a given guess of the Mach number M and the incident and reflect wave amplitudes at each duct section, a_{1i}, a_{1r}, a_{2i}, and a_{2r}, the acoustic field at the n-th microphone position can be calculated using Equations C.1 and C.2, and compared to the measured one, $p_{n,meas}$, giving the error function, e:

$$e_n = p_n - p_{n,meas}, \qquad \text{(C.3)}$$

which is minimized by finding the correct values of the Mach number and plane-wave amplitudes. By doing this together for all microphone positions, a system of $2k$ equations (Equation C.3, once for each microphone) and 5 unknowns is assembled, which can be solved using a standard non-linear solver, for instance, the *fsolve* minimizer with the Levenberg-Marquardt [34] algorithm in MATLAB.

With the addition of more microphones, the number of unknowns is unaltered, but the number of equations increases, which might help suppress random errors in the measurement data. Here, for illustrative purposes, an equal number of microphones was chosen at each side of the test section; this however is not required. Any number of microphones larger then 3 might be used at each group of microphones sharing the same plane-wave amplitudes.

In tests carried-out for this work, the results of the proposed method were compared to Pitot tube measurements, from Mach 0 to Mach 0.25. Differences below 2% were seen at all flow speeds, which were smaller then the standard deviation of the Pitot measurements.